

https://dspace.org/

Synthesis and characterization of mixed metal tungstate and titanates

Makhura, Ngwakwana Bridget

2011-06-23
http://hdl.handle.net/10539/10177

Downloaded from a DSpace repository. https://dspace.org/

Abstract

This dissertation investigates the synthesis of different mixed metal oxides using modern and classical synthetic techniques and their characterization by powder x-ray diffraction (PXRD) techniques and structure refinement using Rietveld. The *ex situ* and *in situ* variable temperature PXRD studies were performed to determine the structure of all the materials, thermal behaviour and quantitative Rietveld phase analysis of the synthesized oxides. Lead tungstate, niobium tungstate mixture, nickel titanate and nickel tungstate are the materials used in the study. The main characteristic studied was the thermal behaviour using the in situ thermal studies to determine the co efficient of thermal expansion.

Synthesis and Characterization of Mixed Metal Tungstate and Titanates

Ngwakwana Bridget Makhura

University of the Witwatersrand

Supervisor: Prof. DG Billing

A Dissertation submitted in partial fulfilment of the requirements

For the degree of Master of Science

Department of Chemistry

University of the Witwatersrand

2009

Table of contents

ABSTRACT **1**

TABLE OF CONTENTS **4**

DECLARATION **8**

ACKNOWLEDGEMENTS **9**

CHAPTER 1 INTRODUCTION **10**

1.1 SUMMARY **12**

1.2 REFERENCES: **14**

CHAPTER 2 BACKGROUND **15**

2.1 PREPARATION METHODS **15**

2.2 THERMAL EXPANSION **23**

2.2.1 What is thermal expansion? *24*

2.2.2 The co-efficient of volumetric expansion *27*

2.2.3 The co-efficient of linear thermal expansion *28*

2.2.3.1 Thermal expansion of ice 31

2.2.3.2 Mechanisms of negative thermal expansion 33

2.3 EXPERIMENTAL MEASUREMENT TECHNIQUES **35**

2.4 CHARACTERIZATION X-RAY DIFFRACTION **39**

2.4.1 Powder X-ray diffraction *40*

2.4.2 Rietveld Refinement *46*

2.4.2.1 Extraction method 53

2.4.2.2 The refinement strategy 55

2.4.2.3 Rietveld software 58

2.5 REFERENCES: 61

CHAPTER 3 INSTRUMENTATION AND DATA ANALYSIS 68

3.1 DATA COLLECTION 68

3.2 RIETVELD REFINEMENT INSTRUMENT CALIBRATION 70

3.3 CALIBRATION OF THE VARIABLE TEMPERATURE STAGE 73

3.4 REFERENCES: 86

CHAPTER 4 : SYNTHESIS, STRUCTURAL CHARACTERIZATION AND THERMAL EXPANSION BEHAVIOR OF LEAD TUNGSTATE 88

4.1 INTRODUCTION 88

4.2 SYNTHESIS 91

4.3 PHASE IDENTIFICATION OF LEAD TUNGSTATE 94

4.4 STRUCTURAL REFINEMENT FROM RIETVELD REFINEMENT 97

4.5 DETERMINING THE THERMAL EXPANSION COEFFICIENT OF LEAD TUNGSTATE USING VARIABLE TEMPERATURE XRD AND RIETVELD REFINEMENT 110

4.6 CONCLUSION 116

4.7 REFERENCES: 117

CHAPTER 5 : QUANTITATIVE RIETVELD PHASE ANALYSIS: NIOBIUM TUNGSTATE 119

5.1 INTRODUCTION 119

5.2 SYNTHESIS 120

5.3 PHASE ANALYSIS 121

5.4 QUANTITATIVE RIETVELD PHASE ANALYSIS 123

5.5 EFFECT OF ANNEALING IN AIR ON THE NIOBIUM TUNGSTATE MIXTURE STUDIED BY IN-SITU POWDER XRD 127

5.6 CONCLUSION 131

5.7 REFERENCES: 132

CHAPTER 6 : SYNTHESIS, CHARACTERIZATION AND SOLID STATE REACTION USING VARIABLE TEMPERATURE *IN-SITU* XRD OF NICKEL BASED OXIDES 134

6.1 INTRODUCTION 134

6.2 SYNTHESIS 135

6.3 PHASE IDENTIFICATION 139

6.4 SOLID STATE REACTION OF NICKEL TITANATE USING VARIABLE TEMPERATURE IN-SITU XRD AND RIETVELD REFINEMENT 143

6.5 VARIABLE TEMPERATURE STUDY OF NICKEL TUNGSTATE FROM POWDER XRD AND RIETVELD REFINEMENT 150

6.6 CONCLUSION 158

6.7 REFERENCES: 159

CHAPTER 7 GENERAL CONCLUSION 161

CHAPTER 8 LIST OF FIGURES 163

CHAPTER 9 LIST OF TABLES.....165

Declaration

The work described in this thesis is entirely the work my own, except where I have acknowledged help from a named person *or* given a reference to a published source or a thesis.

The research presented was performed in the Department of Chemistry, University of the Witwatersrand between January 2006 and June 2009, the results of which have not been submitted for a degree in this or any other university.

This thesis conforms to the word limit set out in the Degree Regulations. It contains 21 847 words including appendices, footnotes and references but excluding experimental data included on the CD-R located at the rear of the thesis.

Date: Signature:

Acknowledgements

“In the memory of my farther”

Chapter 1 **INTRODUCTION**

Modification of natural substances like rocks and minerals by simple procedures such as heating and pressure treatments has produced new classes of materials, e.g. ceramics, glasses and cements. These new materials are made to mimic the natural minerals and rocks by structure and composition and enhance their important properties of pre-historic value. In this dissertation the synthesis of selected ceramic materials, their PXRD characterization and their thermal behaviors are investigated

Ceramic is a term covering a range of inorganic non-metallic materials whose formation is due to heat. They are classified into three categories: the oxides, (e.g. alumina, silica and ziconia), the non-oxides (e.g. carbides, borides, nitrides and silicates) and thirdly the composite materials which are combinations of both the oxides and non-oxides, with each class having different properties [1]. The oxide ceramics are generally resistant to oxidation and are chemically inert and show high electrical insulation and low thermal conductivity. The non-oxides have a low resistance to oxidation and tend to be extremely hard. They are also chemically inert but have high thermal and electrical conductivity. The ceramics based on composite components are generally tough with variable oxidation resistance depending on the type and variable thermal and electrical properties [1].

Selecting or modifying a particular composition, the firing process or heating treatment to obtain useful products requires an understanding of material properties and structure. Ceramics have numerous forms uses such as in kiln linings, gas fire radiant's, steel, glass making crucibles, gas burner nozzles, ballistic protection, nuclear fuel uranium oxide pellets, bio-medical implants, jet engine turbine blades, and missile nose cones and etc. and behave in equally diverse ways. Their uniformed properties include thermal behaviour (such as found in ZW_2O_8 a negative coefficient of thermal expansion), optical, electrical (e.g. superconductors: Yttrium barium copper oxide), magnetic e.g. the ferro-, parra-, antiferro and ferromagnetic materials such as Fe_3O_4 which is ferromagnetic and biological properties as found in bio-medical implants [2].

The powder diffraction technique is one of the best methods for characterizing and understanding the structure of most ceramics [3]. Single crystal forms of most ceramics are difficult to grow and therefore the powder form tends to be used for characterisation. The main advantage of the powder diffraction technique over other analysis methods such as X-ray fluorescence, wet chemical methods, thermo gravitational and etc., is that it is fast and non-destructive. More recently the use of *in-situ* powder X-ray diffraction (PXRD) has opened doors for exploitation of the technique and increased the amount of information that can be obtained. For example, if the PXRD for a solid state reaction is measured over a certain time

period, the reaction kinetics can be studied over a temperature and pressure range and hence the thermal and pressure behaviours of materials can be studied [4-6].

1.1 *Summary*

The present study describes the synthesis of different mixed metal oxides using different well known methods such as sol-gel, citrate and classical solid state synthetic techniques, the characterization of the synthesized oxides using powder X-ray diffraction (PXRD) techniques and structure refinement using Rietveld refinement [7-0]. The *ex-situ* PXRD study of the structure and phase composition of the "as synthesized" oxides will be presented as well as in situ variable temperature PXRD studies for thermal expansion measurement, variable temperature phase quantification and general thermal behaviour of the synthesized oxides. Chapter 2 presents the background and literature study, for the synthesis, PXRD and Rietveld refinement techniques methods used. In chapter 3, the data collection methods are presented, including the calibration of the instruments

Chapter 4 explores the synthesis of Lead Tungstate, with the scheelite (AMO_4), by using sol-gel method. The use of PXRD technique to identify and characterize the resulting materials, and Rietveld powder diffraction pattern refinements will be

presented. It also contain the in situ high temperature PXRD measurement of the resulting coefficient of thermal expansion

In chapter 5 a mixed niobium tungstate material is reformed using the classical solid state synthetic techniques. The quantitative Rietveld phase analysis of the mixture a room temperature will be presented and an in situ PXRD study of how the phases change with temperature.

The synthesis of Nickel based oxides are reformed in chapter 6.The sol-gel method is used for the synthesis of nickel titanate and a citrate method is used for the synthesis of nickel tungstate. PXRD studies of the resulting oxides are presented. Quantitative phase analysis for the resulting nickel tungstate mixture, rutile, $NiTiO_3$ (red) and $Ni_{2.44}Ti_{0.77}O_4$ are performed using in situ high temperature PXRD. The coefficient of thermal expansion and the thermal behaviour of nickel tungstate are presented.

Chapter 7 gives a short analysis of the overall work presented in the dissertation and multi-future work arising from this body of work.

1.2 ***References:***

1. D.W. Richerson, B.J Dumbar, *The magic of ceramics*, Westerville: Ohio, American Ceramic Society, 2000

2. T. A. Ring, *Fundamentals of Ceramic Powder Processing and Synthesis,* Academic Press, 1996

3. C. B. Carter, M. G. Norton, *Characterizing Structure, Defects, and Chemistry*, Springerlink, 2007, **ch 10**, 154

4. J.S. Evans, I.R. Evans, Beyond classical applications of powder diffraction, Chem. Soc. Rev., 2004, **33**, 539-547

5. V. K. Pecharsky and P. Y. Zavalij, *Fundamentals of Powder Diffraction and Structural Characterization of Materials*, Kluwer Academic Publishers, Boston, 2003.

6. N.E. Wilfred, *X-ray diffraction methods*, Wiley, 1966

7. R. A. Young (ed.), *The Rietveld Method*, Oxford University Press, Oxford, UK, 1993

H. M. Rietveld, A profile refinement method for nuclear and magnetic structures,

Chapter 2 BACKGROUND

2.1 Preparation methods

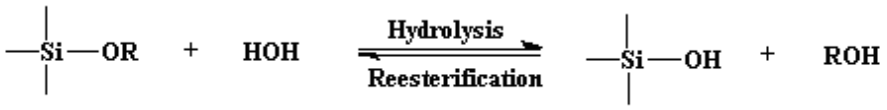
This section deals with the chemical synthesis of ceramic materials. The methods used include sol-gel processes, powder mixing, citrate-gel method, co precipitation, combination methods, fusion, hydrothermal techniques and emulsion methods.

Chemistry is a big contributor to modern day material processing and synthesis since it opens up the potential to produce products with tailored properties. An increased number of synthesis routes to novel materials and naturally occurring materials, usually powders, now follow chemical protocols. This was highlighted by the discovery of high temperature superconductors such as $YBa_2Cu_2O_{7-x}$ in 1986 [1]. Successful synthesis of these powders still require additional fabrication protocols to move them into useful formats for wider a variety of applications, e.g. coatings, fibres, monolithic ceramics and powders with controlled particle and pore sizes. This chapter will summarize some of the synthetic methods used for making ceramics and the use of diffraction techniques to characterize and analyze them.

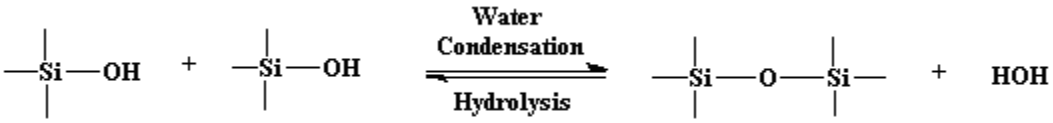
2.1.1 Sol-gel processing

Around 1970, Disiich prepared a silica glass lens by the sol-gel method and since then sol-gel science and technology has continued to contribute to a wide and increasing variety of materials research.

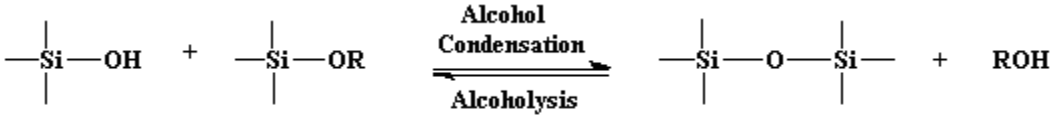
The silica alcogels where synthesized from the hydrolysis of $Si(OC_2H_5)_4$ solution in the presence of ethanol and calcined at 243^{o}C and 6.4 MPa pressure [1]. The reaction is outlined in equations 2.1 – 2.3.



1-1



1-2



1-3

It is a multipurpose solution process for making different kinds of ceramic and glass materials. To generalize, the sol-gel preparation method involves the transition of a system from a liquid "sol" (mostly colloidal), which is a dispersion of solid particles in a liquid phase where the particles are usually small enough (around 1 micron) to remain in suspension indefinitely by Brownies motion [2]. Then turned into a solid "gel" phase, which is a solid containing a liquid component and an internal 3-D network structure such that both the solid and the liquid are in a highly dispersed state [3], as shown schematically in Figure 1.1. This opens up possibilities to engineer ceramic or glass materials in a wide variety of forms: ultra-fine or spherical shaped powders, thin film coatings, ceramic fibers, microporous inorganic membranes, monolithic ceramics and glasses, or extremely porous aerogel materials [4-5].

The whole process can be described in the following way: the components are ultra-homogeneously mixed on an atomic scale into a solution and a gellation is made and controlled by pH, ionic strength, temperature and time with these parameters contributing differently in each synthesis. The gel is then shaped to the desired form, dried and calcined to the final product at lower temperature.

The starting materials used in the preparation of the "sol" are usually inorganic metal salts or metal organic compounds such as transition metal alkoxides, $M(OR)_n$.

Typically the transition metal alkoxide is subjected to a series of hydrolysis and polymeration reactions to form a colloidal suspension, or a "sol". Then the "sol" is processed, which could just be solvent evaporating or by addition of a gelling agent, typically water to give a wet "gel". The gel is dried and calcined, thus converting it into dense ceramic or glass articles [7 - 9]. Depending on the conditions, a highly porous and extremely low density material called an "aerogel" is obtained or the "sol" is adjusted into the right viscosity range. Ultra-fine and uniform ceramic powders are formed by precipitation, spray pyrolysis, or emulsion techniques. Formation of a metal oxide involves connecting the metal centers with oxo (M-O-M) or hydroxo (M-OH-M) bridges, therefore generating metal-oxo or metal-hydroxo polymers in solution [10-11]. Figure 1.1 shows some of the types of materials that can be made using the sol-gel process.

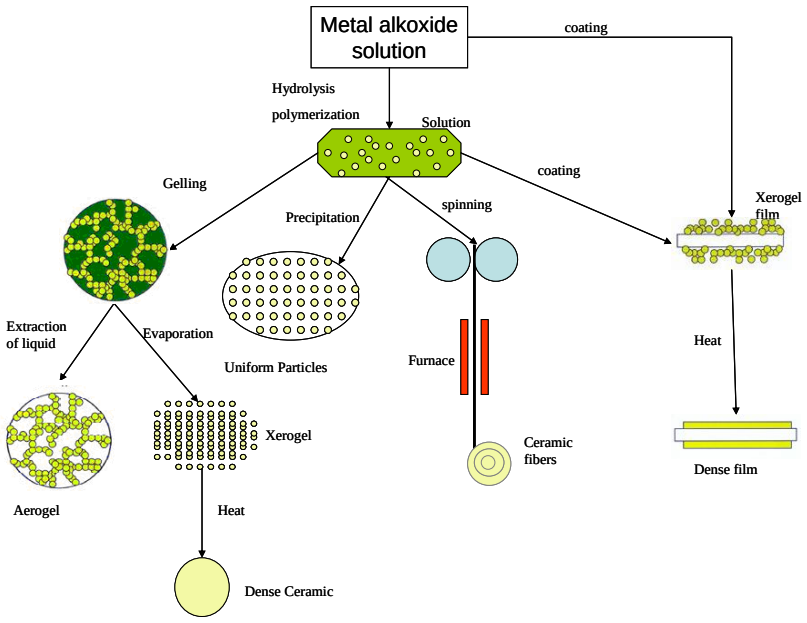


Figure 1.1: Schematic diagram of the general sol-gel processes

2. Powder mixing method

The powder mixing technique is the conventional method usually used to make multiphase oxides. It is a method where oxides, hydroxides or carbonates are mixed and the mixture then milled and heated repeatedly. This mixing and heating can be done in powder form or compacted pellet form to increase a solid-state reaction rate. For example, to make barium titanate using this method, barium oxide and titanium oxide are milled and calcined at 1200^{o}C repeatedly [6].

3. Citrate Gel method

The Citrate gel process uses an organic acid containing at least one hydroxyl and one carboxylic group e.g. tartaric, lactic as glycolic acid, as a chelating agent for synthesis. The acid is added to a number of metal salts, depending on the final product composition to create a solution. An alcohol is added to the mixture and heated for the polyesterification of the chelate. The pH of the resulting mixture is increased to 6-7.5 with a base, which results in formation of a highly viscous mixture, which is dried to give an amorphous gel. The gel is calcined to give the ceramic [5]. Superconductors are made from this method e.g. $Yba_2Cu_3O_{7-x}$ [12] and $Ba_3CoCuFe_{24}O_{41}$ [13] as shown in the process diagram outline in Figure 1.2.

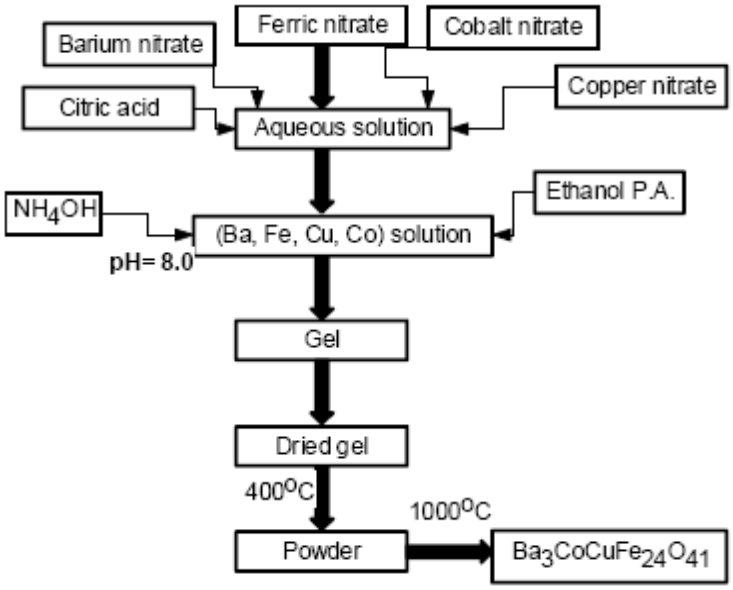


Figure 1.2: Process flow diagram for synthesis of $Ba_3CoCuFe_{24}O_{47}$ using the citrate gel method.

4. Co-precipitation

In the precipitation method an electrolyte solution is used to co-precipitate hydroxides or oxalates. The resulting precipitate is washed, dried, calcined and milled [14]. This method is based on the preparation of multi-component ceramic oxides through formation of intermediate precipitates. They can be in the form of hydrous and oxalate salts that are soluble in most mediums to ensure an intimate mixture of components. This will maintain homogeneity through to the calcinations step and hopefully to the final product.

$$BaCl_2 + TiOCl_2 + 2H_2C_2O_4 + 4H_2O \longrightarrow BaTiO(C_2O_4)_2.4H_2O + 4HCl \quad 1\text{-}4$$

For example, the method was applied to the preparation of barium titanate, with the equation outline given in equation 2.4. Barium titanyl oxalate precipitate can be formed when oxalic acid is added to a mixture containing chlorides of barium and titanium [15]. This method can also be easily used for doping materials. Another example where this method was used was for the synthesis of bayerite (β-$Al_2O_3.3H_2O$), where bauxite mineral is initially dissolved in NaOH electrolyte and then undergoes auto-precipitation to bayerite after neutralization with CO_2 gas [16]

5. Fusion method

A method where oxides are fused at high temperature and the resulting solidified melt is crushed to a powder is called fusion [1]. This method has disadvantages such as the loss of volatile components due to the higher temperatures of operation and the limited range of viscosity of most melt.

6. Hydrothermal Synthesis

This method involves heating metal salts, oxides or hydroxides in a solution or suspension form, in a liquid at an elevated temperature and pressure of up to 300^{o}C

and 1000 Bar [1]. It offers direct route to as oxide powder in a low temperature synthesis, to submicrometre without calcinations required in the sol-gel technique and a narrow size distribution.

The synthesis of $BaFe_{12}O_{19}$ from suspension of $Ba(OH)_2$ and α-FeOOH illustrates the improvements associated with in this method. A phase pave $BaFe_{12}O_{19}$ was formed at 325^{o}C as compared to the 1150^{o}C- 1250^{o}C required for the same product synthesized by conventional solid state reaction powder mixing methods [17].

7. Combination method

The combination method, also called the self-propagating high-temperature synthesis (SHS) method, involves an exothermic reaction above 2500^{o}C with no dependence on stability of reaction, which means no furnace is required. The reactions occurring could be of different type, e.g. redox, thermite, (which produces multiphase compositions like cements) or reactions that need chemical activators. The end product from this technique is usually a porous powder [18].

8. Homogeneous nucleation

The homogeneous nucleation method is a variation of the sol-gel technique, where micro-spheres such as urania and thoria are used as feed materials for fuel-pellet

fabrication used in nuclear reactors and droplets gelling occur when there is a homogeneous release of ammonia when hexamethylenetetramine decomposes into metal-oxide spheres [7].

2.2 Thermal Expansion

There exists a general tendency for ceramics, metals and alloys to undergo dimensional changes when responding to temperature variations. This tendency or property brings about critical implications for industries that process materials at elevated temperatures. These properties are of great importance to all ceramics but critical to the ones with applications like thermal insulation, superconducting etc.

Capacity, C_p, which is the measure of energy required to raise the temperature of a material, the coefficient of thermal expansion, α, which is the change in volume or linear dimension per degree of change in temperature and the heat conductivity, which is the amount of heat conducted through a body per temperature increase. C_p and thermal expansion govern thermal stress, the operating temperature and temperature gradients since they determine the rate of temperature change in a ceramic during heating in fabrication and in application [19].

In many metallurgical operations such as casting or spraying-forming, forging, rolling or extrusion the influences of thermal stress or strain from temperature variations can lead to cracks or defects. Optimization of such process calls for the thorough understanding of thermal characteristics of the material. Thermal expansion is also closely related to the thermal shock resistance of materials. Materials with a high CTE show poor thermal shock resistance, as rapid heating or cooling can result in temperature gradients that will cause cracks.

2.2.1 What is thermal expansion?

Thermal expansion of solids is an inter-atomic potential dependant physical property. When two atoms are brought closer together the overall potential energy of the whole system is determined by an attractive force until the distance between the atoms becomes very short and the bonding electrons cannot overcome the short term repulsion forces. This increases the potential energy. The interatomic potential function, of a simple harmonic oscillator is shown in figure 2.3. For an attractive interaction the potential energy decreases as the distance decreases and the atoms are brought closer together, until bond formation begins. This is indicated by the right side of the curve. Repulsive interactions increase the potential energy with further decrease in atomic distance starting at a minimum. If temperature is

increased to T_2 there would be no change in the average bond distance (R), i.e. no thermal expansion [20] as shown in figure 2-3

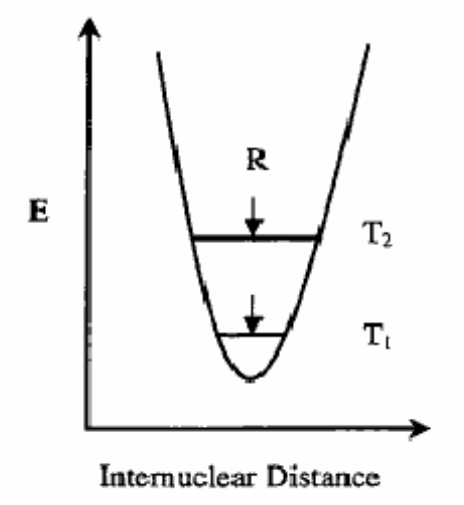


Figure 1.3 Potential energy diagram of a harmonic oscillator

Realistically atoms vibrate in an anharmonic way caused by an asymmetric potential energy well. The variation of the potential function with interatomic separation for an anharmonic oscillator is represented in **Figure 1.4**. At temperature T_1, the intersection of the horizontal line with the curve marks the extreme values of the internuclear distance where oscillation energy is all potential energy, and the midpoint marks the average value. As the temperature increases to T_2, the average bond length shifts to larger distances due to the asymmetry of the potential well. The increase in the average bond length contributes to the thermal expansion of the back material. The size of the asymmetry is dependent on the bond strength for the

thermally sampled region. A stronger bond has a more symmetric potential well, meaning a smaller bond expansion [29]

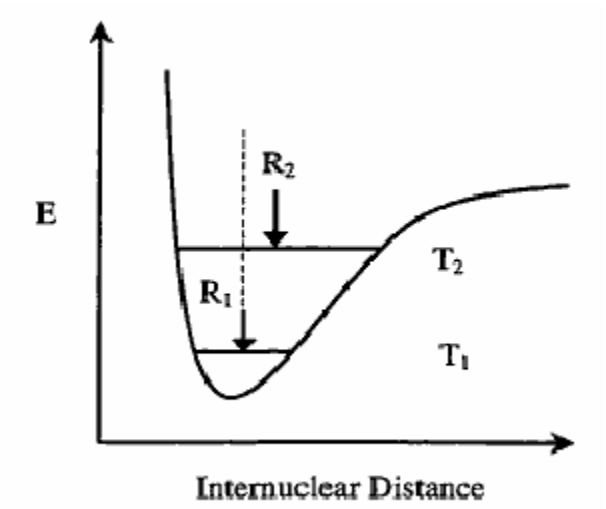


Figure 1.4 Potential energy diagram for an anharmonic oscillator

In order to quantitatively measure and compare the extent of thermal expansion in solids, the thermal expansion coefficient can be calculated. This describes the dimensional change that occurs with a change in temperature at constant pressure. Thermal expansion in materials can occur in the vibrational, (isotropic and anisotropic), and non-vibrational, electronic, nuclear etc., forms. Isotropic expansion occurs when material expands evenly in any direction when heated which yields identical values of a property in all crystallographic directions, e.g. polycrystalline aggregates and cubic materials. The expansion in these cases can be measured in terms of a volume thermal expansion co-efficient at constant pressure β [22].

Some materials expand to different extents in a particular direction, i.e. anisotropic expansion. Anisotropic non-cubic materials, for example, have contributions from both thermal stresses and elasticity which results in a wide variety of behaviours. This is defined as the linear expansion, where the co-efficient of linear thermal expansion will be measured is σ. The underlying vibrational mechanisms can sometimes be elucidated by computer simulation techniques, (e.g. notably quasi-harmonic lattice dynamics) and since expansion is distributed unequally among the three axes and if the symmetry is monoclinic or triclinic even the angles between these axes are subject to thermal changes. In such cases it is necessary to treat thermal expansion as a tensor that has up to six independent elements. A good way to determine the elements of the tensor is to study the expansion by powder diffraction

2.2.2 The co-efficient of volumetric expansion

Expansion of volume is measured in terms of the fractional increase in volume per unit rise in temperature. The volumetric thermal expansion coefficient is a thermodynamic property of a substance [23], given by equation 2-5

$$\beta = \frac{1}{V}\left(\frac{\partial V}{\partial T}\right)_p$$

$$- = -\frac{1}{P}\left(\frac{\partial \rho}{\partial T}\right)_p \qquad \textbf{1-5}$$

where T is the temperature, V is the volume, ρ is the density and derivatives are taken at constant pressure P; β measures the fractional change in density as temperature increases at constant pressure.

The expansion of a crystalline material occurs only when the force field of the crystal deviates from a perfect quadratic. If the force field is perfectly parabolic, granular

2.2.3 The co-efficient of linear thermal expansion

This is the quantification of expansion of a material with temperature in terms of increase or decrease of a linear dimension. The coefficient of linear thermal expansion, σ, of any material can be defined as the fractional increase in length, (linear dimension), per unit rise in temperature. Typically ceramics have a lower σ values than metals and materials with higher melting points have lower thermal

expansion co-efficient [24]. In the literature it is generally calculated in two ways; in a temperature range or at a single point temperature.

Over a temperature range

For a material at initial length (L_o) and temperature (T_o) with expansion upon T_1 to length L_1 and T_2 to length L_2, according to the figure 2.5

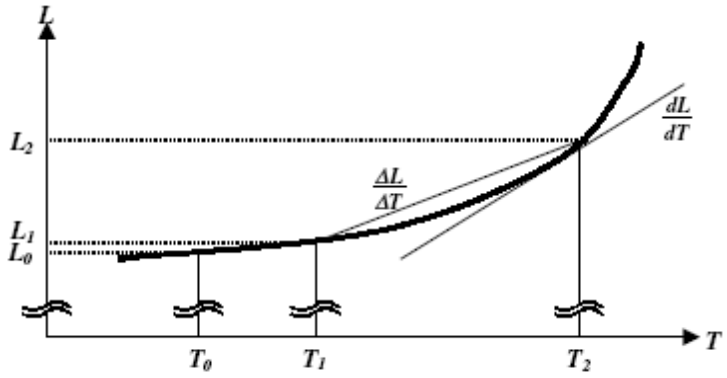


Figure 1.5 Change in length, L, of a sample of material as a function of temperature, T [25]

We define σ as a change in length with temperature change i.e. the gradient between two points, also called the mean coefficient of thermal expansion σ_m,

$$\sigma_m = \frac{\left(\frac{L_2 - L_1}{L_0}\right)}{T_2 - T_1} \qquad 1\text{-}6$$

$$- = \frac{1}{L_0}\left(\frac{\Delta L}{\Delta T}\right)$$

Over a single temperature

The more commonly used measure of thermal expansion is β also called the true coefficient of linear thermal expansion [23-26]. This is the derivative dL/dT at a single temperature. This is the slope of the tangent to the curve of length versus temperature as shown in figure 1

$$\sigma_t = \frac{dT/L}{dT} \qquad 1\text{-}7$$

$$- = \frac{1}{L}\frac{dL}{dT}$$

For an isotropic material, the true coefficient of volumetric thermal expansion is equal to three times the true coefficient of linear thermal expansion [27-28]

$$\beta = 3\,\alpha\,t \qquad 1\text{-}8$$

While this holds for coefficients defined at a single temperature, the relationship between volumetric and linear coefficients defined over a temperature range is more complex [23, 29].

2.2.4 Negative thermal expansion

There is an unusual phenomenon that has been observed with certain ceramic materials, i.e. the size of the material decreases with increasing temperature. This is termed negative thermal expansion. A classical example of such behavior would be from water to ice

2.2.3.1 Thermal expansion of ice

Ice floating on water is a well-known phenomenon. Materials usually adopt a dense, efficient atom-packing arrangement when they crystallize. Water has a hydrogen-bonded network which causes ice crystals to adopt an open architecture with a lot of empty space, leading to the floating ice cube phenomenon Water just like most materials becomes denser as it gets colder until the temperature reaches about 4 °C, shows the water decreased in density on cooling below 4 °C, figure 1.2.4.1. The slope of density versus temperature at any given point gives the water's coefficient of

thermal expansion (CTE) at temperature. Below 3.97 °C, this coefficient is less than zero [30]

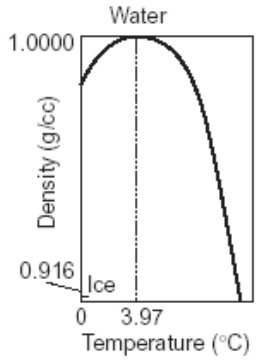


Figure 1.6 : Diagram of water molecules and the density plot as it freezes. Water contracts as it gets colder until it reaches 3.97 °C, then forms an open crystal structure that causes it [31]

Negative thermal expansion has been observed in zirconium tungstate and lead titanate. As it is heated up to its ferroelectric-para Electric phase transition, the M-O bond decreases in length. As it contains a highly distorted Ti or Zr-O octahedra, this then leads to a decreased cell volume as the temperature is increased. Scientists have studied lead titanate in more detail, along with many other related perovskites. These materials can be used in controlling the overall thermal expansion of various mixed metals [32]. There are several different mechanisms that have been used to explain negative thermal expansion, $BaTiO_3$, ZrW_2O_8. The negative thermal expansion occurs over a wide range (0 -1050 K) and co-efficient of -9 pm / K, $PbTiO_3$ and some

other AMO_3 and AM_2O_8 oxides [33-50]. These materials all have perovskite structures and the negative expansion occurs just below their cubic- to -tetragonal phase transition.

2.2.3.2 Mechanisms of negative thermal expansion

The negative expansion occurs due to that metal-oxygen bond distances a decrease in polyhedra as it becomes regular with increasing temperature from its low temperature tetragonal form [19]. The effect is due to the fact that anion-anion repulsions that are minimized as polyhedra become regular.

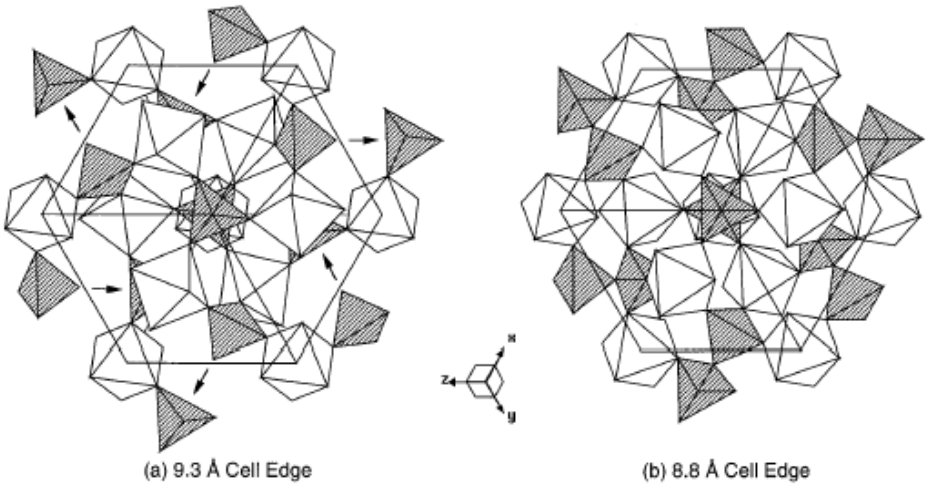


Figure 1.7: Diagram showing the framework of ZrW_2O_8 perovskite during negative thermal expansion [51]

The second mechanism is caused by a normal positive thermal expansion of certain M-O bonds [48]. These can be seen in cordierites ($Mg_2Al_2Si_5O_{18}$), β-eucriptites ($LiAlSiO_4$) and NZP ($NaZr_2P_3O_{12}$) materials with hexagonal structures that show anisotropic thermal expansion. Expansion occurs in the weaker Mg-O, Li-O and Na-O bonds with negligible expansion occurring in the stronger Si-O, Al-O and Zr-O bonds. The invariance of oxygen-oxygen distances of a shared edge or face in linked octahedral and tetrahedral causes thermal expansion to occur only along the *a* and *b* axes in cordierite and β-eucriptite and along the c axes in the NZP. As these sheets of edge-shared polyhedra expands along *a* and *b* axes they are pulled together in the c axes resulting in smaller net volumes [52].

Another mechanism of negative thermal expansion is based on interstitial cations within a network. Due to temperature increase these cations change sites. This can be observed in β-eucriptites where the Li^+ cation situated on the tetrahedral site moves to the octahedral site with temperature increased and thus there is a reduction in volume [53].

A fourth mechanism is based on transverse thermal motion of oxygen atom in the M-O-M bonds [19]. When the M-O bond is strong there would be negligible positive thermal expansion, but when the oxygen molecule is given enough energy to vibrate

about its axes and since there will not be any expansion due to the strong bonds, the vibration is perpendicular to the line joining the two metal atoms. This vibration pulls the metals together [53] as illustrated in figure 2.8

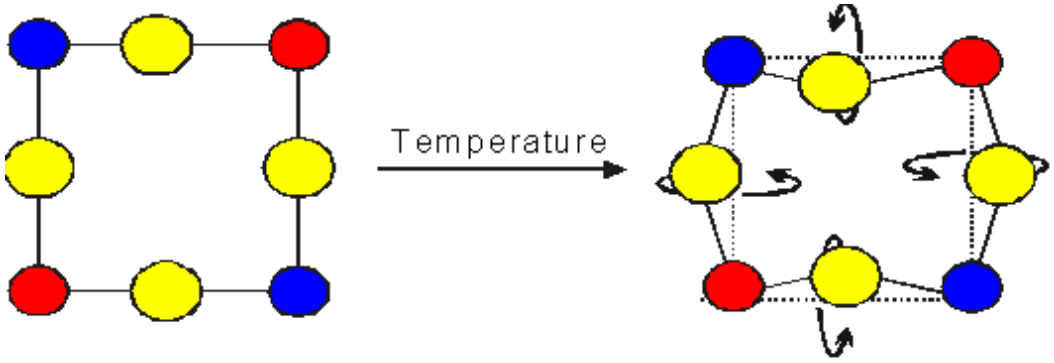


Figure 1.8: Diagram showing the straight and vibrational mode of the M-O-M bond, the arrows showing the vibrational movement of the oxygen

2.3 Experimental measurement techniques

In all definitions of the coefficient of thermal expansion, two quantities have to be measured; displacement and temperature. There are different methods that could be employed to measure thermal expansion by measuring displacement versus a temperature profile. The most commonly used being mechanical dilatometry, optical and diffraction techniques.

Mechanical dilatometry is a technique for measuring displacements resulting from a sample with increasing temperature and mechanically transmitting this to a sensor away from the heat. This results in a plot of displacement against temperature where CET can be calculated. The most common arrangement is the push rod dilatometer [54-56]. A specimen is enclosed in a furnace and two rods in contact with opposite face of the specimen are aligned side by side and parallel to the direction of the expansion, figure shows the schematic of the arrangement [54].

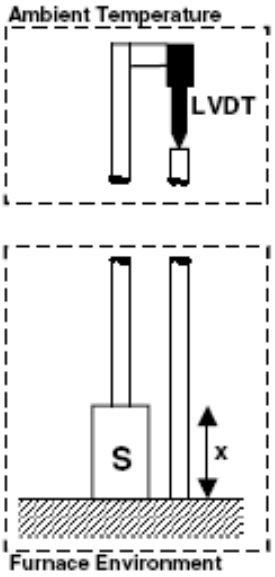


Figure 1.9: Schematic of a push rod mechanical dilatometer for thermal expansion measurement of specimen, (S)

A differential dilatometer [57] uses two specimens, of which one has to be a reference material and the other the examined one. There are other variations of the

dilatometer which are based on the same principles and which can be applied to materials for thermal expansion measurement [58-60]

The optical techniques can be defined as techniques in which the dimensional changes in a test-piece with increasing temperature can be measured optically with techniques that can be divided into three main categories. The first involves the creation of an image of a specimen or of relevant parts of it, and determination of spatial movement of either of the ends or of some clearly defined marks along its length. This generally requires the optical path to be perpendicular to the displacement direction. Examples of this technique include the so-called twin telemicroscope method [61-62]. The second group is based on optical interference measurements [63-64], and differs fundamentally from the first in that the optical path is parallel to the direction of displacement that is being measured. By calculating the path difference between beams reflected from opposite surfaces of the specimen, the displacement can be determined in terms of the wavelength of the light used. The third group employs speckle interferometry [65 - 67]. This relies on the formation of an interference pattern on the surface of the specimen itself, and then the changes in this pattern then enable the calculation of the displacement.

Diffraction techniques involve measurements of the crystal lattice parameter of a material at different temperatures and can be used for the calculation of the thermal expansion coefficient. The bulk of these studies have been based on the diffraction of x-rays from crystal planes [29, 68-70]. The specimen, in the form of a powder, polycrystalline wire or rotating crystal, is enclosed in a suitable furnace. A beam of monochromatic x-rays is then directed on to the specimen and the angles at which the beam is scattered recorded either by means of a cylindrical Debye–Scherrer camera with film surrounding the specimen or by measuring the intensity of the beam as a function differention of angle using a diffractometer. This technique is particularly suitable for small samples and where the material to be studied is very weak. For anisotropic materials the variation in expansion with different directions within the crystal lattice can also be determined [69-72]. A potential drawback to the technique is the fact that the technique does not directly measure the increase in lattice parameter, but rather relies on the subtraction of two separate measurements of this quantity Accurate measurement of the temperature of the small sample and the elimination of temperature gradients is also difficult. Some workers have attempted to measure the temperature by performing diffraction on a reference material with known expansion characteristics [73], which can be mixed in with the material under investigation if it is in powder form. the difference between the thermal expansion coefficient of the bulk and that

of the lattice has been estimated to be approximately 1.5 × 10−6 K−1 for copper at its melting point [29], which would represent a percentage difference of around 6%.

2.4 Characterization X-Ray Diffraction

An effective way of studying the atomic structure of most materials is by means of diffraction techniques and since most materials of interest cannot grow into large crystal for single crystal studies, powder diffraction techniques need to be applied. Rietveld refinement on the powder patterns are then done to model the crystallographic parameters and hence the structure of the material.

X-ray diffraction is one of the most important characterization tools used in solid-state chemistry and materials science. It can be used to determine the size and the shape of the unit cell for any compound. X-rays are electromagnetic radiation with wavelength of about 1 Å (10-10 m), a size similar to that of an atom. Powder X-ray diffraction has been in use in two main areas: for the fingerprint characterization of crystalline materials and to the determination of their structure. Each crystalline solid has its unique characteristic X-ray powder pattern governed by Bragg's law ($2d \sin\vartheta = n\lambda$) [74] which may be used as a "fingerprint" for its identification. Once the material has been identified, structural models to perform Rietveld refinement may

be used to determine its structure, i.e. how the atoms pack together in the crystalline state and what the interatomic distance and angles [75].

Rietveld refinement uses least-squares refinement methods, which are carried out until the best fit is obtained between an entire observed powder diffraction pattern and a calculated pattern from simultaneously refined models of crystal structure, diffraction optic effect, instrumental factors and other characteristics as may be desired and can be modelled [76]. Crystal structure information is gained for samples that are difficult or otherwise impossible to synthesize in a form suitable for single crystal analysis.

2.4.1 Powder X-ray diffraction

In relation to other methods of analysis such as wet or gravimetric, chemical techniques, various electron microscopy techniques (SEM, TEM), Rutherford back scattering etc., powder diffraction allows for fast and non-destructive analysis of multi-component mixtures without the need for extensive sample preparation. This alone makes this technique useful unknown materials and characterize them in fields such as metallurgy, mineralogy, forensic science, archeology, condensed matter physics, and the biological and pharmaceutical sciences [77].

The methodology used in X-ray crystallization is mainly in figure 2-10. A sample for PXRD study contains a large number of individual crystallites which are subjected to

an incident X-ray beam. The X-ray beam after interacting with the sample is selected as cones of individual beams. The individual single crystal spots become smeared out into rings of different intensities. The powder pattern is then a super position of the 3D single crystal data of each crystallite into a one dimensional observation of diffracted intensities against diffraction angle 2θ [79-80].

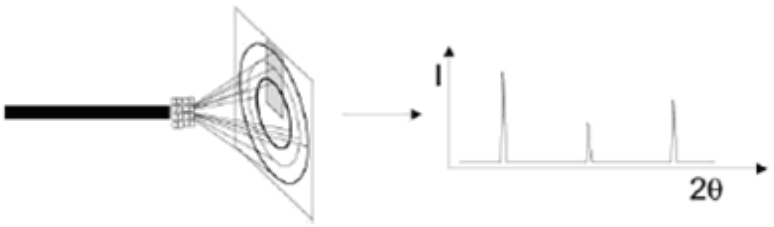


Figure 1.10: Diffraction from a polycrystalline material, where the one dimensional powder patterns can be obtained by scanning a detector across the cones of diffracted intensity [78]

Peak positions in a VRD pattern are determined by the size and shape of the unit cell of the material present, via the Bragg equation; n λ = 2d Sin θ. Peak intensities are determined by the atomic positions within the unit cell, though one must also account for accidental overlap in 2θ of different reflections and any possible preferred orientation of crystallites within the sample. For a multiphase sample one determines one set of reflections due to each phase, which leads to the classical use of powder methods for qualitative or quantitative phase analysis [80].

More recent advancement in powder diffraction instrumentation has lead to measurement of powder patterns in-situ while varying different environmental parameters for new applications. These include measurements over time which can be applied to give information about the progress of reactions in the solid state. This given information similar to that a solution chemist might obtain from NMR/GCMS measurements during experiments [80].

An example of the use of in-situ diffraction methods for monitoring progression of reactions was the work involving the synthesis of $CaTiO_3$ [81]. This study was aimed at investigating the rate of $CaTiO_3$ formation, product purity and the microstructural characteristics. Variable temperature X-ray powder diffraction data were collected and analyzed by multiphase Rietveld refinement of materials obtained from calcined mixtures of $CaCO_3$ and TiO_2 with and without prior mechanical activation. Figure 1.11 shows powder patterns from this study at different temperatures.

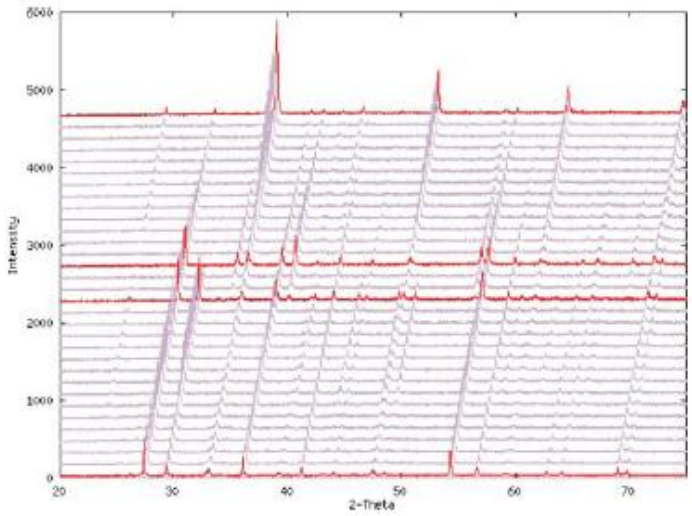


Figure 1.11 : Powder diffraction data recorded on heating the non-activated mixture of $CaCO_3$ and TiO_2. Data at increasing temperatures have been offset vertically.

Without mechanical activation, the sample at room temperature consisted of $CaCO_3$ and TiO_2, and a small amount of $CaTiO_3$ presumably formed during short calcination experiments. $CaCO_3$ decomposition began at 600 ^{o}C and was completed at 800 ^{o}C, when $CaTiO_3$ formation ensued. The final product at 1100 ^{o}C contained about 10% unreacted material.

Other applications include variation in pressure which can be used to analyze a material's behaviour under extreme pressure conditions. Example would be the use of diamond anvil cell to create high pressure conditions in a manner such that a powder pattern can be measured, in-situ by varying the temperature. This approach

can be used in many applications such as investigation of polymorphism, solid state kinetics as well as thermal expansion, contraction and conductivity.

Polymorphism is the ability of a substance to crystallize in different structured forms in the solid state, and it is of great importance since different polymorphs of the same chemical compound can have very different macroscopic properties. For pharmaceutical molecules, the presence or absence of therapeutic activity can sometimes be completely determined by the crystalline form present. In-situ diffraction studies can be used to identify new polymorphs of materials that are unstable under normal conditions. Diffraction methods, in contrast to the complementary techniques of solid state NMR, hot stage microscopy and thermal analysis, give one the ability to solve the structures of the new polymorphs and provide full 3D structural information on transitions [82-84].

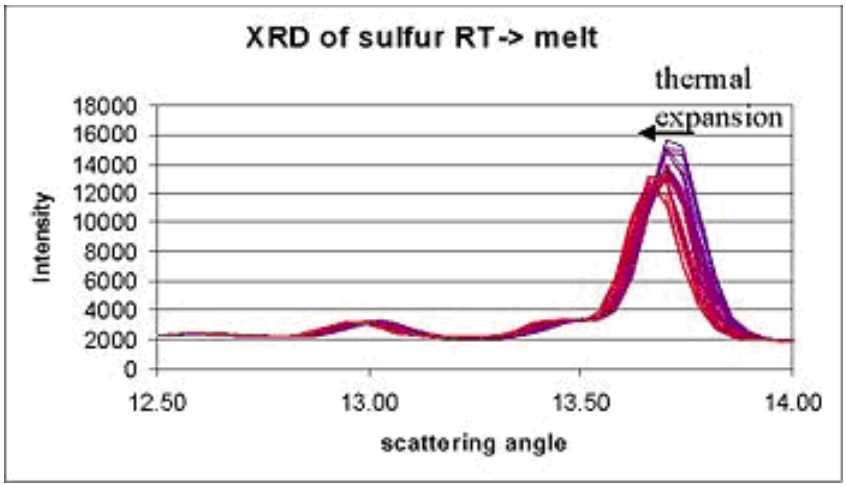


Figure 1.12: Showing change in scattering angle, θ, which was used in calculating the thermal expansion behaviour of sulphur [**85**]

Changes in unit cell parameters can also be used to obtain significant insight into the properties and performance of materials. As these thermodynamic variables are changed, the observed diffraction peaks will migrate continuously to indicate higher or lower lattice spacing as the unit cell distorts. This allows for measurement of such quantities as the thermal expansion tensor and the isothermal bulk modulus, as well determination of the full equation of state of the material [86]. Figure 1.12 shows an example where the thermal expansion data for sulphur were determined using diffraction data.

2.4.2 Rietveld Refinement

The Rietveld method was proposed in 1968 by Hugo Rietveld, from neutron powder diffraction pattern to estimate intensities, shape and 2θ positions of peak within a powder diffraction pattern..

The neutron and X-ray diffraction of powder samples results in a pattern characterized by peaks in intensity at certain positions. The height, width and position of these peaks can be used to determine many aspects of the materials structure.

This method approaches a refinement by the use of least squares to calculate the theoretical line profile until it matches the measured profile. This makes method able to deal reliably with strongly overlapping reflections, thus making the discovery of this technique a significant step forward in the diffraction analysis of powder samples [88]

A Rietveld refinement, based on a mathematical model of the crystal structure, is used to obtain the best fit between an observed and a calculated powder diffraction pattern [76], The calculated pattern is dependent on a number of parameters, which account for sample characteristics such as atomic positions and unit cell parameters, and instrument factors such as the Lorentz-polarisation (LP) factor and the zero point error. Whereas the intensity of the Bragg reflections is dependent on the

atomic parameters, their 2ϑ positions are dependent on the cell dimensions, sample absorption, sample height and instrument zero point error.

Table 1.1: list of parameters and corrections refined during Rietveld refimenet

Peak profile parameters	Error correcting parameters
Cagglioti parameters u, v, w	Zero shift
Pseudo-voigt or other profile parameters	Specimen displacement
Asymmetry correction	Absorption
Anisotropic broadening	Extinction, Porosity

The overall shape of each peak obtained from a powder diffraction pattern results from the material under examination. It is also influenced by other factors ksuch as the characteristics of the X-ray beam, the experimental arrangement, the sample size and the sample shape. These instrumental factors can be insignificant when high resolution XRD and synchrotron sources are used. The size of the crystallite and its strain account for the broadening of a profile, while flat specimen error results in the asymmetric broadening of a profile

The profile breadth, H_k, is expressed by the full width at half maximum (FWHM) of the Bragg reflection as

$$H_k = U\tan^2\theta_k + V\tan\theta_k + W \qquad \text{1-9}$$

U, V and W are Caglioti [89] instrumental line width parameters for the k_{th} Bragg reflection. A 2θ dependence of the peak width from equation 1-9 can be extrapolated, to show that the higher 2θ angles have broader peaks

The Profile breadth is dependent on the radiation source and can be symmetric or asymmetric in nature. The profile shape is described by the profile shape function, which approximates the effects of both structural and instrumental features on the sample, denoted Φ. The traditionally used functions for peak shape are the Gaussian [90], and Lorentzian [90], represented in equations 2-10 and 2-11

$$\Phi = \frac{(4\ln 2)^{\frac{1}{2}}}{(H_k\pi)^{\frac{1}{2}}}\exp\frac{-4\ln 2(2\theta i - 2\theta_k)^2}{H_k^2} \qquad \text{1-10}$$

$$\Phi = \frac{2/(H_k \pi)}{1 + 4\left((2\theta_i - 2\theta_k)^2 / H_k^2 \right)} \qquad 1\text{-}11$$

where G and L are representations of the calculated Gaussian and Lorentzian functions respectively.

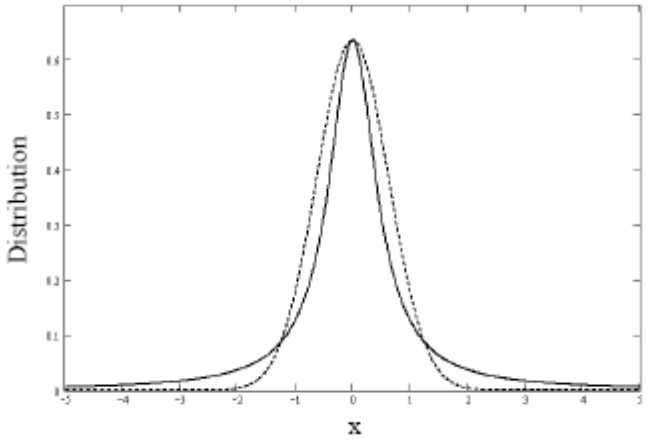


Figure 1.13: Comparison between Gaussian (dashed) and Lorentzian (solid) distributions. The functions of the two distributions are given in Eqns. 2-10 and 2-11 respectively [90].

These days a Pearson VII and pseudo-Voigt function are the most commonly used function to describe the shape of a Bragg peak [91].

Pseudo-Voigt is a linear combination of Gaussian and Lorentzian components, with an additional function which describes peak asymmetry due to axial divergence of the diffracted beam at low-angle [92] The Pseudo-Voight Function, where η represents the mixing parameter is shown in equation 2-12

$$\Phi = \eta L + (1+\eta)G \qquad 1\text{-}12$$

Peak shape varies with 2ϑ and is governed by both the sample and by the instrument. This function is much easier to compute and will converge easily during a refinement. Its physical meaning has been questioned when compared to the Pearson VII function, because the function does not define a variance in its computation [93].

The Pearson type VII function has been found to describe the Kα peak shape to a good approximation [91], with form shown in equation 2-13

$$\Phi = a\left[1+\frac{(x-d)^2}{b^2}\right]^{-m} \qquad 1\text{-}13$$

where (d, a) are the coordinates of the peak maximum, exponent m is a shape factor that determines the rate at which the tails fall, and b is proportional to the full width at half-maximum (FWHM) = $2b(2^{1/m} - 1)^{1/2}$. When the exponent m = 1, the shape becomes Cauchy; when m = 2, modified Lorentzian; and when m = ∞, Gaussian.

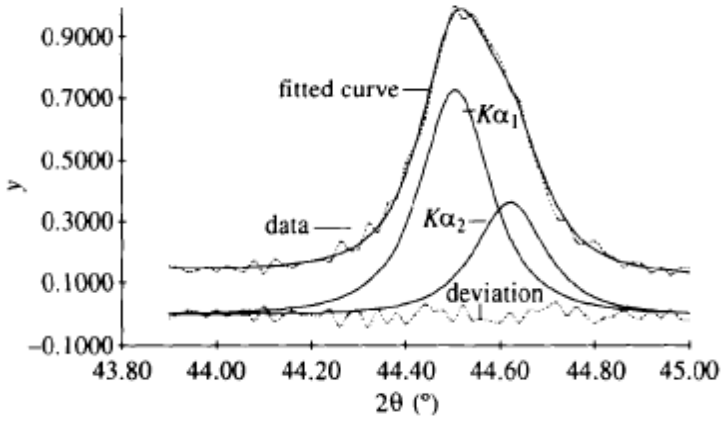


Figure 1.14: plot showing the curve fitting and deviation used in Pearson VII function

Crystallographic texture or preferred orientation can cause serious systematic errors in quantitative phase analysis of crystalline materials using powder diffraction data. In the ideal case crystalline orientations are represented equally in a powdered

sample. The resulting orientation averaging causes the three dimensional reciprocal space that is studied in single crystal diffraction to be projected onto a single dimension [94-96]. The three dimensional space can be described with (reciprocal) axes x*,y* and z* or alternatively in spherical coordinates q,ϕ*,χ*. In powder diffraction intensity is homogeneous over ϕ* and χ* and only q remains as an important measurable quantity. In practice, it is sometimes necessary to rotate the sample orientation to eliminate the effects of texturing or preferred orientation and achieve true randomness

It is possible to extract preferred orientation information from such patterns if the pattern for a randomly oriented specimen can be modelled, or simulated, from knowledge of the crystal structure parameters and various other factors (*e.g.* line broadening) which influence the pattern.

Preferred orientation may lead to variation in peak intensities from that which is predicted for a completely random sample distribution. Rietveld introduced a correction function that allows for moderate cases of preferred orientation [97]. Today the preferred orientation is usually modelled with the Marsch Dollase [98-99] as the Spherical Harmonic [100] function:

$$P_k = \left(\frac{r^2 Cos^2\alpha + Sin^2\alpha}{r} \right)^{-\frac{3}{2}} \qquad 1\text{-}14$$

where α is the angle between the (hkl) planes and the preferred orientation vector, and r is an adjustable parameter.

$$A(h,y) = 1 + \sum_{\ell}^{L} \frac{4\pi}{2\ell+1} \sum_{m=-1}^{i} \sum_{n=-1}^{\ell} C_{\ell}^{mn} K_{\ell}^{m}(h) K_{\ell}^{n}(y) \qquad 1\text{-}15\ [100]$$

The two harmonic terms, and ~(y), take on values according to the crystal and sample symmetries, respectively, and thus the two inner summations are over only the resulting unique non-zero harmonic terms [101].

2.4.2.1 Extraction method

Extraction methods are used to find information needed to perform a structural refinement when nothing is known about the compound under analysis. There are two extraction methods that are widely used for extraction of peak intensities; the Le Bail [102] method based on the original Rietveld method for determining

observed structure-factor magnitudes and the Pawley [103] method which is a constrained non linear least squares approach.

Rietveld proposed a summation approach to the evaluation of the observed structure-factor magnitude for the overlapping of reflections. This approach was based on the fact that the peak area is proportional to the square of the structure-factor magnitude. The method reduced the problem of finding peak to adding together the background-subtracted profile points and for overlapping peaks to calculating peak contribution for that reflection divided by the sum of the calculated peak values for each peak contributing reflection. The Le bail method is the extension of the method but starting with arbitrary fixed intensity values. The integrated intensity value is calculated according to:

$$I_h = \frac{\sum_i (Y_{obs}(i) - Y_b(i)) * Y_{calc}(I,h)}{\sum_k Y_{calc}(i,k)} \qquad 1\text{-}16 \quad [102]$$

where Y_{obs} (i) is the experimental count; Y_b (i) is the background contribution; Y_{calc} (I, h) is the calculated count due to the h reflection contribution. This method uses a first calculated peak to calculate the second peak recursively.

The Pawley method minimizes the sum of squares of the differences between the calculated and observed profiles. The integrated intensities, cell parameters, and the parameters modelling peak shape and background are the refinable parameters. There are positivity constraints used in this method to overcome the problem of unstable least squares that lead to negative integrated intensities caused by peak overlap.

2.4.2.2 The refinement strategy

Rietveld refinement is a method that fits a structure-background-profile model to experimental data. Therefore, there exist lots of potential for “false” minima, diverging solutions, etc. For this reason the model profile must be chosen to be as close in value to the observed profile. The model does however not need to be exact since the refinement will follow an iterative process in which changes are applied to the initial parameters in order to improve the fit. This results in the refinement strategy that requires refinement of the most important variables first, then more

variables would be added until an adequate solution is found. These parameters are the scale factor, zero shifts or specimen displacement but not both, linear background, lattice parameters, more background, peak width, (w), atom positions, preferred orientation, isotropic temperature factor B, then u, v, and other profile parameters, anisotropic temperature factors [104].

R is the quantity that is minimized during least-squares or other fitting procedures; R_{wp} is weighted to emphasize intense peaks over background. R_{exp} estimates the best value R for a data set an evaluation of how good the data are R_{Bragg} tries to modify the R for a specific phase [76, 105 - 107]

All of the above parameters have to be considered for refinement if the best agreement between the observed and calculated models is to be achieved. The quality of the model can be shown graphically in terms of a difference profile plot or numerically in terms of residual factors or *R* indices . The weighted-profile *R*-factor is defined in Equation 2-17, where, $y_i(obs)$ is the observed intensity at step *i*, $y_i(calc)$ the calculated intensity and w_i, the weight [76].

$$R_{wp} = \left\{ \frac{\sum_i w_i \left[y_i(obs) - y_i(calc) \right]^2}{\sum_i w_i \left[y_i(obs) \right]^2} \right\}^{1/2} \qquad \text{1-17}$$

The numeric value of R_{wp} can be misleading when high backgrounds are observed, as a large proportion of the intensity is accounted for by the background function, so the denominator will be large and R_{wp} turns out to be small despite a poor structural model. A good refinement is one where R_{wp} approaches the statistically expected R value, R_{exp}, defined in Equation 2-18; N is the number of observations and P the number of parameters. R_{exp} reflects the quality of the data [76].

$$R_{\text{exp}} = \left[(N - P) \Big/ \sum_i^N w_i y_i(obs)^2 \right]^{1/2} \qquad \text{1-18}$$

From the ratio of the Equations 2-17 and 2-18, χ^2 is a more concise way of describing the quality of a refinement.

$$\chi^2 = R_{wp} / R_{\exp} \qquad 1\text{-}19$$

However, χ^2 strongly depends on the length of time spent collecting data; rapid scans imply that errors will be dominated by counting statistics and R_{exp} will be large so χ^2 could be less than 1 [76].

2.4.2.3 Rietveld software

There are many free and commercially available Rietveld referenced programes, each have advantages and difficulties based on the functionality and required, end use, (e.g. solving for different parameters like size and strain), crystallite sizes, quantitative phase analysis and structure determination

One of these programs is known as the General Structure Analysis Software (GSAS), suite one of the oldest refinement programs. It was written in the 1970's as a structure refinement program, not as a Rietveld refinement program. This is a freely distributed program. List of other common software is shown in Table 1.2. In this

report all Rietveld refinements were conducted using the Bruker TOPAS software [108].

Table 1.2: Listing some of the available Rietveld software

Free	Commercial
GSAS + ExpGUI	PANalytical HighScore Plus
Fullprof	Bruker TOPAS (also an academic)
Rietica	MDI Jade or Ruby
PSSP (polymers)	
Maud	
Powder Cell (limited refinement)	

TOPAS consists of two modes of operation; *the Interface* and *Launch (Input)* modes. The former mode allows pattern fitting *via* a graphical user interface. *Launch (Input)* mode was used exclusively in this throughout as it permits rapid, multiple least-squares refinements and contains more functionality. An input file is set up which contains the space group and cell information, and starting values for all the peak positions, background, instrument and atomic parameters. The real bonus of using *TOPAS* for Rietveld work is that all parameters can be simultaneously refined without causing divergence in the model. More data at many different temperatures can be refined relatively quickly. In a typical variable temperature refinement, the first range was refined using *TOPAS* in *Launch* mode using an input file as mentioned

above. This first refinement was then used as a seed for those to be performed at all remaining temperatures. The output file for the first refinement was copied to the input file for the subsequent refinement and a round of least-squares cycles performed until convergence was observed. Relevant refined parameters were written out in a text file and the whole process repeated again. The process was automated using a routine called *Multi-TOPAS* [108].

At the end of the multiple refinements, the results file showing the temperature dependence of the refined parameters analyzed in Microsoft *Excel*. The most important plot we discussed in the main chapters of this thesis.

2.5 REFERENCES:

1. M.N. Al'Bov, Z. Vsesoyuz, mineralogy, Obschkeststva, Mem. Soc. Russe mineral, 1954, **83**, 148
2. P. D´ıaz-Leyva, E. P´erez, J.L. Arauz-Lara, Brownian motion of optically anisotropic particles in weak polymer gels, *Rev. Mex. F´ıs.* 2004, **50** (6), 633
3. D. Segal, *Making advanced ceramics*, Chemistry in Britain, 1989
4. J. T. Kloprogge, M.L. weier, L.V. Duong, R.L. Frost, Microwave assisted synthesis and characterization of divalent metal tungstate nanocrystalline minerals: ferberite, hubnerite, sanmartinite, scheelite and stolzite, Mat. Chem. and Phys., 2004, **88**(2-3), 438
5. D. Segal, *Chemical synthesis of advanced ceramic materials*, Cambridge: Cambridge university press, 1989 (1991 printing)
6. M.N Rahaman, *Ceramic processing and sintering 2nd addition*, Marcel Dekker, Inc., New York, USA, 2003
7. H. Chen, H. Chang**,** Synthesis of nanocrystalline cerium oxide particles by the precipitation method, Ceramics International, 2005, **31**(6), 795
8. J.L. Woodhead, D. Segal, *Sol-gel processing*, Chemistry in Britain,1984
9. H. Schmidt, Chemistry of materials preparation by the sol-gel process, Journal of non-crystalline solids, 1988, 51
10. C.W. Turner, Sol-gel process – principles and application, Ceramic bulletin, 1991, **70**(9)
11. G. Wilson, A. Patel, Recent advances in sol-gel processing for improved materials synthesis, Materials science and technology, 1993, **9**
12. A. Kursumovic; E. Babic, D. Damjanovic, N. Ilic, Z. Marohnic, M. Prester, Physical-Properties of $Yba_2Cu_3O_{7-X}$ Superconductor Sintered at Different Temperatures, Journal of Materials Science, 1989, **24**(12), 4370
13. V.R. Caffarena, T. Ogasawara, Synthesis by Citrate method and Characterization of $Ba_3CoCuFe_{24}O_{41}$ Hexaferrite, Acta Micro., 2003, **12**, 71
14. A. Hiromichi, H. Hideyuki, N. Takashi, M. Tsunehiro, K. Hiroyuki, W. Yuji, Synthesis of fine magnetite powder using reverse coprecipitation method and its heating properties by applying AC magnetic field, Materials research bulletin, 2005, **40**(7), 1126

15. Z.C Hum, G.A. Miller, A. Payzante, C. J. Rawn, Homogeneous (co)precipitation of inorganic salts for synthesis of monodispersed barium titanate particles, Journal of materials science , 2000, **35(**12), 2927
16. G. Renaudin; M. Fran Ç ois, Bayerite: Electrochemical Synthesis and Mechanism of Formation, Synthesis and Reactivity in Inorganic, Metal-Organic, and Nano-Metal Chemistry, 1997, **27**, 947
17. W. Jun, Z. Yuejin, Fabrication of $BaFe_{12}O_{19}$ Nanowires by a Hydrothermal Process and Their Magnetic Properties, Modern Physics Letters B, 2006, **20**(7), 359
18. S. Padilla, J. Román, M. Vallet-Regí, Synthesis of porous hydroxyapatites by combination of gelcasting and foams burn out methods, J. Mat. Science: Materials in Medicine, 2002, **13**(12)
19. L. J. Korb, The Shuttle Orbiter Thermal Protection System, Bulletin Am. Ceramic Soc., 1981, **60**(11), 1188
20. E. Grüneisen, *Ann. Phys.*, 1908, **26**, 393
21. K. Röttger, A. Endriss, J. Ihringer, S. Doyle, W. F. Kuhs, *Acta Cryst.*, 1994, **B50**, 644
22. D. L Turcotte, G. Schubert, *Geodynamics*, 2nd Edition, Cambridge, 2002,
23. P. Bruesch, *Phonons: Theory and Experiments*, Springer Verlag, Berlin, Germany, 1982
24. R. Roy, D. K. Agrawal, and H. A. McKinstry: Very Low Thermal Expansion Coefficient Materials. Annu. Rev. Mater. *Sci,* 1989, **19**, 59
25. J D James, J A Spittle, S G R Brown and R W Evans, Negative Thermal Expansion, Meas. Sci. Technol., 2001,**12**, R1
26. T. R. Ravindran, A. K. Arora, and T. A. Mary: High Pressure Behavior of ZrW2O8: Gruneisen Parameter and Thermal Properties. *Phys. Rev. Lett,* 2000*,* **84,** 3879
27. Kirby R K *Compendium of Thermophysical Property Measurement Methods* vol 2, ed K D Maglic, A Cezairliyan and V E Peletsky, New York: Plenum, 1992, **ch. 19**, 549–67
28. T H K Barron, *Cindas Data Series on Material Properties, Volume I-4—Thermal Expansion of Solids,* ed R E Taylor, Materials Park, OH: ASM International, 1998, **ch. 1**, 5
29. Y S Touloukian, R K Kirby, R E Taylor, P D Desai, *Thermophysical Properties of Matter, Volume 12—Thermal Expansion, Metallic Elements and Alloys,* New York: IFI–Plenum, 1975
30. *D. B. Balashov, V. P. Orlov, Thermal anomaly of water. I. Regional boundaries. Entropy. Heat capacities. Zh. Fiz. Khim.* 1983, **57**, 2465

31. N. Mcguire, Negative-coefficient materials can point the way to positive value in the right matrixes, Am. Chem. Soc., 2002, 25
32. V. Heine, P. R. L. Welche, M. T. Dove: Geometrical Origin and Theory of Negative Thermal Expansion in Framework Structures. *J. Am. Ceram. Soc.* 1999, **82**, 1793
33. V. Korthuis, N. Khosrovani, A. W. Sleight, N. Roberts, R. Dupree, W. W. Warren, Negative Thermal Expansion and Phase Transitions in a $ZrV_{2-x}P_xO_7$ Series, Chem. Mater., 1995, **7,** 412
34. N. Khosrovani, A. W. Sleight, T. Vogt, Structure of ZrV2O7 from −263 to 470°C J. Solid State Chem., 1997, **132**, 355
35. J. Graham, A. D. Wadsley, J. H. Weymouth, L. S. Williams, A New Ternary Oxide, ZrW_2O_8, *J. Am. Ceram. Soc.*, 1959, **42**, 570
36. L. L. Y. Chang, M. G. Scroger, B. Phillips, Condensed Phase Relations in the Systems ZrO_2-WO_2-WO_3 and HfO_2-WO_2-WO_3, *J. Am. Ceram. Soc.*, 1967, **50**, 211
37. A. Clearfield, R. H. Blessing, The preparation and crystal structure of a basic zirconium molybdate and its relationship to ion exchange gels, J. Inorg. Nucl. Chem., 1972, **34**, 2643
38. A. Clearfield, R. H. Blessing, The preparation of a crystalline basic zirconium tungstate *J. Inorg. Nucl. Chem.*, 1974, **36**, 1174
39. C. Lind, A. P. Wilkinson, Z. B. Hu, S. Short and J. D. Jorgensen: Synthesis and Properties of the Negative Thermal Expansion Material Cubic $ZrMo_2O_8$, Chem. Mater. 1998, **10**, 2335
40. A. Matsumoto, K. Kobayashi, T. Nishio, K. Ozaki, *Fabrication and thermal expansion of Al-ZrW_2O_8 composites by pulse current sintering process,* 2003
41. H. Holzer, D. C. Dunand, Phase Transformation and Thermal Expansion of Cu/ ZrW_2O_8, J. Mater. Res., 1999, **14**, 780
42. Verdon and D. C. Dunand: High-Temperature Reactivity in the ZrW2O8-Cu System Scripta Mater. 1997, **36**, 1075
43. P. Wilkinson, C. Lind, S. Pattanaik, A new polymorph of ZrW2O8 prepared using nonhydrolytic sol–gel chemistry Chem. Mater., 1999, **11**, 101
44. Lind, A. P. Wilkinson, Seeding and the Non-hydrolytic Sol-Gel Synthesis of ZrW2O8 and ZrMo2O8, J. Sol-gel Sci. Techn., 2002, **25**, 51
45. L. D. Noailles, H. H. Peng, J. Starkovich, B. Dunn, Thermal Expansion and Phase Formation of ZrW2O8 Aerogels Chem. Mater., 2004, **16**,1252

46. Closmann, A. W. Sleight, J. C. Haygarth, Low-temperature synthesis of ZrW_2O_8 and Mo-substituted ZrW_2O_8, J. Solid State Chem., 1998, **139**, 424
47. J. Catafesta, J. E. Zorzi, C. A. Perottoni, M. R. Gallas, J. Alziro, H. da Jornada, Tunable Linear Thermal Expansion Coefficient of Amorphous Zirconium Tungstate, J. American Ceramic Society, 2006, **89**(7) , 2341
48. A.W. Sleight, Thermal contraction, Endeavor, 1995, **19**, 64
49. Martinek, F. A. Hummel, *J. Am. Ceram. Soc.*, 1968, **51**, 227
50. T. A. Mary, J. S. O. Evans, T. Vogt, A. W. Sleight, *Science*, 1996, **272**, 90
51. I.D. Brown, R.D. Shannon, Empirical bond-strength-length curves for oxides, Acta. Cryst. A, 1973, **29**, 266
52. R.M. Hazen, C.T. Prewit, Effects of temperature and pressure on interatomic distances in oxygen-based minerals, Am. Mineral, 1977, **133**, 580
53. A.W. Sleight, Compounds that contract on heating, Am. Chem. Soc., 1998
54. Gaal P S Cindas ed R E Taylor, *Data Series on Material Properties, Thermal Expansion of Solids*, Materials Park, OH: ASM International, 1998, **I-4**, 165
55. J D James, J A Spittle, S G R Brown and R W Evans, A review of measurement techniques for the thermal expansion coefficient of metals and alloys at elevated temperatures, *Meas. Sci. Technol*, 2001, **12,** R1
56. J. Valentich, General Dilatometry, J. Mater. Sci. 1979, **14**, 371
57. P S Gaal, Cindas, *Data Series on Material Properties, Volume I-4—Thermal Expansion of Solids* ed., R E Taylor, Materials Park, OH: ASM International, 1998, 165
58. E E Shpil'rain, K A Yakimovitch, A G Mozgovoi, *Compendium of Thermophysical Property Measurement Methods vol 2*, ed K D Maglic, A Cezairliyan and V E Peletsky, New York: Plenum, 1992, **ch 21**, 601
59. K.D. Sommer, J. Poziemski, Density, thermal expansion and compressibility of mercury, Metrologia., Metrologia., 1994, **30,** 665
60. J. Blumm, J. B. Henderson, Measurement of the volumetric expansion and bulk density of metals in the solid and molten regions, High Temp.–High Pressures, 2000, **32,**109
61. Rothrock B D and Kirby R K 1967 J. Res. Natl Bureau Standards C 71 85–91
62. R.E. Taylor, B.D. Rothrock, R.K. Kirby, *Cindas Data Series on Material Properties, Thermal Expansion of Solids*, Materials Park, OH: ASM International, 1998, **ch 9**, 225

63. T.A. Hahn, *Cindas Data Series on Material Properties,Volume I-4—Thermal Expansion of Solids,* ed, R E Taylor Materials Park, OH: ASM International, 1998, **ch 6**, 181
64. G. Ruffino, *Compendium of Thermophysical Property Measurement Methods vol 1,* ed K D Maglic, A Cezairliyan and V E Peletsky, New York: Plenum, 1984, **ch 18**, 689
65. J.A. Leendertz, Interferometric displacement measurement on scattering surfaces utilizing speckle effect, J. Phys. E: Sci. Instrum., 1970, **3,** 214
66. O.J. Lokberg, J.T. Malmo, G.A Slettemoen, Interferometric measurements of high temperature objects by electronic speckle pattern interferometry, Appl. Opt., 1985, **24,** 3167
67. Kim S, Kim J H, Lee J K and Jarng S S Measurement of thermal expansion coefficients by electronic speckle pattern interferometry at high temperature J. Mater. Sci. Lett., 1997, **16,** 1753
68. McKinstry H A, Huang C Y and McKinstry S T Cindas, *Data Series on Material Properties, Volume I-4—Thermal Expansion of Solids*, ed, R E Taylor (Materials Park, OH: ASM International, 1998, **ch 7**,193
69. Antii M-L, Babushkin O, Shen Z, Nygren M and Warren R 1999 Key Eng. Mater. 164–165 279–82
70. N Suzuki N. T. Kanomata, T. Suzuki, K. Sato, T. Kaneko, M. Yamagishi and S. Endo, Thermal expansion of MnRhP J. Alloys Compounds 1998, 281, 77–80
71. Halvarsson M, Langer V and Vuorinen S 1995 Surf. Coatings Technol. 76–77 358–62
72. Liu Q, An S and Qiu W Study on thermal expansion and. thermal shock resistance of MgO–PSZ, Solid State Ionics, Solid State Ion. 1999121 61–5
73. Merryman R G and Kempter C P, Precise Temperature Measurement in Debye-Scherrer Specimens at Elevated Temperatures, J. Am. Ceram. Soc,1965, 48 202–5
74. N.E. Wilfred, *X-ray diffraction methods*, Wiley, 1966
75. D.L. Bish, S.A. Howard, *Quantitative phase analysis using the Rietveld method*
76. R.A. Young (Ed), *The Rietveld method*, Chester, England: IUCr, Oxford, New York, Oxford university press, 2002 printing
77. B.D. Cullity, *Elements of X-ray diffraction*, Addison-Wesley, 2nd ed., 1977, **Ch 14**
78. J. S. O. Evans and I. R. Evans, Beyond classical applications of powder diffraction, Chem. Soc. Rev., 2004, **33**, 539

79. F.J. Kuellmer, X-ray intensity measurements on perthitic materials: I. Theoretical considerations, Journal of Geology, 1959, **67**, 648
80. V. K. Pecharsky, P. Y. Zavalij, Fundamentals of PowderDiffraction and Structural Characterization of Materials, Kluwer Academic Publishers, Boston, 2003
81. R. Evans, J. A. K. Howard, T. Sreckovic and M. M. Ristic, Mater. Res. Bull., 2003, **38**, 1203
82. R. Evans, J. S. O. Evans and J. A. K. Howard, J. Mater. Chem., 2002, 12, 2648.
83. Mizrahi, J. P. Wignacourt, M. Drache and P. Conflant, J. Mater. Chem., 1995, **5**, 901.
84. J. M. Rubin-Preminger, J. Bernstein, R. K. Harris, I. Radosavljevic´ Evans and P. Ghi, Cryst. Growth Des., 2004, **4**(3), 431
85. J. Wallis, I. Sigalas, S. Hart, Determination of the thermal expansion of orthorhombic sulfur, J. Appl. Cryst., 1986, 19, 273
86. S. Allen and J. S**. O. Evans,** The kinetics of low-temperature oxygen migration in $ZrWMoO_{8,}$ J. Mater. Chem., 2004, **14**(2) , 151
87. D. B. Balashov, V. P. Orlov, Thermal anomaly of water. I. Regional boundaries. Entropy. Heat capacities. Zh. Fiz. Khim. 1983, **57**, 2465
88. H. M. Rietveld, A profile refinement method for nuclear and magnetic structures, Journal of Applied Crystallography 1969, **2**, 65
89. G. Caglioti, A. Paoletti, F. P. Ricci, Choice of Collimator for a Crystal Spectrometer for Neutron Diffraction, Nucl. Instrum. Methods., 1958, **3**, 223
90. R. A. Young and D. B. Wiles, Profile shape functions in Rietveld refinements, *J. Appl. Cryst.*, 1982, **15**, 430
91. M.M. Hall,G. V. Veeraraghavan, H. Rubin, P .G. Winchell, The approximation of symmetric X-ray peaks by Pearsont ype VII distributions, J. Applied Crystallography, 1977, **10**, 66
92. M. Ahtee, L. Unonius, M. Nurmela and P. Suortti, A Voigtian as profile shape function in Rietveld refinement, *J. Appl. Cryst.*, 1984, **17**, 352
93. www.wolfram.com
94. H. Sitepu, Assessment of preferred orientation with neutron powder diffraction data, J. Appl. Cryst. 2002, **35**, 274
95. AI.Tomare, G. Cascarano, C. *Giacovazzo,*A. Gt, Early finding of preferred orientation: a new method. *J. Appl. Cryst.,* 1994, **27**, 1045
96. T. Leventouri, A new method for measuring the degree of preferred orientationin bulk textured YBa2Cu3Ox, Physica C, 1997, **277** , 82

97. J. Bergmann, T. Monecke and R. Kleeberg, Alternative algorithm for the correction of preferred orientation in Rietveld analysis, J. Appl. Cryst., 2001, **34**, 16

98. J. Howarda, E. H. Kisib, Preferred orientation in Debye-Scherrer geometry:interpretation of the March coefficient, J. Appl. Cryst., 2000, **33**, 1434

99. W. A. Dollase, Correction of intensities for preferred orientation in powder diffractometry: Application of the March model, J. Appl. Cryst., 1986, **19**, 267

100. H. Bunge, *Texture Analysis in Materials Science,* London: Butterworth, 1982, 3–118

101. R. B. Von Dreele, Quantitative texture analysis by Rietveld refinement, *J. Appl. Cryst.,* 1997, **30**, 517

102. A. Le Bail, H. Duroy, J.L. Fourquet, Ab-initio structure determination of LiSbWO6 by X-ray powder diffraction, Mat. Res. Bull., 1988, **23**, 447

103. G.S. Pawley, Unit-cell refinement from powder diffraction scans, J. Appl. Cryst., 1981, **14**, 357

104. B. O'Connor, D. Li, Influence of refinement strategies on rietveld phase composition determinations, Denver X-ray Conference, 1998

105. D.E. Cox, R.J. Papoular, Structure refinement with synchrotron data: R-factors, errors and significance tests, Materials Science Forum, 1996, **228**(1,2), 233

106. E. Jansen, W. Schafer, G. Will, R-values in analysis of powder diffraction data using Rietveld refinement, Journal of Applied Crystallography, 1994, **27**(4), 492

107. R.J. Hill and R.X. Fischer, Profile agreement indexes in rietveld and pattern-fitting analysis, Journal of Applied Crystallography, 1990, **23**(6), 462

108. R. W. Karlsruhe, A. A. Coelho, TOPAS. Version 3. Bruker AXS Inc., Germany. Cheary, J. Appl. Cryst. 1992**, 25**, 109

Chapter 3 Instrumentation and data analysis

X-ray data collection was done on a Bruker D8 Advance powder x-ray diffractometer [1] and then analyzed using Bruker Diffract Plus Eva version 3 [2] and modeled using the Rietveld refinement method. The software used for the refinement was the TOPAS version 3 [108-4] Rietveld modelling package.

3.1 Data collection

The structural data collected, were obtained using a Bruker D8 Advance X-ray powder diffractometer equipped with a primary beam Göbel mirror, a radial Soller slit, a VÅntec-1 detector and using Cu-Kα radiation (40 kV, 40 mA). The Soller slit was used to decrease axial divergence to minimise peak shifts and asymmetric broadening. A radial Soller slit precedes the VÅntec-1 detector which collects the diffracted X-rays, in normal, room temperature, reflection mode and also when any of the temperature stages are attached. The diffractometer is equipped with accessories such as a nine sample changer for room temperature measurements and is equipped with a sample spinner to minimize texturing and preferred orientation effects.

The X-ray generator was operated with a copper target X-ray tube with wavelength $K\alpha_1$ 1.544426 Å and $K\alpha_2$ 1.54439Å and all samples were recorded over a range of 5º < 2θ > 140º in 0.007^{o} steps to increase the number of data points and using the scan speed resulting in an equivalent time of 110.4 s per step.

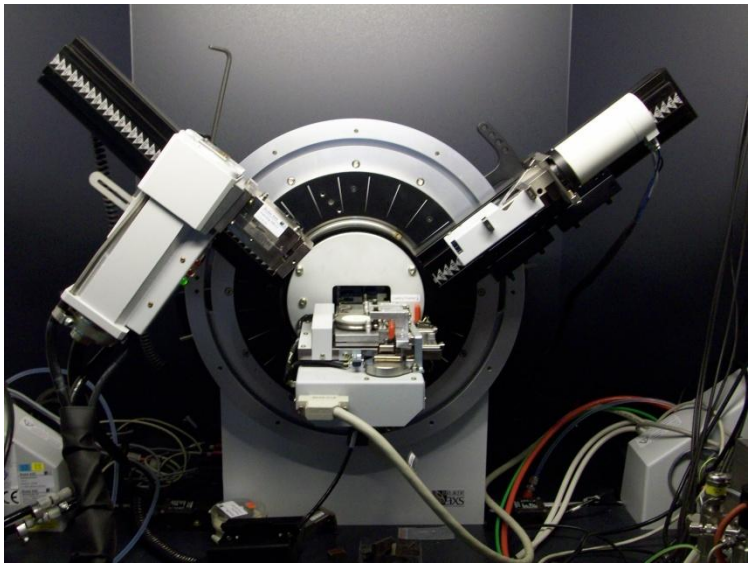


Figure 1.15 A Bruker D8 advance automated X-ray diffractometer which was used for all X-ray measurements

3.2 Rietveld refinement instrument calibration

Before using any structural information from the samples, a calibration measurement and refinement was done to ensure subsequent accurate structural information. This was done using a known standard material, LaB_6 [5], and a Rietveld refinement for instrumental parameters using TOPAS version 3 was performed.

During this validation refinement lattice parameters were kept constant and only the instrumental parameters were refined. The TOPAS input file used in the refinement is shown in appendix disc. The resulting instrumental parameters shown in Table **1.3** were used in the refinement of all the materials described in subsequent chapters for the characterization and thermal expansion studies. Figure **1.17** shows the fit obtained by TOPAS refinement using these instrumental parameters.

Table 1.3: Refined parameters for LaB_6

Refinement fit Parameters	
R_{wp}	5.724
R_{exp}	5.032

1/X Background	1521.567
RS Length (mm)	0.0125
Instrumental Parameters	
Full Axial Model	
Prim. Soller (°)	3
Prim. Soller (°)	3
LP factor	62.3360

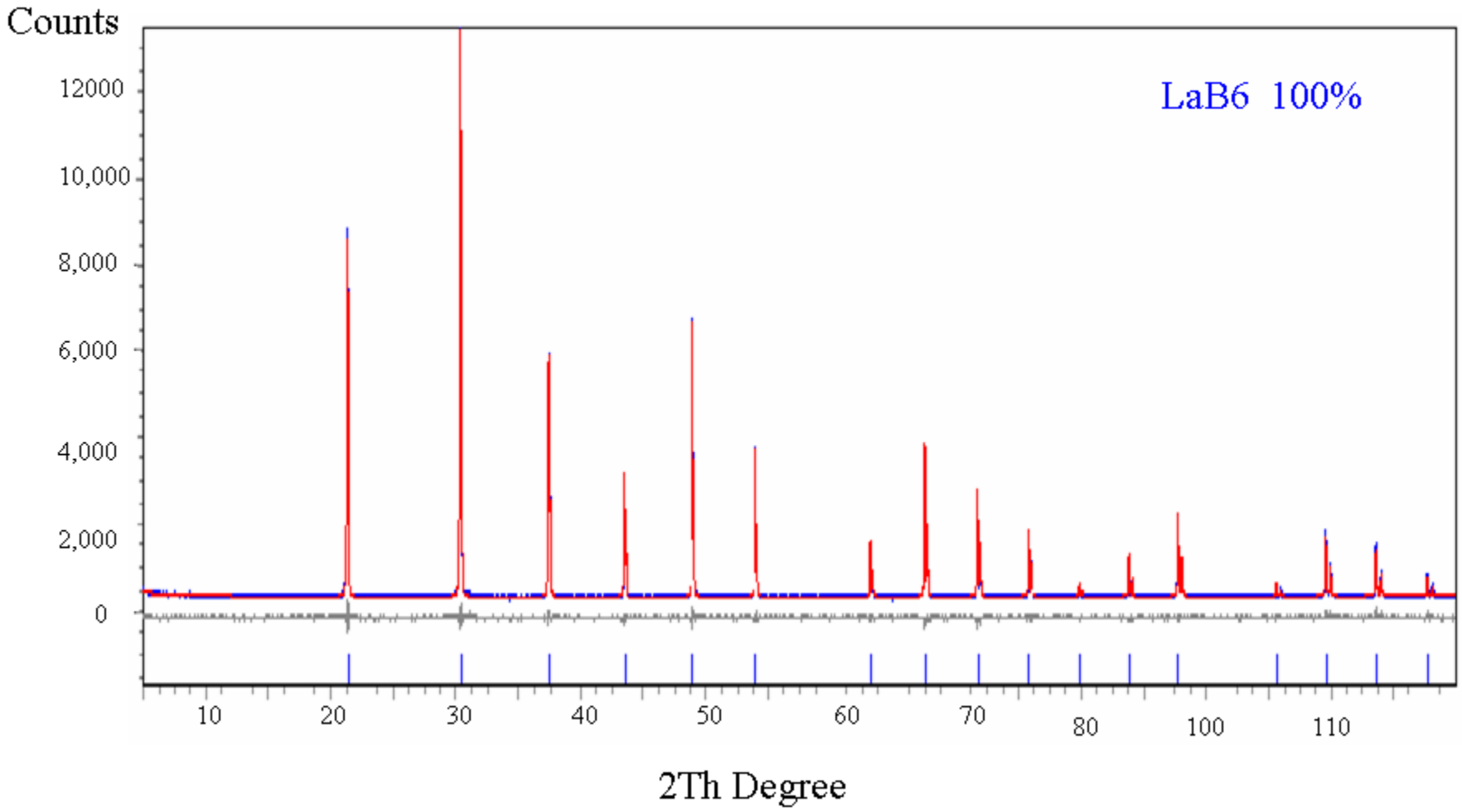


Figure 1.16: TOPAS Rietveld refinement results for LaB_6: fitted pattern (red), experimental pattern (blue) and the difference curve (grey)

3.3 Calibration Of the variable temperature stage

A Bruker D8 Advance diffractometer equipped with a high temperature attachment was used for all the variable temperature measurements. An Anton Paar XRK900 high temperature reaction chamber, shown in Figure **1.17**, was used for the measurements [7-8]. Before definitive structural information could be performed on the samples presented in this thesis, an in-house calibration procedure was performed. This was done to ensure accurate structural information would be obtained.

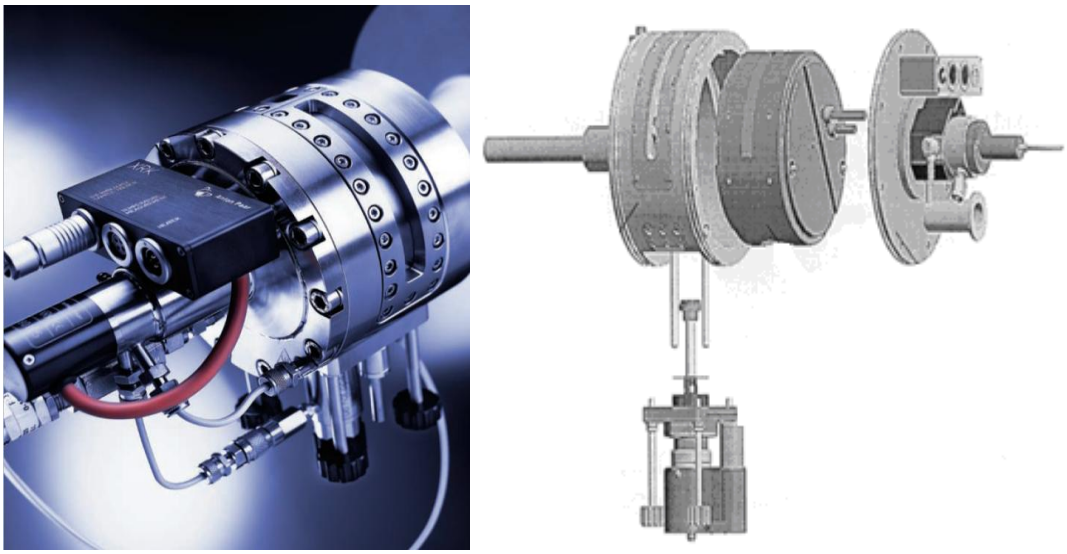


Figure 1.17: Picture and schematic diagram of the Anton Paar XRK900 high temperature reaction chamber [6]

The Anton Paar XRK900 reaction chamber is the only reaction chamber for lab based X-ray diffraction experiments on the market that allows one to perform studies of solid state and solid state-gas reactions up to 900 °C. The furnace guarantee, the absence of temperature gradients inside the sample. A thermocouple is placed inside to measure and control the sample temperature. The design permits homogeneous flushing with reaction gas and gas flow through the sample. The housing can be heated to prevent condensation of reaction gases. Table 3.2 shows the furnace specifications [8].

Table 1.4**:** Showing a list of the XRK 900 Chamber Specifications

Operating temperature:	**Ambient to 900 °C**
Temperature measurement:	NiCr / NiAl (type K) thermocouple
Max. housing temperature:	150 °C
Operating pressure:	approx. 1 mbar to 10 bar
Angle of incidence:	0 to +165° 2 Theta
Sample environment:	
Sample holder material:	Stainless steel or glass ceramic

Sample size:	
Diameter	max. 14 mm
Thickness	max. 1,5 mm
Materials:	Housing: Stainless steel, Inconel
Window foil:	Kapton (housing)
	Beryllium (temperature shielding)

Variable temperature measurement were collected and analyzed on a standard compound to calibrate the high temperature reaction chamber. National Institute of Standards Technology (NIST), silicon standard was used for the calibration. Silicon is one of the most frequently used internal standard materials in powder diffraction experiment for peak position calibration. The NIST Administration, U.S. Department of Commerce supplied the powder diffraction community with certified lattice parameters of silicon powder, Standard Reference Material [9]. The powder was subjected to successive diffraction data collection at different temperatures.

Firstly a scan at room temperature, 30^{o}C was measured. This was done to identify and confirm that the whole. Phase verification was done using the Bruker Eva search match and general data reduction software package. The powder was confirmed to contain one pure phase of silicon with the cubic diamond Fd-ms space group. Figure **1**.**18** shows the graphical representation of the results from Bruker's Diffract plus Eva version 3 software.

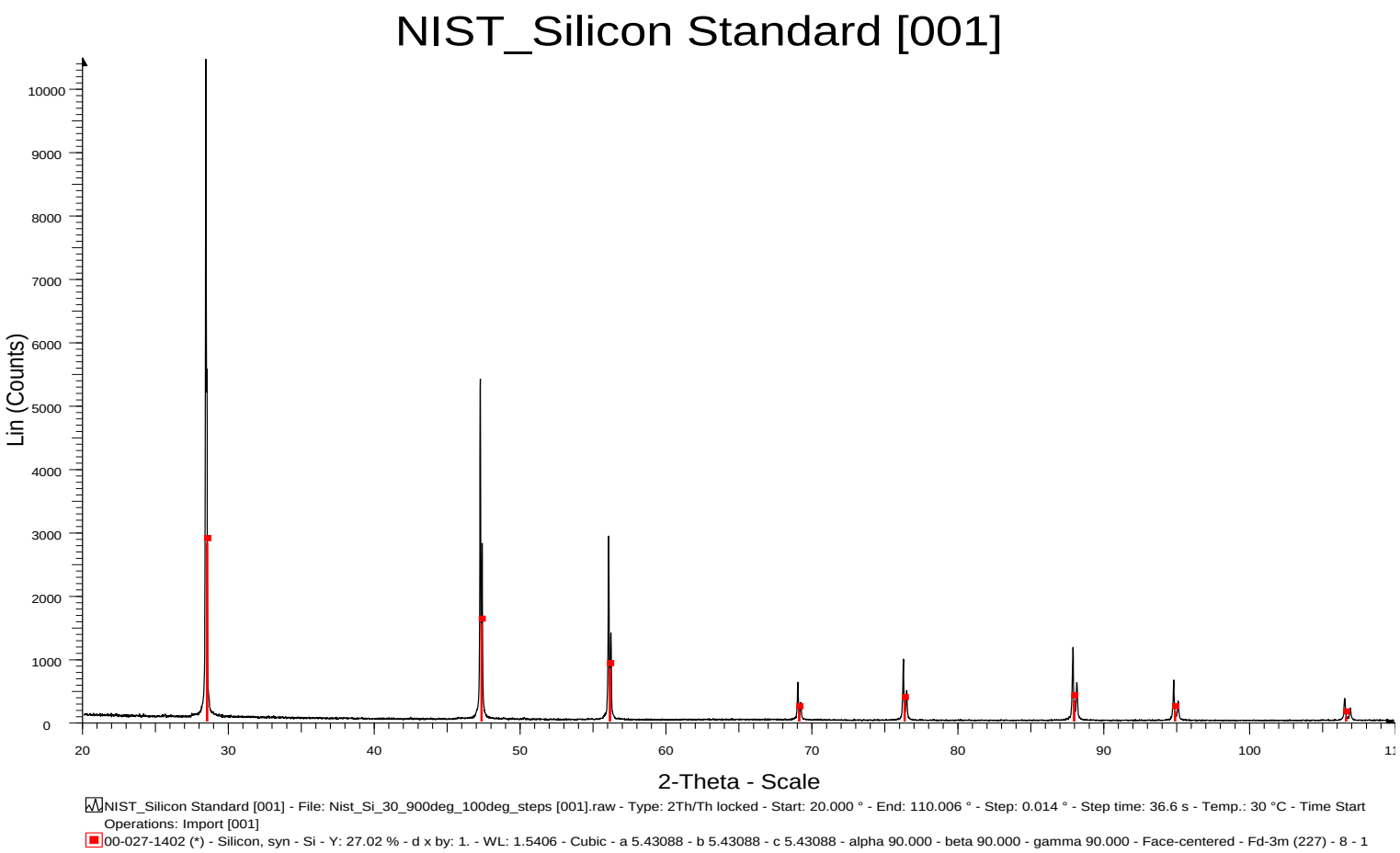


Figure 1.18: XRD powder pattern of the measured from the search match, phase identification Bruker Eva program showing all peaks of the measured powder corresponding to silicon

Variable temperature scans were measured from 50^{o}C to 900^{o}C at 50^{o}C increments. This was followed by a scan at room temperature after cooling the material *in-situ*. This scan was done to identify the phase present after the variable temperature measurements where done and to ensure that the chamber cooled down and did not dwell at 900^{o} C, which could damage the instrument. The resulting powder was identified to contain the same phase as the starting silicon standard powder. Figure **1**.**19** shows a summary of the scans after the high temperature study.

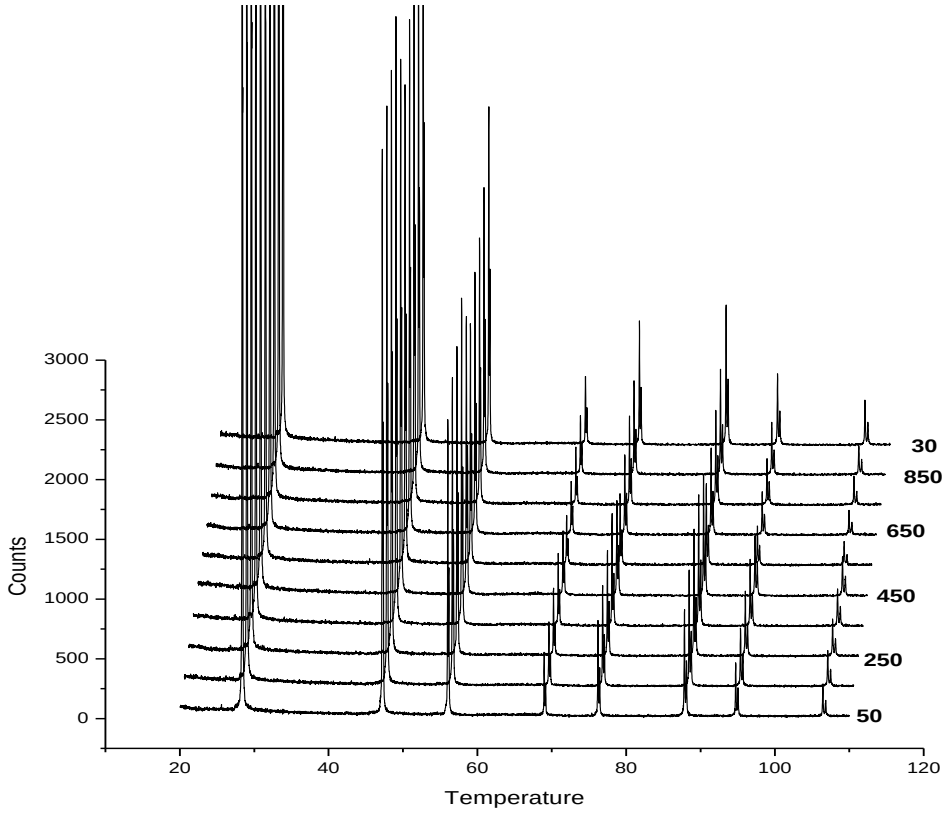


Figure 1.19: XRD patterns of silicon standard as a function of temperature

A Rietveld refinement using TOPAS version 3 was done sequentially on the different temperature scans. A refinement strategy as described in chapter 2 was used. The scale factor, Chebyshev background terms, unit cell coordinates and parameters, peak shape parameters and corrections, a sample height correction and Lorentzian polarization factor were refined and used systematically. Figure **1.20** graphically shows the refinement results, (measured in blue, fitted curve in red and the difference curve in grey) .

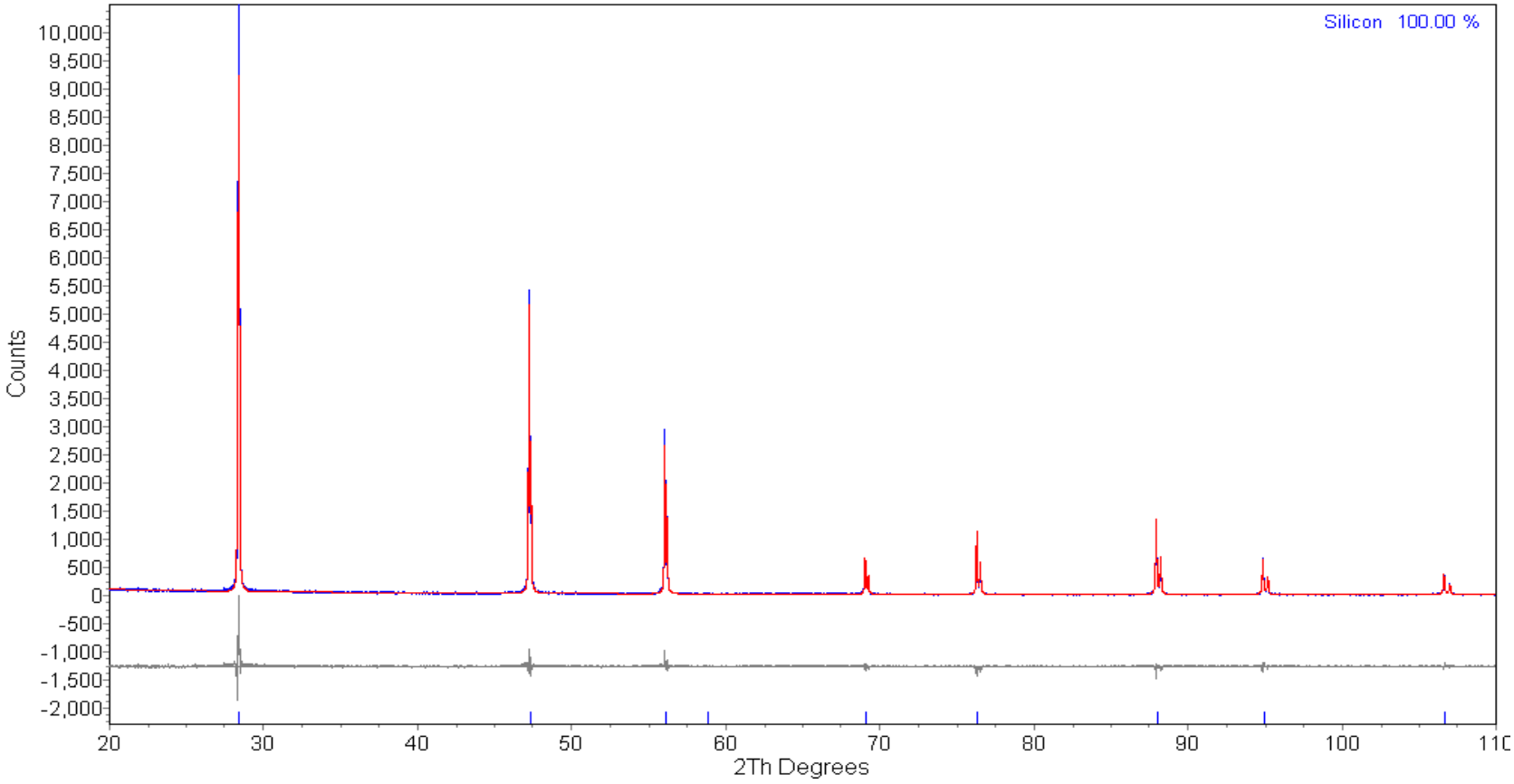


Figure 1.20: TOPAS output showing the results of the refinement of silicon standard, the measured pattern (blue), the calculated pattern (red) and the difference curve (grey)

No preferred orientation corrections were done during this refinement. A good fit was found as shown in the graphical representation. The global goodness of fit χ^2 was found to be 1.44 (χ^2 =1 for best fit). The global refinement fit results are listed in Table **1**.**5**. The individual goodness of fit for each refinement are listed in Table **1**.**6** and the TOPAS input file is shown in the appendix.

Table 1.5: List **of** Rietveld list squares refinement global goodness of fit data

	Value
Max. Iterations	1000
Chi2 convergence criterion	0.001
GOF	1.44
Rexp	11.96
Rwp	17.28
Rp	13.44

Table 1.6: List **of** Rietveld list squares refinement goodness of fit data for the individual patterns

Temperature	GOF	Rexp	Rwp	Rp
30	1.36	11.83	16.11	12.12
50	1.39	11.84	16.47	12.17
100	1.38	11.85	16.4	12.46
150	1.37	11.87	16.26	12.29
200	1.4	11.9	16.63	12.68
250	1.41	11.94	16.88	13
300	1.42	11.93	16.89	13.06
350	1.39	11.93	16.63	12.92
400	1.45	11.98	17.37	13.61
450	1.45	11.96	17.36	13.62
500	1.47	11.97	17.62	13.92
550	1.48	12.02	17.78	14.07
600	1.5	12.01	18.06	14.33
650	1.49	12.03	17.89	14.2
700	1.53	12.05	18.5	14.83
750	1.52	12.09	18.41	14.75
800	1.51	12.08	18.24	14.64
850	1.53	12.09	18.47	14.76
900	1.53	12.08	18.49	14.8
27	1.26	11.84	14.97	10.95

Unit cell parameters for all the scans were subsequently extracted and listed as a function of temperature (Table **1.7**). These were compared to the values determined by Okada et al [12], which were calculated using the formula given in equation 3.1. The group performed their studies between 150°C and 1500°C. The cell parameters between 150°C and 900°C are in good agreement with the literature values.

$$a_{calc} = a_0 + \frac{c_1}{e^{\theta_1 / T} - 1} \qquad 1\text{-}20$$

Table 1.7: **A** comparison of the unit cell parameters of the current calibration **with** literature values

Temperature	Phase Name	Space group	a (Å)	a (Å) (Okada)	Difference
30	Silicon	Fd-3mS	5.4318120	5.430741000	0.001071
50	Silicon	Fd-3mS	5.4321662		
100	Silicon	Fd-3mS	5.4331890		
150	Silicon	Fd-3mS	5.4342622	5.430834772	0.003427
200	Silicon	Fd-3mS	5.4353177	5.431101051	0.004217
250	Silicon	Fd-3mS	5.4363822	5.431560302	0.004822
300	Silicon	Fd-3mS	5.4375114	5.432179846	0.005332

350	Silicon	Fd-3mS	5.4387195	5.432921665	0.005798
400	Silicon	Fd-3mS	5.4398906	5.433754842	0.006136
450	Silicon	Fd-3mS	5.4409995	5.434656523	0.006343
500	Silicon	Fd-3mS	5.4424675	5.435610221	0.006857
550	Silicon	Fd-3mS	5.4437152	5.436604030	0.007111
600	Silicon	Fd-3mS	5.4451120	5.437629262	0.007483
650	Silicon	Fd-3mS	5.4465377	5.438679481	0.007858
700	Silicon	Fd-3mS	5.4478386	5.439749847	0.008089
750	Silicon	Fd-3mS	5.4494247	5.440836666	0.008588
800	Silicon	Fd-3mS	5.4507446	5.441937079	0.008808
850	Silicon	Fd-3mS	5.4523807	5.443048839	0.009332
900	Silicon	Fd-3mS	5.4535667	5.444170163	0.009397
27	Silicon	Fd-3mS	5.4325185		

Okada *et. al*. found that the temperature dependence of the co-efficient of linear thermal expansion of silicon to be given by

$$\sigma = 3.725(1 - e^{-5.88\times10^{-3}(t-120)} + 5.548t \times 10^{-4}) \times 10^{-6} \qquad 1\text{-}21$$

The calculated α values are plotted in Figure **1.20** (red). In the same plot, values of α coefficient of thermal expansion of the measured standard were calculated using the same formula and plotted (blue) and compared. Figure **1.20** also shows that there is negligible error in the thermal expansion results. The present results show the method used to obtain a calibration curve for the furnace is derived from the difference in unit cell parameters.

3.4 References:

.

1. Bruker Test Data Supplied to Le Bail Group d8 Advance Powder Diffractometer, http://sdpd.univ-lemans.fr/powdif/low_fwhm_and_rp.html

2. Bruker Diffract Plus EVA Search/Match Software, Bruker AXS Ltd., Congleton, UK

3. R. W. Cheary, A.A. Coelho, TOPAS. Version 3. Bruker AXS Inc., Karlsruhe, Germany., J. Appl. Cryst., 1992, **25**, 109

4. A..A. Coelho, TOPAS, General Profile and Structure Analysis Software for Powder Diffraction Data, Bruker AXS GmbH, Karlsruhe, Germany, 2003

5. J.P. Cline, R.D. Deslattes, J-L. Staudenmann, E.G. Kessler, L.T. Hudson, A.. Henins, R.W. Cheary, NIST Certificate, SRM 640c Line Position and Line Profile Standard for Powder Diffraction, NIST, Gaithersburg, MD, 2000

6. M. Wohlschlögel, U. Welzel, G. Maier, E. J. Mittemeijer, Calibration of a heating/cooling chamber for X-ray diffraction measurements of mechanical stress and crystallographic texture, *J. Appl. Cryst.,* **39**, 2006, 194-201

7. A. Löckner, HTK1200 High Temperature Oven Camera Instruction Handbook, Anton Paar GmbH, Graz, 1998

8. Anton Paar RXK 900 specification: www.anton-paar.com/ap/apinternet/html/default/fsin-5p3d5s.fr.0.jsp

9. NIST Specification Certificate for Silicon (SRM640c), http://patapsco.nist.gov/srmcatalog/common/view_cert.cfm?srm=640c

10. S. Altree-Williams, R. Clapp, Specific toxicity and crystallinity of α-quartz in respirable dust samples. AIHA J, 2002, **63**, 348

11. M. Taylor, Methods for the quantitative determination of asbestos and quartz in bulk samples using X-ray diffraction. Analyst, 1978, **103,** 1009

12. Y. Okada, Y. Tokumaru, Precise determination of lattice parameter and thermal expansion coefficient of silicon between 300 and 1500 K, J. Appl. Phys., 1984, **56**, 314-320

Chapter 4 : Synthesis, structural characterization and thermal expansion behavior of lead tungstate

4.1 Introduction

Lead tungstate, $PbWO_4$, adipts the general tungten scheelite structure with tungsten in tetrahedral IV coordinated atom occurs. It naturally occurs in one of two forms resulting from the hydrothermal formation, metasomatism and the oxidation of primary lead ores [1-8]. The term is Stolzite, with a tetragonal structure, and raspite with a monoclinic structure. Stolzite forms dipyramidal crystals often thick and tabular with striated faces. Its structure is more Scheelite with the lead in 8-coordination with the tungstate groups. It is similar to Wulfenite which has the same chemical structure except that the tungsten is replaced by molybdenum [9]. Lead tungstate crystals have the optical transparency of glass and a much higher density of 8.28 g/cm^3 compared to ~2.2 g/cm^3 for fused silica [10-11].

There has been increasing interest in it as seen by its widespread commercial use as a scintillator since its approval for use in the Compact Muon solenoid, (a schematic diagram is shown in Figure **1**.**21**) and also in Assembly Line Balance application

experiments to construct electron-magnatic calorimeters at the Large Hadron Collider (LHC) [12-18]

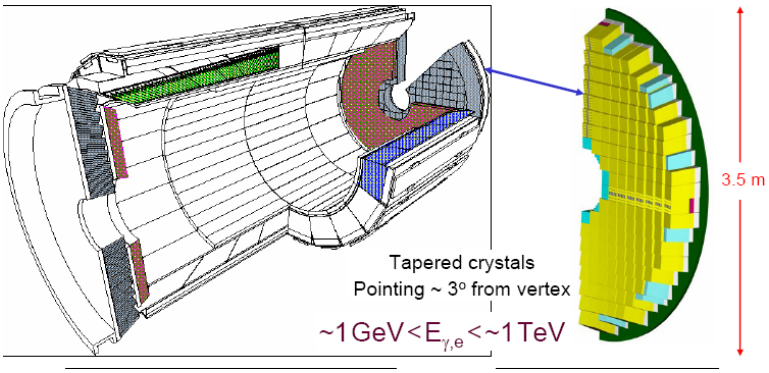


Figure 1.21: Schematic diagram of a lead tungstate scintillators [15]

A scintillator is a substance that absorbs high energy electromagnetic or charged particle radiation. In response to the absorbed energy, it liberates photons at a characteristic longer wavelength, releasing the previously absorbed energy. They convert the energy to light of a wavelength which can be detected by inexpensive or easy to handle detectors such as photomultiplier tubes (PMTs). Common scintillators used for radiation detection include inorganic crystals, organic plastics and liquids. Scintillators are defined by these number of emitted photons per unit absorbed energy, short fluorescence decay times, and optical transparency at wavelengths of their own specific emission energy [16].

Lead tungstate has the fastest light emission time, ~80% in 25 nano seconds compared to other more conventional materials, at peak emission is at 425 nm which is in the visible range, but it suffers from about 2.2 - 5 % / ^{o}C decay in dynamic equilibrium under radiation. This effect is illustrated in Figure 1.22. It has the l0west radiation length and Moliere radius values (0.9 and 2.19, respectively) among all known scintillators. Radiation damage appears at doses exceeding 105 Gy. Yet the light output of $PhWO_4$ is as low as about 1% of Csl(TI), so that the material can be used in high-energy physics experiments only [10, 19].

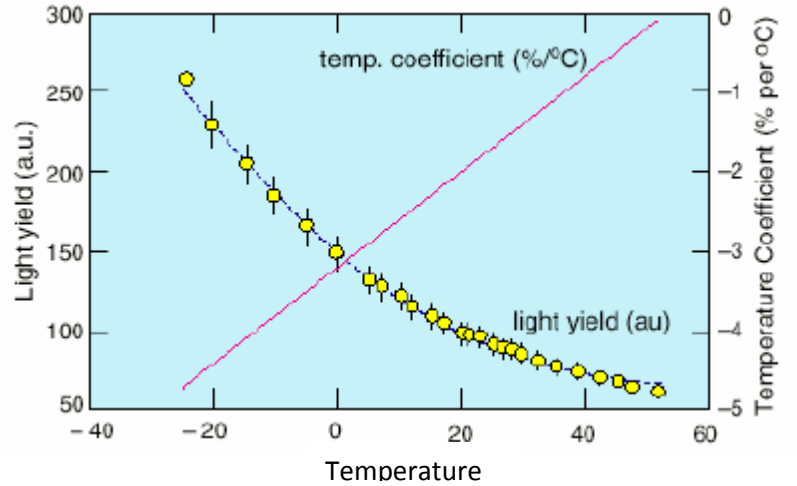


Figure 1.22: Plot showing coefficient of thermal expansion and light yield of lead tungstate with temperature [19]

The lower the decay time of a scintillator, that is, the shorter the duration of its fluorescence flashes, the less so-called "dead time" the detector will have and the more ionizing events per unit of time it will be able to detect [10].

In the present study the powdered Stolzite form of lead tungstate was synthesized using sol-gel and powder mixing techniques. Room temperature and variable temperature powder X-ray diffraction will served as the primary means of characterization. The Rietveld refinement of the powder X-ray diffraction data were conducted using an appropriate structure model obtained from the (ICSD release 1 2008).

4.2 Synthesis

The metal alkoxide sol-gel method, described in chapter 2, was used for the preparation of the tungstate. WCl_6 was dissolved in an alcohol to form a blue intermediate ($WCl_{6-x}(OC_2H_5)_2$) and hydrochloric acid as shown in equation 1-22. The resulting mixture was then refluxed in alcohol at a temperature of 50^{o}C for 24 hours, after which a transparent alkoxide $WCl_{6-x}(OC_2H_5)_2$ formed as shown in equation 1-23 , The resulting transparent color of the product indicated a full conversion of the intermediate to the alkoxide.

$$WCl_6 + XC_2H_5OH \rightarrow WCl_{6-x}(OC_2H_5)_2 \text{ (Blue)} + HCl \qquad 1\text{-}22$$

$$WCl_{6-x}(OC_2H_5)_2 \text{ Blue} + (6-x)C_2H_5OH \rightarrow W(OC_2H_5)_6 \text{ (transparent)} + (6-x)HCl \quad 1\text{-}23$$

The tungsten based metal alkoxide was then added to a solution volume, most of lead nitrate in ethanol. A few drops of water were added to the resulting solution to form a gel. The gel was then dried for 48 hours at ambient temperature to form a xerogel product as per equation 1-24. The xerogel product was calcined at 500^{o}C for 4 hours to form the crystalline lead tungstate. The whole process is outlined as shown in the flow chart figure **1-25**.

$W(OC_2H_5)_6 + Pb(NO_3)_2.6H_2O \rightarrow PbWO_4$ (amorphous) + $C_2H_5OH + NO_3^-$ (*aq*) 1-24

$$PbWO4\,(\text{amorphous}) \xrightarrow{\Delta} PbWO4\,(\text{crystalline}) \qquad \textbf{1-25}$$

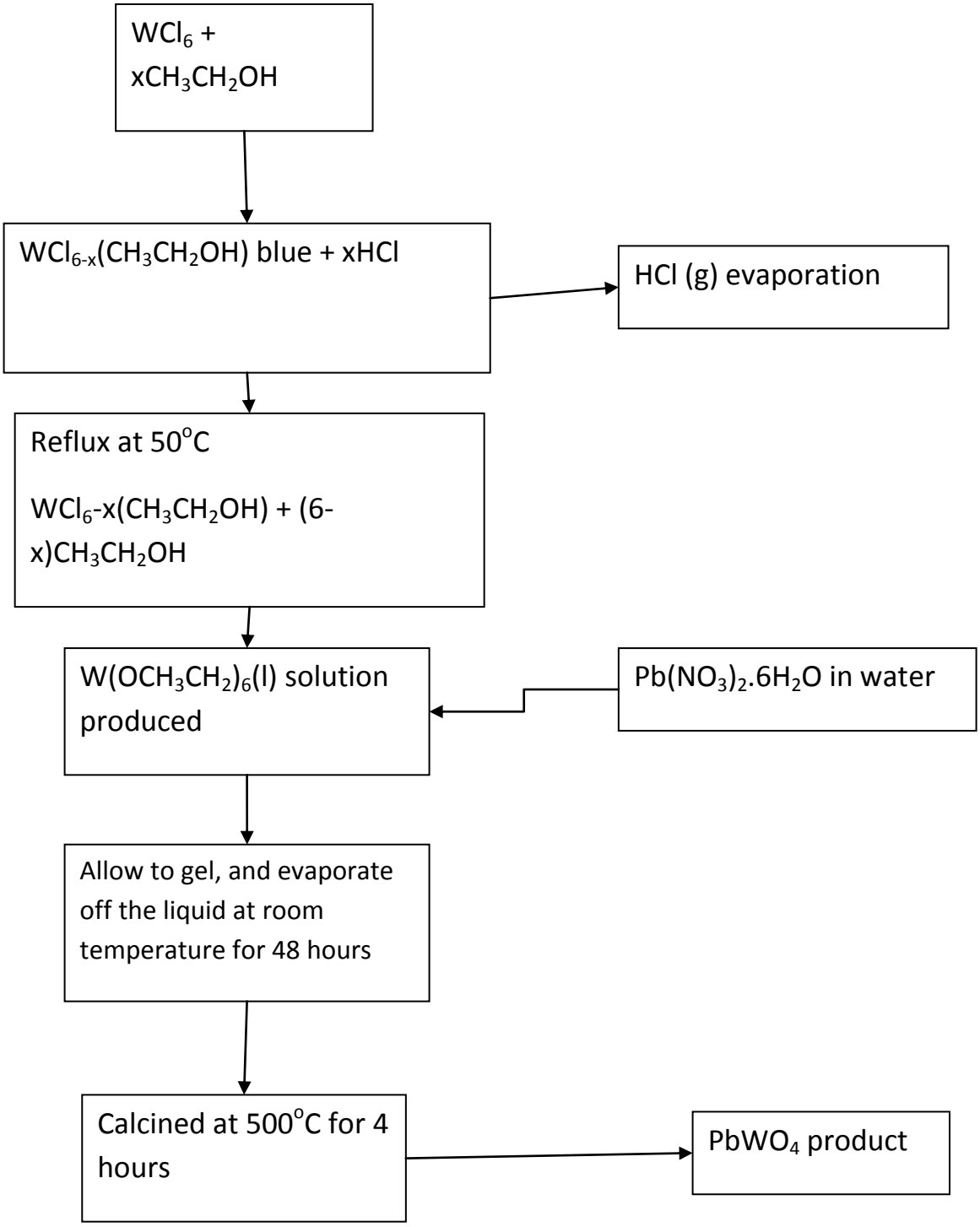


Figure 1.23: Shows a flow diagram of the Sol-Gel process described above

4.3 Phase identification of lead tungstate

The starting structural model used in a Rietveld refinement program is important and needs to be as similar in structure to the actual material as possible. This means that the material produced needs to be identified first. From its unit cell parameters and atomic coordinate that are close to the true ones are needed for ease of refinement. Using a search match program linked to the Powder diffraction database, fingerprinting of the measured diffractogram was conducted, to identify the phases present in the oxide formed. Bruker EVA version 3 phase identification software was used and results are shown on Figure 1.24.

Clearly only one phase is present in the graph after calcination since all the peaks corresponded to one phase. The phase was confirmed to be the mineral Stolzite, $PbWO_4$, (Figure 1.24; Table 1.8). Peaks associated with Pbo2 and WO3 phases, stable oxides of lead and tungsten were not present. These results substantiate that this synthetic methodology produces exclusively the stolzite form of lead tungstate.

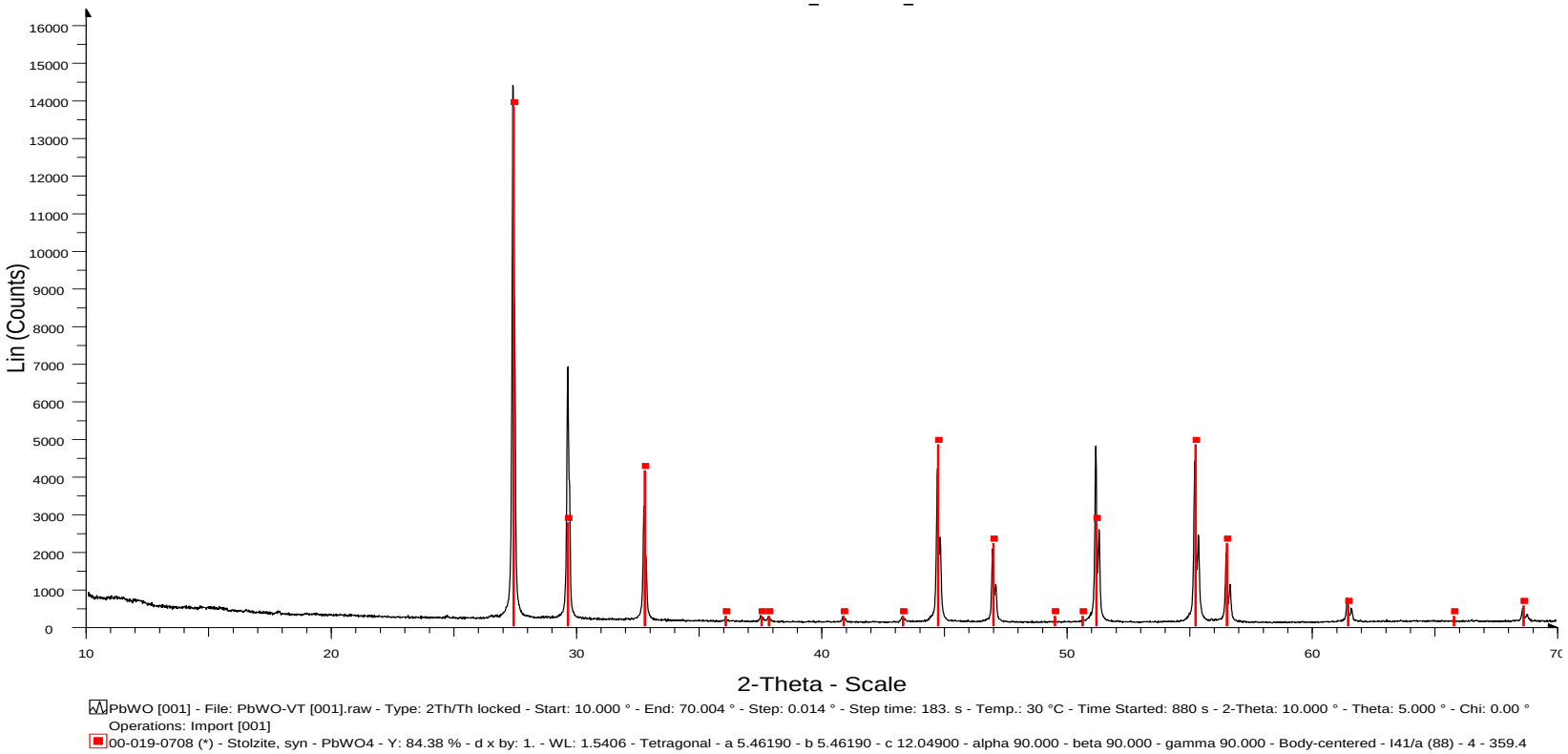


Figure 1.24 XRD powder pattern of the measured from the search match, phase identification Bruker; Eva program showing all peaks of the measured powder corresponding to lead Tungstate, stolzite.

Table 1.8 shows search match results of experimental powder diffraction pattern

No.	Ref. Code	Compound Name	Chemical Formula	Score	Scale
1	00-008-0476	Stolzite	Pb W O4	70	0.714

The irreversible conversion of the monoclinic form of lead tungstate, raspite to Stolzite happens at 400^{o}C [20], *in-situ* product was calcined at 600^{o}C, no raspite was observed. Furthermore, the absence of any nitrate and chloride based compounds, which when present in the starting material; ($Pb(NO_3)_2$, WCl_6 and CH_3CH_2OH), the reactant were removed by the washing procedure or oxidized during the heat treatment

From the ICSD database, Stolzite type structures have a tetragonal system that belongs to the I41/a space group. Table **1.9** summarizes the unit cell parameters for this phase which would be the starting point for refinement.

Table 1.9 ***Cell parameters of our Stolzite type structure [ref]***

Space group :	I41/a

Unit cell parameters	
a (Å):	5.4616
b (Å):	5.4616
c (Å):	12.046
Alpha (°):	90
Beta (°):	90
Gamma (°):	90

4.4 Structural refinement from Rietveld refinement

Rietveld refinement structure modeling was performed using the TOPAS version 3 [108] program with standardized instrumental parameters derived from calibration using LaB_6 as a standard. The resulting powder pattern is plotted in **Figure 1.25**, and shows a good fit, χ^2 of 2.61 calculated as the ration of R_{wp}, weighted to emphasize intense peaks over background, and R_{exp}. The best values of R_i (i = *exp* or *wp*) were estimated for a data set and are listed in Table **1.10**

$$X^2 = \frac{R_{wp}}{R_{\exp}} \qquad 1\text{-}26$$

Table 1.10: *Refinement statistics*

R-Values	
R-exp	7.92
R-wp	12.79
R-p	15.56
χ^2	2.61

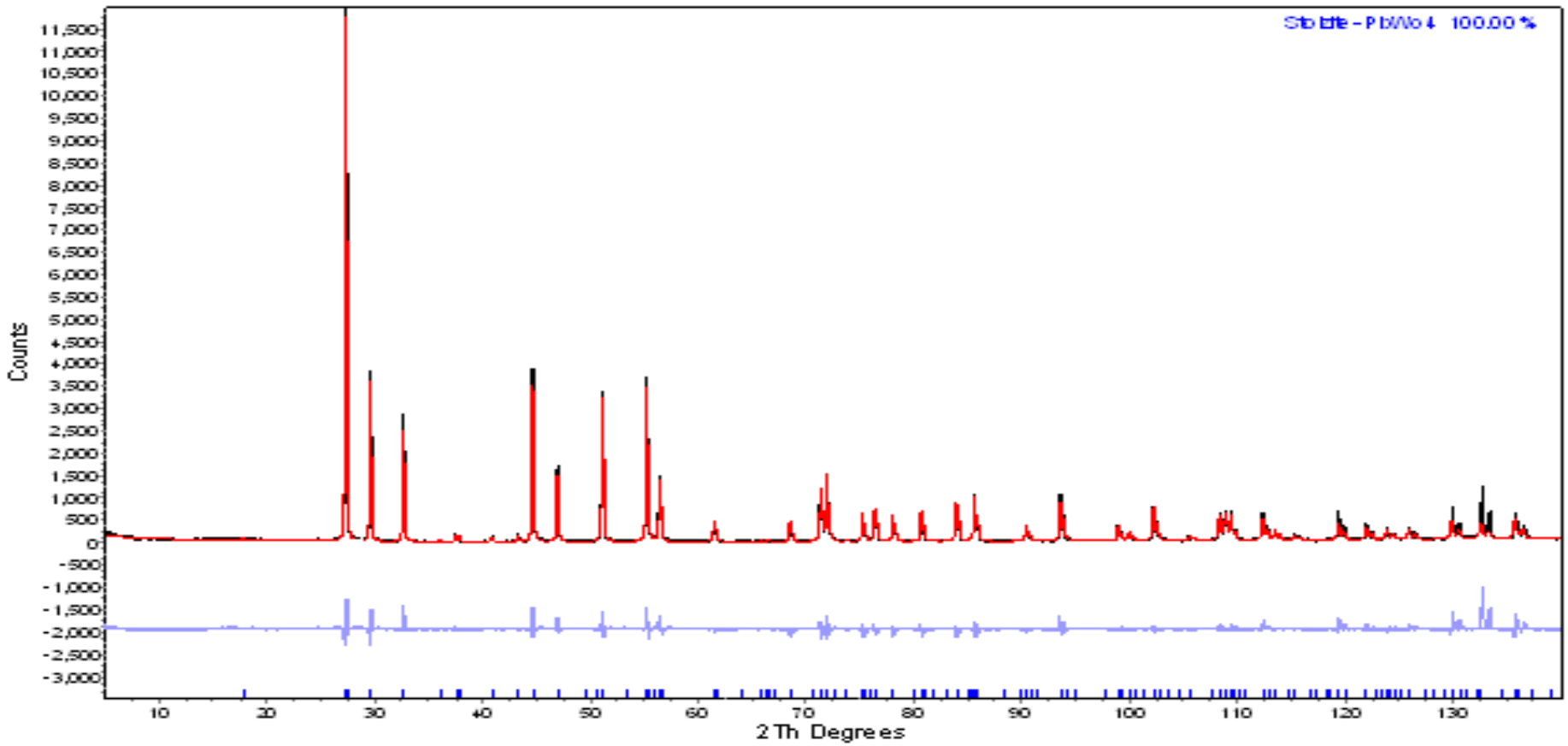


Figure 1.25*:* Rietveld refinement results for PbWO4: The measured pattern (black), fitted pattern (red) and difference curve below (blue)

Figure 1.25 shows a curve for the difference between the fitted or modeled diffraction pattern and the measured pattern. The ideal difference is a straight line with a null value showing insignificant differences between the calculated and measured peak shape and intensities. The above difference curve supports the good fit suggested by χ^2 calculations.

Instrumental factors were refined in order of importance. The most important variables were, the *scale factor, background, lattice parameter, peak width, atomic position, preferred orientation, isotropic temperature factor B, Caglioti and profile parameters. More* reactions were added later until an adequate solution was realized. This was done since Rietveld methods fit a multivariable structure-background-profile model to experimental data so there is potential for "false" minima, diverging solutions, *etc*. A scale factor of 5.72×10^{-5} was determined and a second order polynomial was used for the refinement of the background function, with the coefficients as tabulated in Table 1.11

Table 1.11 Refined linear background coefficients

Background Chebychev polynomial, coefficient	
0	53.5

1	28.4
2	24.6

Lead tungstate falls into the tetragonal system which means all angles are 90^{o} and unit cell dimension *a* = *b*. Therefore the lattice parameters refined were only *a* and *c,* with *a* of 5.47078 Å and *c* of 12.06732 Å. These values are within the stolzite space group reported in the literature [9] and outlined in Table **1**.**12**.

Table 1.12: Refined structural parameters

Phase name	**Stolzite $PbWo_4$**
R-Bragg	6.979
Space group	I41/aZ
Lattice parameters	
a (Å)	5.47078
c (Å)	12.06732
Scale	0.00005724

Cell Mass	1820.200
Cell Volume ($Å^3$)	361.168
Wt% - Rietveld	100.000
Crystal Linear Absorption Coefficient. (1/cm)	1446.615
Crystal Density (g/cm^3)	8.36872

There are two most widely used profile shape functions, the pseudo-Voigt and the Pearson VII. Using the standard *Mathematica* package [22] "Statistics Non linear Fit" and high resolution synchrotron data, the physical meaning of the pseudo-Voigt may be questioned since its variance is not defined even though its ease of computation is better than the Pearson VII function [23]. Therefore in the refinement a Pearson VII peak shape function was chosen. The profile breadth which is expressed as the profile full width at half maximum (FWHM), H_k was varied according to 2ϑ governed by the Caglioti parameters, *W*, *V* and *U* according to equation 1-27.

$$H_k\ (FWHM) = U\tan^2\theta_k + V\tan\theta + W \qquad \text{1-27}$$

with the parameters *U*, *V* and *W* refined to 0, 0.22 and 0 respectively. The shape factor *m*, which governs the rate at which the tail falls was refined using equation

$$Exponent_m = 0.6 + ma + \frac{mb}{Cos\theta} + \frac{mc}{Tan\theta} \qquad \text{1-28}$$

, with the corresponding *a, b* and *c* coefficients listed in Table 1.13

$$Exponent_m = 0.6 + ma + \frac{mb}{Cos\theta} + \frac{mc}{Tan\theta} \qquad \text{1-28}$$

Table 1.13: **A** listing **of** the refined coefficient of the shape factor from a Pearson VII function

m*a*	**20**
m*b*	0
m*c*	5

Instrumental parameters listed in Table 1.10 containing refinement statistics were used in the refinement according to the calibration refinement performed using the LaB_6 standard, discussed in chapter 3. Error correction parameters refined incuded

the sample zero error which was refined to -0.02 and the Lorentzian-Polarizing absorption (LP) factor.

The preferred orientation caused by plate-like or rod-like crystallites' tendency to experience preferential alignment along the axis of a cylindrical sample holder, also required correction. It manifested itself by variation of the intensities of particular (*hkl*) reflections, causing errors in the refinement.

Table 1.14: Refinement statistics

Instrument Factor	
Primary radius (mm)	250
Secondary radius (mm)	250
Receiving slit width (mm)	0.2
Divergence angle (°)	0.013
Full Axial Convolution	
Filament Length (mm)	12

Sample Length (mm)	15
Receiving Slit Length (mm)	12
Primary Sollers (°)	4
Secondary Sollers (°)	4

.

In this refinement, a spherical harmonics model was used for the preferred orientation corrections.

Table **1**.**15** lists the refinement results. A spherical harmonics model of the 8th order was used to fit the measured pattern.

Table 1.15: Showing preferred orientation refinement results using 8th order spherical harmonics

Preferred Orientation (Dir 1 : 024)	**1.23**

Preferred Orientation Spherical Harmonics	
Order	8
y00	1
y20	0.06
y40	0.174
y44m	0.211
y44p	-0.02
y60	0.0098
y64m	-0.71
y64p	-0.003
y80	-0.152
y84m	-0.43
y84p	-0.0972
y88m	1.19
y88p	-0.0251

Table **1.16** lists the fractional co-ordinates and site occupancies, refined with 4 Pb and W atoms to 16 oxygen atoms in a unit cell. Both lead and tungsten occupy special positions so their co-ordinates were not refined. Only the oxygen co-ordinates were refined.

Table 1.16: List refined atomic coordinates

Site	Np	X	y	x	Atom	Site Occupancy	B eq
Pb	4	0.500	0.750	0.125	Pb^{+2}	1	-0.146
W	4	0.000	0.2500	0.125	W^{+6}	1	0.410
O	16	0.231	0.578	0.0414	O^{-2}	1	0.28

From the refinement results above a *cif* file (Crystallographic information) was prepared and a TOPAS input file was not (Appendix 3). The crystal structure diagram was generated using Diamond [24]. Figure **1.26** shows the unit cell and the packing pattern of the $PbWO_4$ crystals. The pattern shows alternating rows of WO_4 at PbO_4.

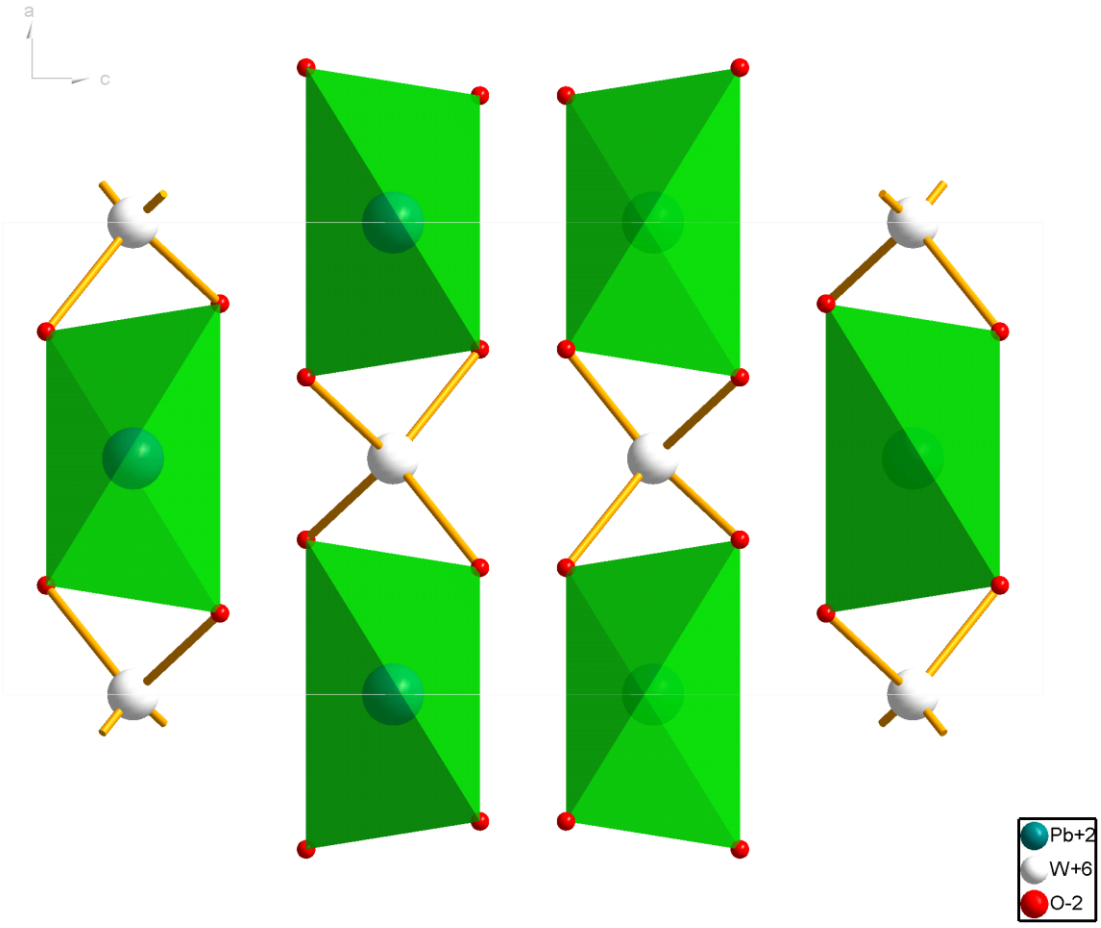


Figure 1.26: Diamond diagram showing packing pattern extracted from the refinement of the synthesized lead tungstate

The tungsten and the lead each forming a tetrahedral geometry surrounded by oxygen atom as is shown in

Figure 1.27 and Figure **1.28**. These geometries are similar to the lead tungstate formed by hydrothermal synthesis reported in the literature [9]. This shows

that the sol-gel preparation method forms good quality structured product that could be used in the scintillator industry.

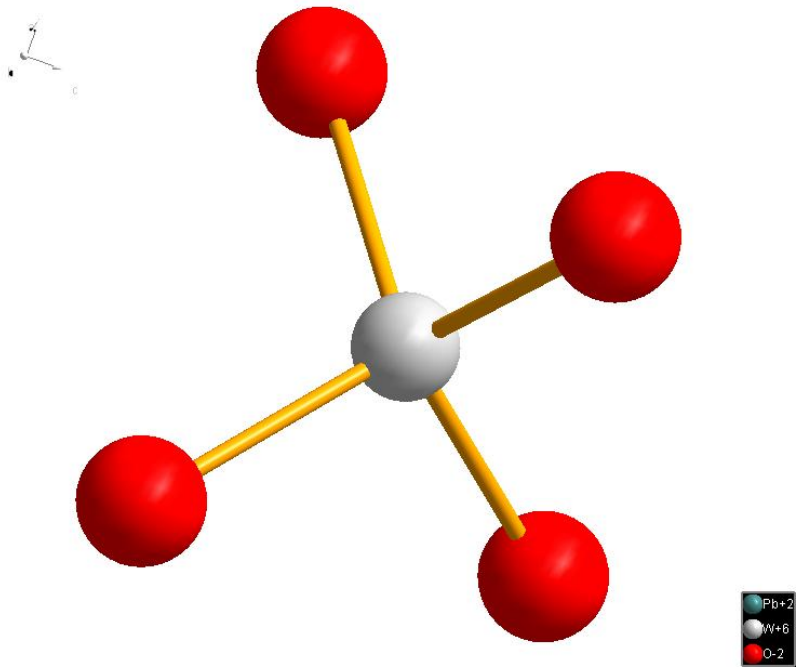


Figure 1.27: Diagram showing the tetrahedral bonding of tungsten with oxygen

All the tetrahedral bond lengths between the tungsten and oxygen were measured to be 1.872 Å, with angle of 106.88 Å between oxygen. Four of the Pb^{+2} and O^{-2} had

bond lengths of 2.530 Å and the remaining bonds were 2.661 Å in length. All the angles were measured to be 76.66^{o}.

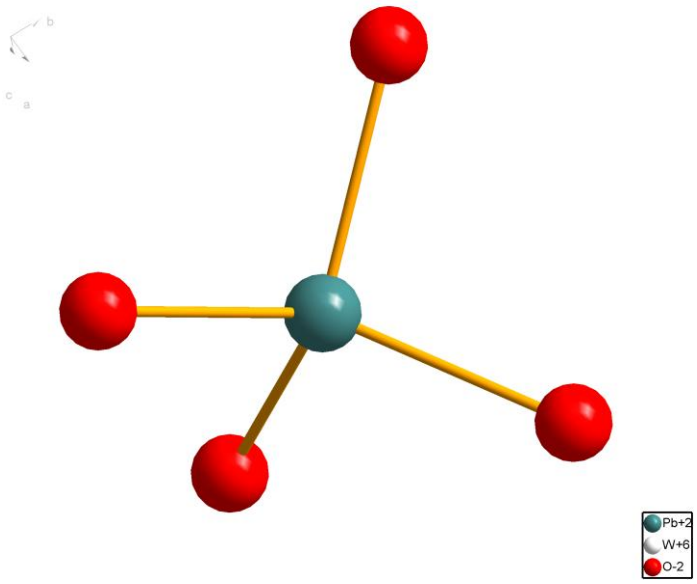


Figure 1.28: Diagram showing the tetrahedral bonding of Lead with oxygen

4.5 Determining the thermal expansion coefficient of lead tungstate using variable temperature XRD and Rietveld refinement

Diffraction patterns of $PbWO_4$ at elevated temperature were measured using the Anton Paar XRK900 reaction chamber. These measurements were performed at 50^{o}C intervals, starting from 30^{o}C (room temperature) up to 850^{o}C.

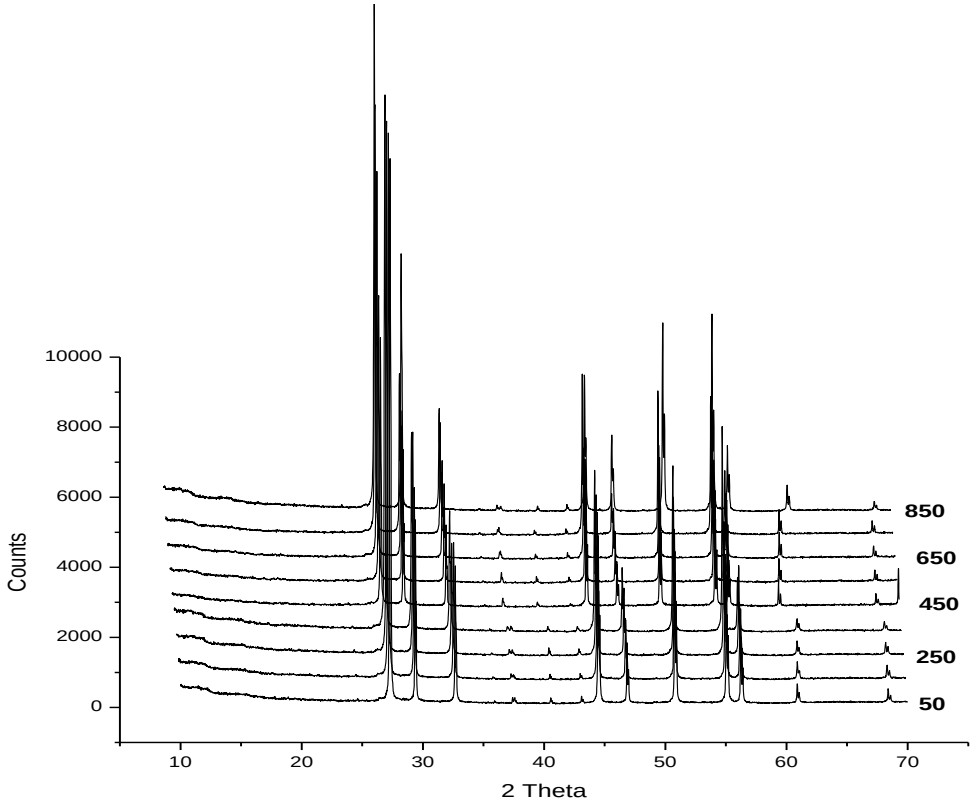


Figure 1.29: Selected XRD patterns of $PbWO_4$ as a function of temperature

Rietveld refinement using TOPAS was performed as described previously for each temperature. The goodness of fit for all the different temperature measured patterns ranged between χ^2 of 1.75 – 2.10 listed in Table 1.17.

Table 1.17: List Rietveld list squares refinement goodness of fit data

Temperature ^oC	**χ^2**	**Rexp**	**Rwp**
30	1.75	5.61	7.52
50	1.83	5.56	10.16
100	1.88	5.56	10.6
150	1.83	5.68	10.4
200	1.89	5.7	10.78
250	1.98	5.62	11.11
300	1.94	5.72	11.09
350	1.93	5.73	11.09
400	1.94	5.77	11.18
450	1.97	5.79	11.42
500	2.00	5.84	11.69
550	1.92	5.97	11.47
600	1.90	6.08	11.59
650	1.94	6.09	11.79

700	2.10	6.06	12.74
750	1.95	6.2	12.09
800	1.98	6.23	12.37
850	2.01	6.22	12.5
30	1.77	5.76	10.19

Unit cell parameters were obtained from the resulting refined patterns. Across the temperature range studied, no phase transformation occurred. Figure 1.30 and Figure 1.31 plots the unit cell edges *a* and c. Both parameters increase gradually with increasing temperature, having a change in dimension, Δl, of 0.05 and 0.35 respectively.

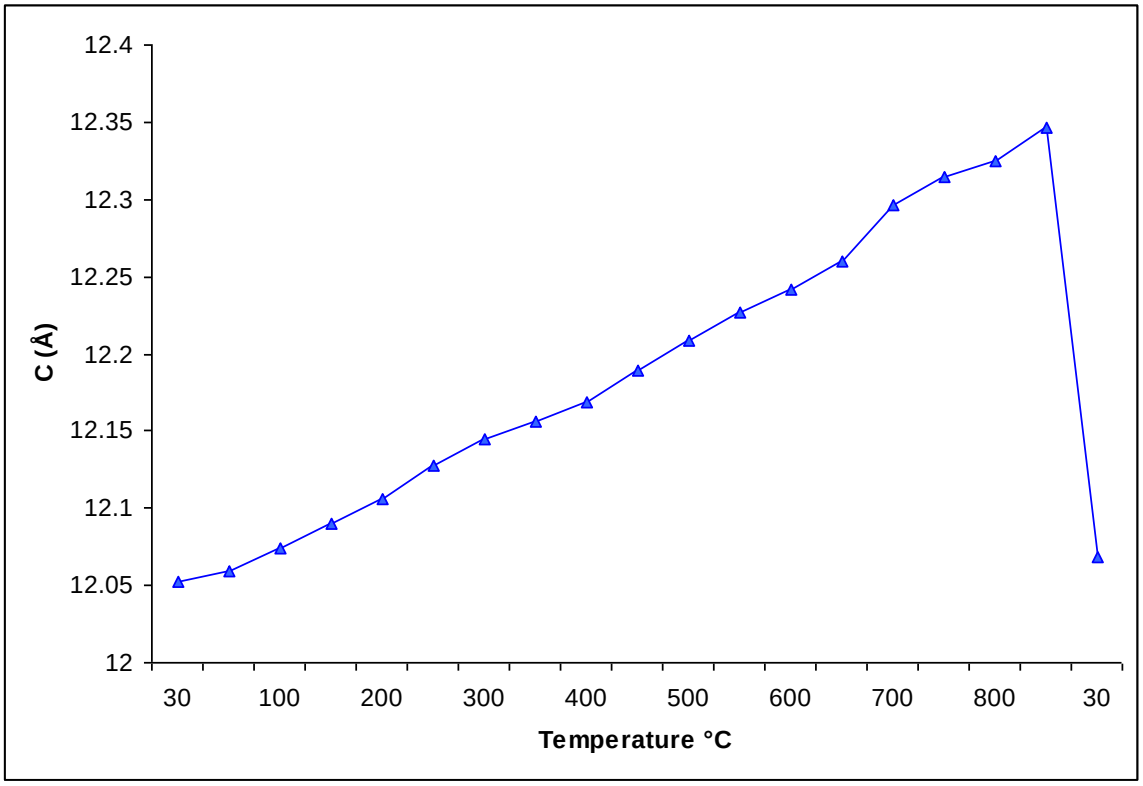


Figure 1.30: Plot shows the increase in the unit cell parameter c with temperature for the refined variable temperature measurement of lead tungstate

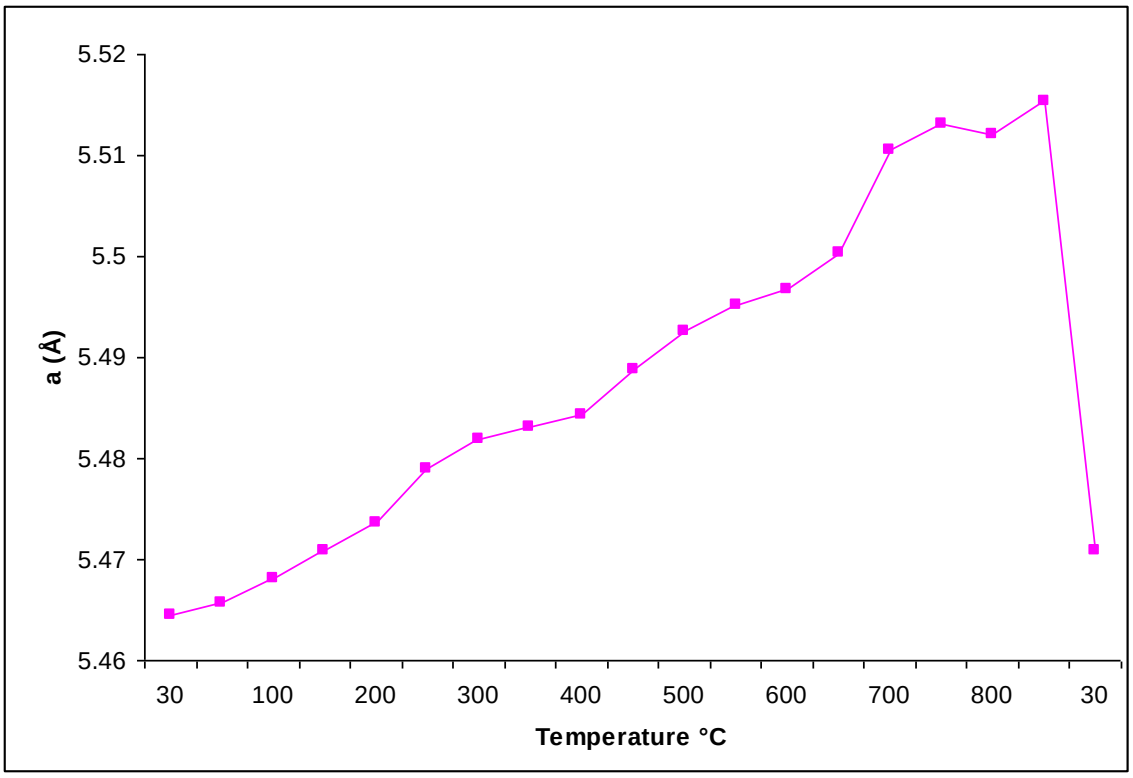


Figure 1.31 Plot shows the increase in the unit cell parameter a with temperature for the refined variable temperature measurement of lead tungstate

Using equation 4-8 and plotted (Figure 1.32)

$$\sigma_m = \frac{1}{L_0}\left(\frac{\Delta L}{\Delta T}\right)$$ 1-29the linear thermal

expansion co-efficient using to both unit cell parameters, over the temperature range was calculated and plotted (Figure 1.32)

$$\sigma_m = \frac{1}{L_0}\left(\frac{\Delta L}{\Delta T}\right) \qquad 1\text{-}29$$

Low thermal expansion material are defined by their co-efficient of thermal expansion at values between $0 > \sigma_m < 2 \times 10^{-6}\ K^{-1}$. In the *a* direction the thermal expansion coefficient ranges between 0 and $2 \times 10^{-5}\ K^{-1}$, with the exception at 800°C where the expansion is negative. This can be due an error in the refinement. In the c direction the thermal expansion ranges from 2 and 6×10^{-5}. These results introduce $PbWO_4$ as a material that exhibits low positive thermal expansion material.

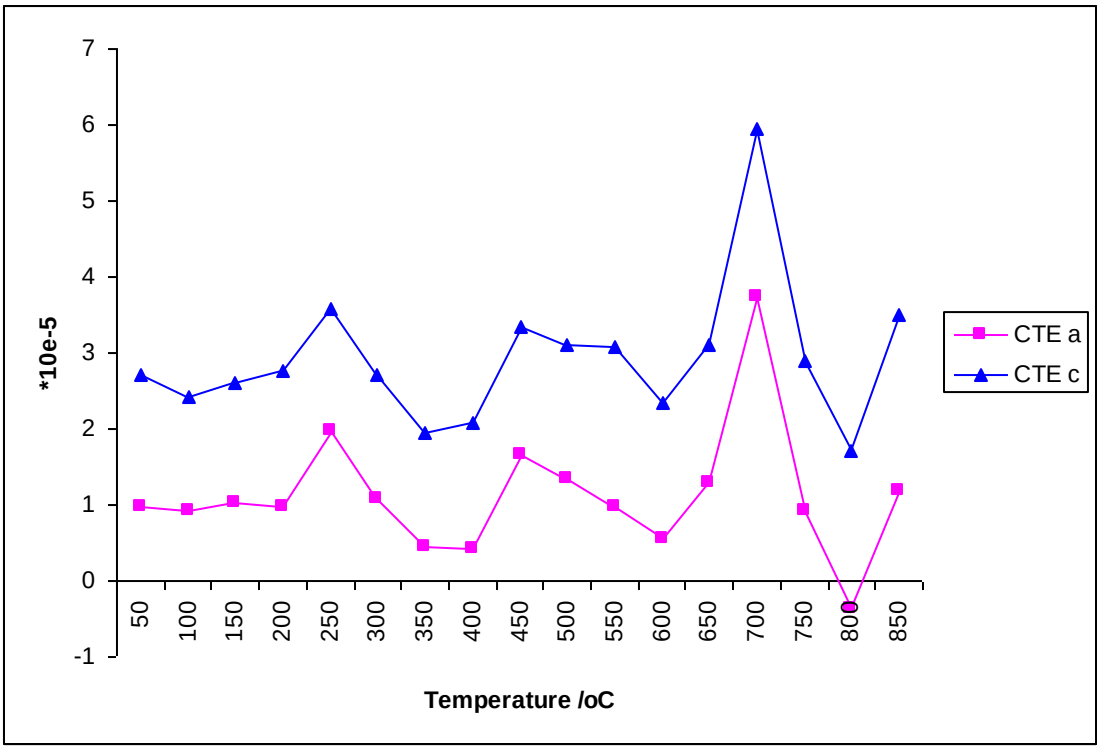


Figure 1.32: Plot the co-efficient of linear thermal expansion over a temperature range of $PbWO_4$ calculated from refined unit cell parameters

4.6 Conclusion

Lead tungstate was synthesized using a sol-gol preparation method and the structure determined using powder XRD was found to agree with the Scheelite structure reported in the literature that was synthesized by other methods. Rietveid refinement using variable temperature powder XRD patterns was used to evaluate the thermal behaviour

of the material. These studies revealed a thermal expansion co-efficient of 0-2 x10-5k^{-1} in the temperature range 30-90°c.

4.7 References:

1. M. N. Chureva, Zapiski Vsesoyuz. Mineral. Obshchestva, Mem. Soc. Russe Mineral, 1948, **77**, 103
2. E. E. Foord, N. M. Conklin, Stolzite from Tsumeb, Mineral. Rec., 1982, **13,** 149
3. J. T. Kloprogge, M. L. Weier, L.V. Duong, R. L. Frost, Microwave assisted synthesis and characterisation of divalent metal tungstate nanocrystalline minerals: ferberite, hübnerite, sanmartinite, scheelite and stolzite, Materials Chemistry and Physics, 2004, **88**(2-3), 438
4. S. P. Kilias And J. Konnerup-Madsen, Fluid inclusion and stable isotope evidence for the genesis of quartz-scheelite veins, Metaggitsi area, central Chalkidiki Peninsula, N. Greece, Mineralium Deposita, 1997, **32,** 581
5. Kosakevitch, Morocco Miner. Ind. Mines, Direct. Mines Geol, Notes Mem. Serv. Geol., 1970, **225,** 179
6. J. S. Stevenson, Univ. Toronto Studies, Geol. Ser., 1941, **46**, 137.
7. K. Walenta, The secondary minerals of the barite vein of the Clara mine near Oberwolfach, central Black Forest Aufschluss, 1975, **26,** 369
8. L. K. Yakhontova, Z. Vsesoyuz. Mineralog. Obshchestva, Mem. Soc. Russe Mineral., 1954, **83,** 117
9. C. Klein, *The 22nd Edition For The Manual Of Mineral Science* (After James D. Dana), John Wiley & Sons, Inc., New York, 2002.
10. R.Y. Zhu, D.A. Ma, H.B. Newman, C.L. Woody, J.A. Kierstead, S.P. Stoll, P.W. Levy, A Study On The Properties On Lead Tungstate Crystals, Nucl. Instr. And Meth. A, 1996, 1
11. L. Gigliola, M. Gianluca, M. Ledi, M.M. Cristina, P. Alfonso, S. Ulderico, Density Of Multicomponent Silica-Based Potential Bioglasses: Quantitative Structure-Property Relationship (Qspr) Analysis, J. European Ceramic Society, 2007, **27** (2-3), 14171

12. CMS Collaboration Technical Proposal, Compact Muon Solenoid Technical Proposal, Cern/Lhcc, 1994, 94-38,

13. CMS collaboration, Compact Muon Solenoid Letter Of Intent, Cern/Lhcc , 1992, 92-3

14. M. Nikl, K. Nitsch, J. Hybler, J. Chval And P. Reiche, Radiation induced formation of color centers in $PbWO_4$ single crystals, Phys. Status Solidi., 1996, **K7**, 196

15. N. Annekov, M. Korzhik And P. Lecoq, Ieee Nuclear Science Symposium Conference Record, Toronto, 1998 (1999), Nov. **8-14**, 46.

16. N. A. Bajanov, Y. S. Blinnikov, Y. I. Gusev, T. Y. Klechneva, Kovalev, L. A. Levtchenko, F. V. Moroz, D. M. Seliverstov, V. A. Kachanov, N. A. Golubev, V. A. Frolov, V. N. Lukyanov, G. A. Mamaeva And D. M. Prilutskaya, Nuclear Instruments & Methods In Physics Research, Section A: Accelerators, Spectrometers, Detectors, An Associated Equipment, 2000, **442,** 146

17. M. Diemoz, Calorimetry In High Energy Physics, Proceedings Of The International Conference, 8th, Lisbon, Portugal, 1999 (2000), June **13-19**, 250

18. M Stefan, S. Vnistor, E Goovaerts, M. Nikl P. Bohancek, Temperature Dependence Of The Electron Paramagnetic Resonance Spectra Of Mn2+ Impurity Ions In Pbwo4 Single Crystals, J. Phys.: Condens. Matter, 2005, **17,** 719

19. M. Korzhik, P. Lecoq, Search of new scintillation materials for. nuclear medicine application, IEEE Transactions On Nuclear Science, 2001, **48**, 628

20. R. Shaw, G.F. Claringbull, Mineralogical Society (London), Am. Mineral., 1955, **40,** 933

21. R. W. Cheary, A.A. Coelho, TOPAS. Version 3. Bruker AXS Inc., Karlsruhe, Germany., J. Appl. Cryst., 1992, **25**, 109

22. http://www.wolfram.com

23. B. Courant ,B Bourniquel, M Francois, M Bessiere Observations On Two Commonly Used Profile Shape Functions, Materials Science Forum, 2000, **347-349**, 23

24. http://www.crystalimpact.Com/Diamond/Sales.Htm

Chapter 5 : Quantitative Rietveld phase analysis: niobium tungstate

5.1 Introduction

Quantitative Rietveld Phase Analysis is in principle a standardless multiphase analysis method and a powerful method for determining the quantities of crystalline and total amorphous content in multiphase mixtures.

Rietveld refinement is calibrated using a NIST silicon standard, described in chapter 3. This is the main advantage of using Rietveld refinement methods over other methods. With Rietveld the calibration constants are computed from reliable structural data, rather than by laborious experiments,. All peaks in the pattern are explicitly included for calculation, unlike using relative intensities that only takes into account the contribution of the highest peak [1-3]. The effects of preferred orientation and extinction are reduced. Crystal structural and peak profile parameters, particle statistics, microabsorption etc. are refined as part of the same analysis [4-7]

5.2 Synthesis

Classical solid state synthetic techniques, via the grinding and firing of stoichiometric mixtures of the constituent oxides was described in chapter 2 and explored for the synthesis of niobium tungstate. This was done by mixing the oxides together and heating at an appropriate temperature that is depending on the physical properties of the oxide material being studied.

To make niobium tungstate; tungsten oxide, WO_3 and niobium pentoxide, Nb_2O_5, were used. WO_3 has a melting point of 1473^oC and Nb_2O_5 melts at 1380^oC. Having a melt mediated reaction would be ideal. Unfortunately the furnace does not heat high enough and that is the real reason.

.

WO_3 and Nb_2O_5 were ground and mixed together in a pestle and mortar. The mixed powders were calcined for 48 h at 1000 ^oC. Green pellets were formed by pouring 100 g of powder into a 28.6-mm-diameter die and uniaxially pressing them at 10 bar for 30 s. The pellets were fired at 1300 ^oC for 4 h with being ramped to this temperature at a rate of, at 5 ^oC /min ramp. The samples were allowed to cool in the furnace at 5 ^oC/ min. The products were formed according the overall reaction

outline given in equation $WO_3 + Nb_2O_5 \xrightarrow{\Delta,air} Nb_2WO_8 + Nb_8W_9O_{47}$ 5-1.

$$WO_3 + Nb_2O_5 \xrightarrow{\Delta,air} Nb_2WO_8 + Nb_8W_9O_{47} \qquad 5\text{-}1$$

A light brown pellet resulted that was crushed with a pestle and mortar and the resulting powder was analyzed using powder XRD.

5.3 Phase analysis

Phase identification was performed using the Bruker EVA version 3 package [2] in a similar way to that described in chapter 3. From the phase identification the resulting powder was found to contain a mixture of two phases of niobium tungstate, namely Nb_2WO_8 and $Nb_8W_9O_{47}$. The resulting plot showing the two identified phases is shown in Figure 5.1

There were no peaks showing the presence of unreacted starting oxide material. In this case the powder mixing method is atom economic and has no byproducts that

need to be removed. The disadvantage to this method is the higher temperatures needed, close to the metal melting points, for the fabrication which can be even higher with high melting point oxides.

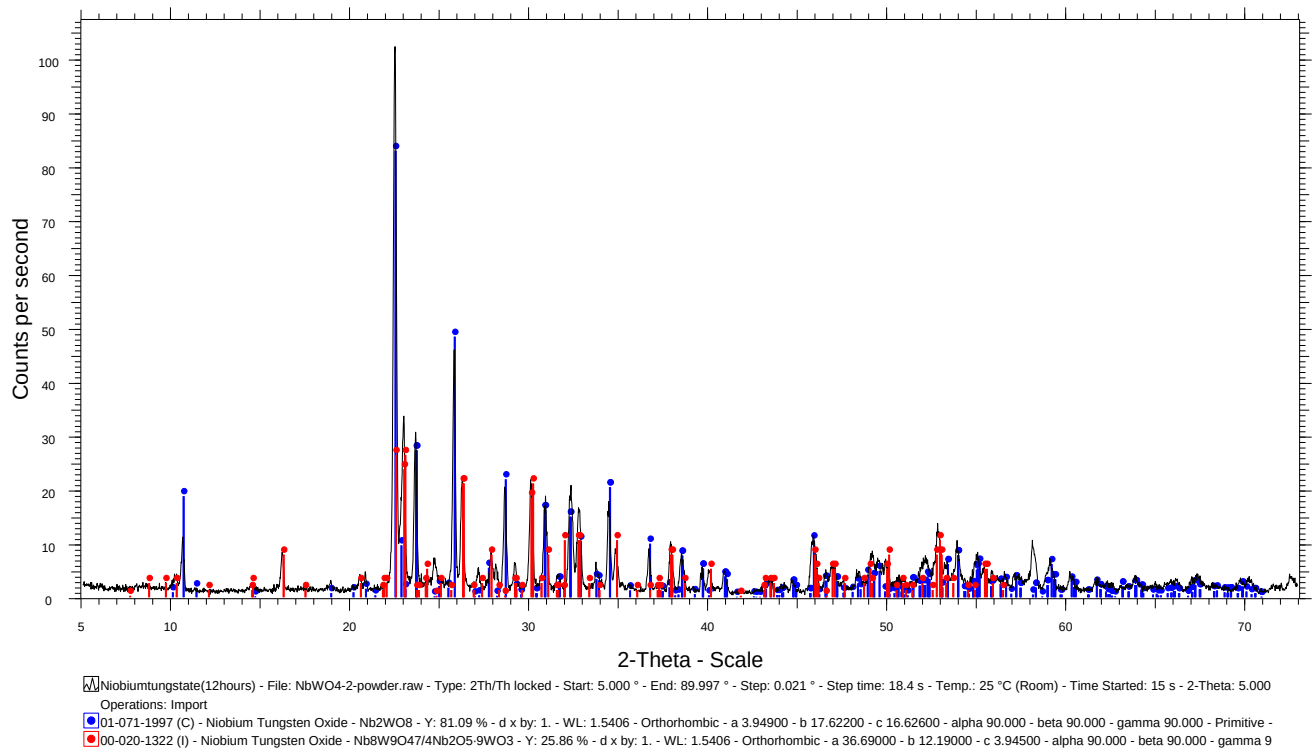


Figure 5.1 Diffractogram showing the measured diffraction pattern with the identified phases of niobium tungstate

5.4 Quantitative Rietveld phase analysis

Relative intensities of different phases in a diffraction pattern give an indication of the relative amount of the crystalline phases present when using the Scherer method. This method of quantification is not robust or always accurate, since only the highest peaks of each phase are considered in the quantification calculation. In the case where the analyzed pattern is not easily resolved this can be difficult. Rietveld refinement gives a better and more accurate way of quantifying different phases from a pattern, because the whole pattern is accounted for during the quantification calculation.

The powder pattern from the mixed phases of niobium tungstate was taken through Rietveld refinement strategies using TOPAS version 3 [108]. The two phases of niobium tungstate identified during the search match exercise were both used as part of the starting model. Refinement was done to model contributions from both phases to match the measured pattern, giving particular attention to the scale factor that defines the intensities.

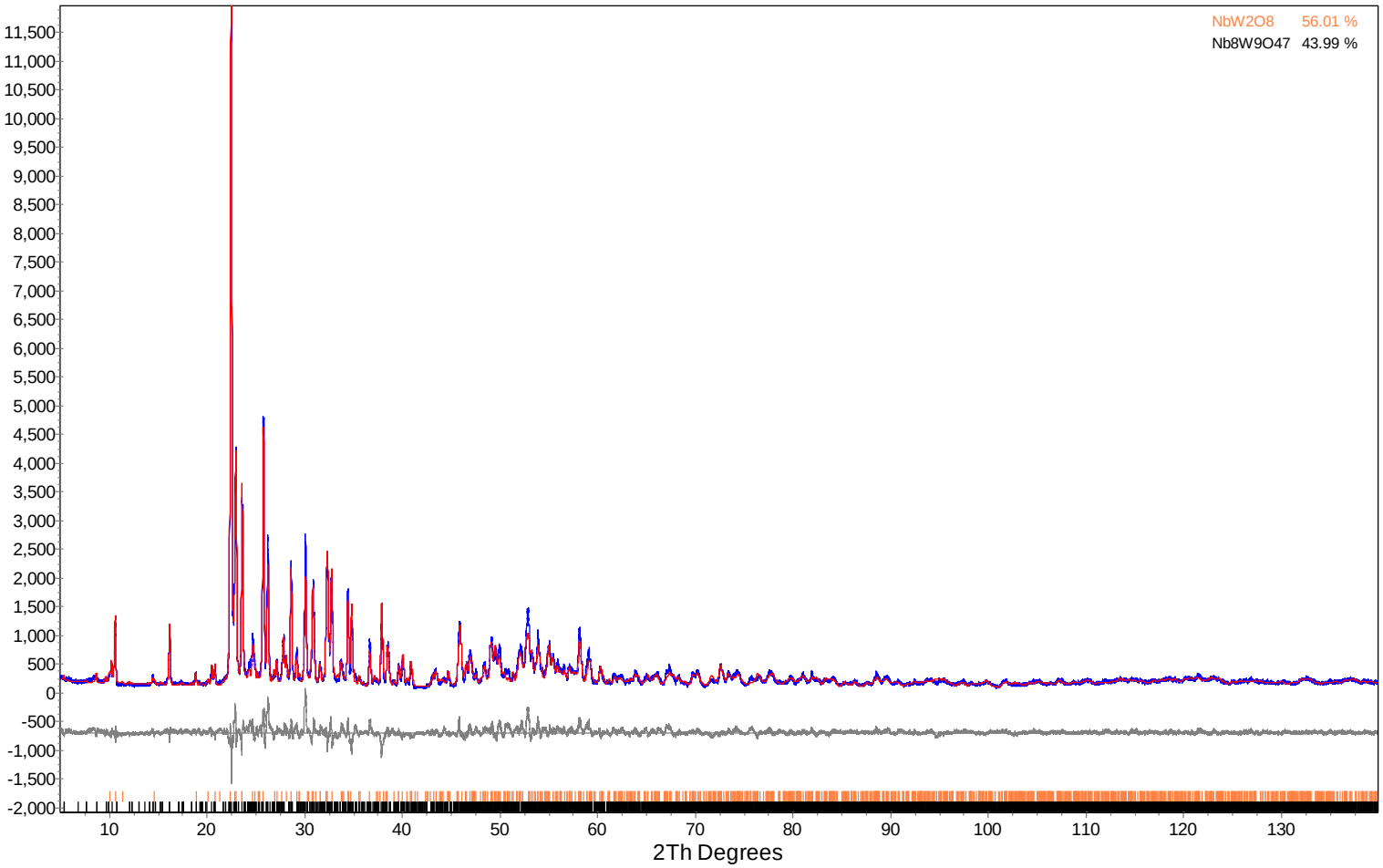


Figure 5.2: TOPAS Difference plot output showing results of the quantitative phase analysis of niobium tungstate, the measured pattern (blue), the calculated pattern (red) and the difference curve (grey) and amounts of each phase

The refinement strategy used was as described in chapter 2, where the aim was to match the calculated pattern to the measured. Figure **5**.**2** shows the refinement results. The graphical representation of the difference curve gives an indication of how close the match, is as represented in Figure **5**.**2**. The goodness of fit χ^2 of this refinement was 2.46, calculated from R_{exp} and R_{wp} of 5.56 and 13.71 respectively.

The resulted best fit, was included with a polynomial of the 2^{nd} order for the background. The co-efficients of the polynomial are listed in Table **5**.**1**. Instrumental factors and corrections for the sample height and Lorentzian polarization factor were used as calibration with for the LaB_6 in chapter 3.

Table 5.1: table showing refined background co-efficient

Chebychev polynomial,	Coefficient
0	-7.0
1	-175.0
2	-38.0

There were no peaks belonging to the same phase that had an intensity mismatch, so no preferred orientation correction was done during the refinement. The refined

unit cell parameters for both phases are listed in appendix D. The peak shape function used was Pearson's VII.

From the quantitative Rietveld refinement analysis done, the niobium tungstate mixture contained 56.01 % Nb2WO8 and 43.99 % $Nb_8W_9O_{47}$. Figure 5.3 shows the graphical representation of the amounts of each phase present in the overall mixture.

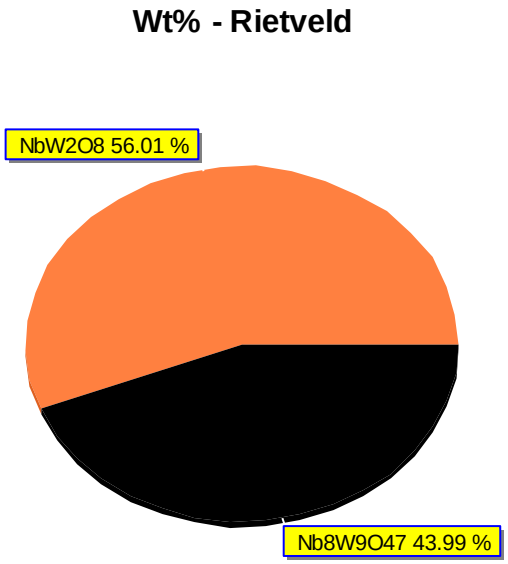


Figure 5.3: Chart showing quantitative results of the different phases in niobium tungstate powder made

5.5 Effect of annealing in air on the niobium tungstate mixture studied by in-situ powder XRD

Most materials have properties or phase composition with temperature. The niobium tungstate mixture was annealed and investigated for any compositional chances with temperature. Variable temperature powder XRD measurements were done using the Anton Par XRK900. The measurements were done as described in chapter 3, from 50^{o}C to 900^{o}C, in 50^{o}C increments. Figure **5**.**4** shows a summary of the powder patterns obtained with temperature.

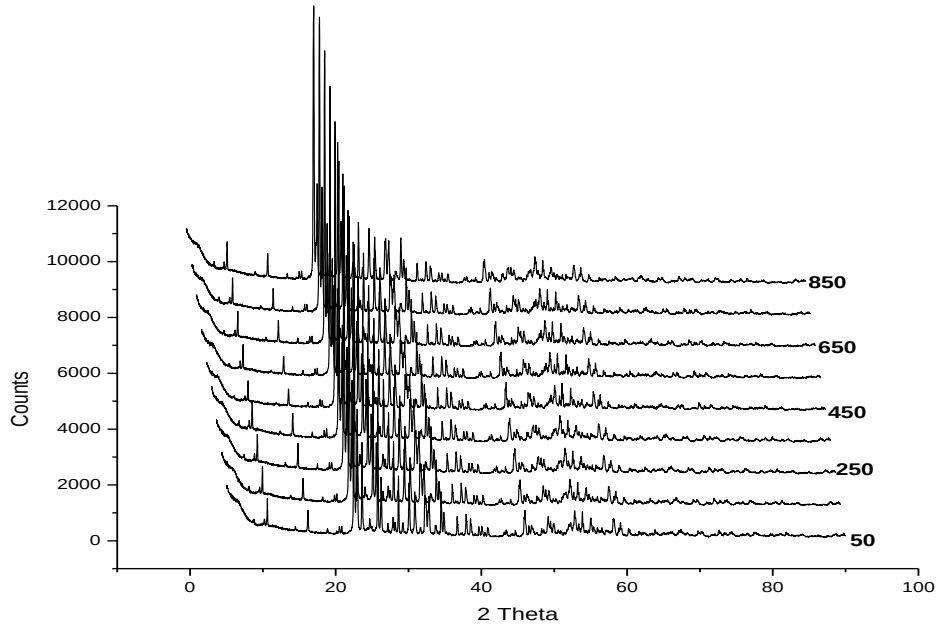


Figure 5.4: XRD patterns of $NiWO_4$ as a function of temperature

The two phases of niobium tungstate made during the classical synthesis method persisted throughout the high temperature analysis. Rietveld refinement was performed on the resulting powder patterns using TOPAS 3. This was done to determine the quantity of each phase in the mixture at each temperature point.

Refinement strategy was used as described in chapter 2 and used throughout this study. Good fit was found between the measured and calculated patterns and the goodness of fit χ^2 for all the different temperatures are listed in Table 5.2.

Table 5.2: Rietveld least squares refinement goodness of fit data for the individual patterns

Temperature	χ^2	Rexp	Rwp	Rp
29	4.89	4.85	23.71	19.22
50	4.86	4.85	23.55	19.12
100	4.78	4.86	23.22	18.91
150	4.71	4.87	22.94	18.7
200	4.66	4.89	22.79	18.6
250	4.64	4.9	22.71	18.61
300	4.62	4.91	22.65	18.48
350	4.61	4.92	22.7	18.59
400	4.65	4.93	22.93	18.76

450	4.68	4.94	23.1	18.95
500	4.85	4.95	24.03	19.77
550	4.92	4.97	24.45	20.24
600	5.07	4.98	25.25	20.84
650	5.22	5.01	26.14	21.62
700	5.42	5.03	27.27	22.49
750	5.63	5.05	28.41	23.38
800	5.72	5.07	29.01	23.7
850	5.84	5.09	29.71	24.19
28	4.83	4.82	23.3	18.93

Error! Reference source not found. shows quantitative phase analysis results of the niobium tungstate mixture at elevated temperatures, as modelled by the Rietveld method. As the temperature increases more of the $Nb_8W_9O_{47}$ phase crystallized (33.69o 35 % of the overall composition). The Nb_2WO_8 phase remained the dominant phase throughout the investigated temperature range.

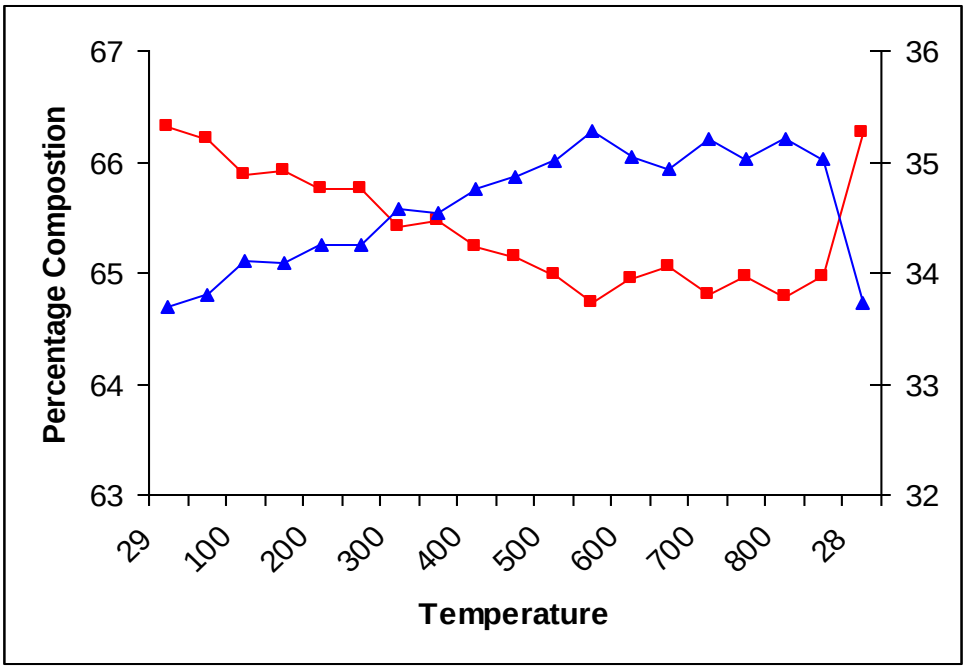


Figure 5.5: Plot showing the compositional changes of the niobium tungstate mixture with temperature, $Nb_8W_9O_{47}$ in red and Nb_2WO_8 in blue.

5.6 ***Conclusion***

This study using niobium tungstate, has demonstrated the use of Rietveld refinement for standardless quantitative phase analysis. The measured powder XRD pattern of niobium tungstate mixture has a lot of peak overlap; therefore highest peak of each phase can not be easily identified. The relative intensity calculation can not be used accurately. The Rietveld method does not require resolved diffraction lines in the diffraction pattern for the different phases since it uses the whole pattern in the calculation. This makes it the more reliable to carry out the phase quantification

5.7 References:

1. R. Pigeon, A. Varma, Quantitative phase analysis of Si_3N_4 by X-ray diffraction, Journal of Mat. Scien. Lett, 1992, **11**(20), 1370

2. N. Scarlet, I Madsen, On-line X-ray diffraction for quantitative phase analysis: application in the Portland cement industry, Powder Diffraction, 2001, **16**(2), 71

3. M. Chmielova, J. Seidlerova, Z. Weiss, X-ray diffraction phase analysis of crystalline copper corrosion products after treatment in different chloride solutions, 2003, **45**(5), 883

4. Chang-An Wang, Aiguo Zhou, Liang Qi, Yong Huang, Quantitative phase analysis in the Ti–Al–C ternary system by X-ray diffraction, Powder Diffraction, 2005, **20**(3), 218

5. A. V. Kurdyumov, V. B. Zelyavskii, N. F. Ostrovskaya, S. N. Gromyko, V. V. Yarosh, N. V. Yarosh, Features of quantitative x-ray diffraction analysis of weakly absorbing powder products with a defective structure, 1998, **37(**11-12), 103

6. B Paplinski, R Kleeberg, J Burgmann, J Wenzel, Quantitative Phase Analysis Using the Rietveld Method - Estimates of Possible Problems Based on Two Interlaboratory Comparisons, Materials science forum, 2004, **45**, 443

7. O Beeri, G Kimmel, Quantitative phase analysis using the Rietveld method for samples in the Ti-Cr binary systems, JCPDS-International Centre for Diffraction Data, 1999, 586

8. Bruker Diffract Plus EVA Search/Match Software, Bruker AXS Ltd., Congleton, UK

9. R.W. Cheary, A.A. Coelho, TOPAS. Version 3. Bruker AXS Inc., Karlsruhe, Germany, J. Appl. Cryst., 1992, **25**, 109

Chapter 6 : Synthesis, characterization and solid state reaction using variable temperature *in-situ* XRD of nickel based oxides

6.1 Introduction

This chapter deals with the synthesis of two nickel based oxides, nickel titanate and nickel tungstate. The former was synthesized using a sol-gel following the work done by Taylor *et. al.* [1]. This group worked on high temperature studies of sol-gel derived nickel and titanium compounds. The work included an investigation into the change in phases of rutile, anatase, brukite and nickel titanate with temperature, and the thermal behaviour of nickel titanate for potential use as a lubricant. Nickel tungstate synthesis was aimed at smaller crystal sizes and was investigated using powder X-ray diffraction and Rietveld refinement at high temperature

Literature reports indicate that oxides of nickel and titanium provided a lubricious surface on silicon nitride without the need of a liquid lubricant [2-3]. Solid lubricants that minimize friction and wear are essential in reducing engine costs by minimizing replacements. There are well developed technologies for making solid lubricants and the best known is molybdenum disulphide (MoS_2). However, MoS_2 is easily affected by oxidation at high temperature, having an oxidation half life of 1 hour at 300^{o}C [4].

This makes the nickel based lubricants better since they are oxides and they will not be affected by oxidation as much as the other.

In the catalysis industry, nickel tungstate based catalysts are used extensively. Nickel-tungstate based catalysts are used in controlling the aromatic content of hydrogen treated fuels [5], hydrodesulphurisation of crude oil [6-7] and propane oxydehydrogenation to propylene [8]. They are advantageous compared to other nickel catalysts because of their high activity in saturation of aromatic reactions. Catalytic activity is related to the surface of the catalyst; the higher the surface are, the more active sites there are and the higher the activity. To attain higher catalytic activity synthesis of this material must be done to target lower crystallite.

6.2 Synthesis

Nickel titanate was synthesized using the sol-gel metal using an alkoxide as described in chapter 2 and following the method of Taylor *et. al*. Commercially available titanium isopropoxide, (Sigma-Aldrich), and nickel acetate tetrahydrate were used as sources of titanium and nickel respectively. A method similar to the method used in chapter 4 for the synthesis of lead tungstate was used for the preparation of nickel titanate. Nickel acetate tetrahydrate was dissolved in alcohol

and added to the titanium isopropoxide solution, in a Ni /Ti 1:1 mole ratio. Water was then added to gel the solution and the gel was then allowed to solidify by evaporating off the ethanol. The solid was then calcined at 600^{o}C in air for 4 hours and Figure **6.1** shows the process. The resulting powder was characterized using powder X-ray Diffraction.

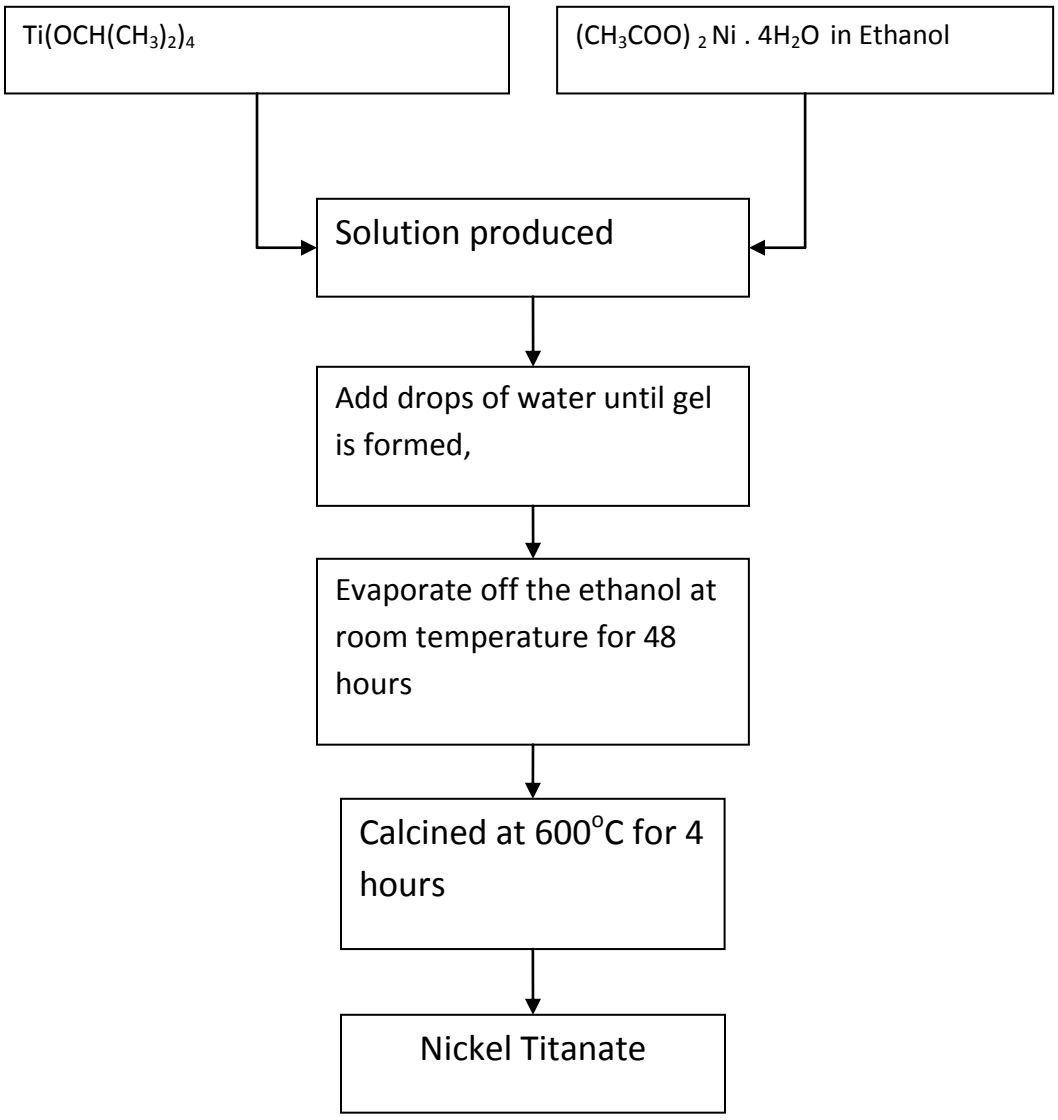


Figure 6.1: Shows a flow diagram of the above described Sol-Gel process

Different ways of preparing nickel titanate have been reported, reaction of $NiCl_2$ and Na_2WO_4 and calcination at 1100^oC for 15 minutes [10], co-precipitation of ammonium tungstate and nickel nitrate and calcination at 550^oC for 4.5 hours [6] or calcination at 902^oC for 2 hours [11] and by refluxing aqueous solutions of stoichiometric amounts of the appropriate metal nitrate salts with ammonium tungstate in the presence of silica and calcination at 290^oC followed by 600^oC for 4hours at each stage [8].

In the present study nickel tungstate was synthesized using the citrate method, which is a variation of the sol-gel method. In the citrate method nickel nitrate and tungsten chloride were first dissolved in citric acid. The resulting solution had sodium hydroxide added it to increase its basic nature, which in turn increases the viscosity of the solution. The viscous mixture was then dried to an amorphous gel. The gel was subsequently calcined at 600^oC in air for 4 hours. Figure **6.2** summarizes the process.

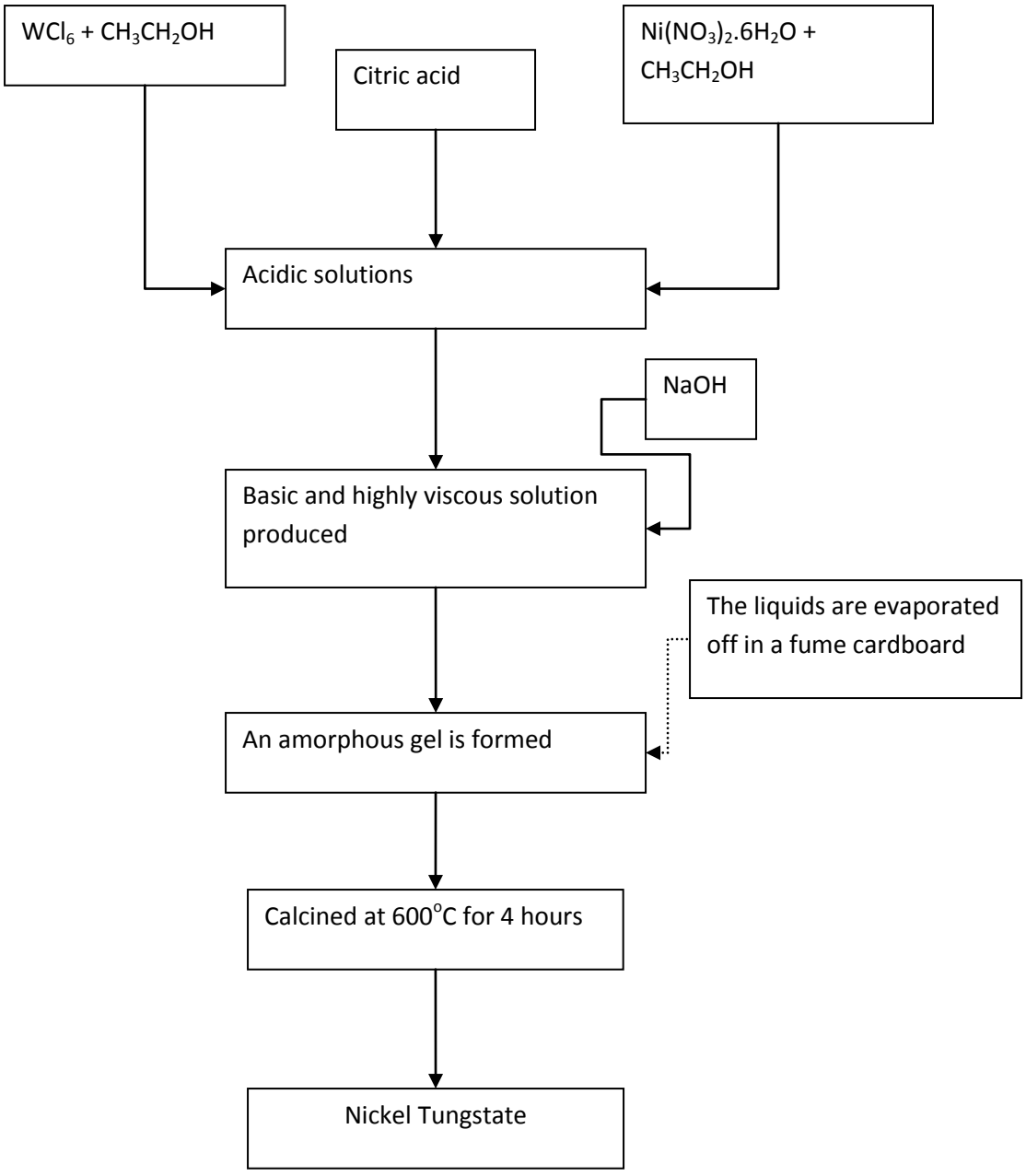


Figure 6.2: Shows a flow diagram of the above described citrate processing method

6.3 Phase identification

Phase identification was performed as described in chapter 4 for lead tungstate. Bruker Eva software version 3 package [2] was used to confirm the phases made from each method. X-ray diffraction finger printing revealed a mixed phase product from the nickel titanate made from sol-gel. Three phases were matched from the powder diffraction file (PDF) database; two nickel titanate phases, $NiTiO_3$ (red) and $Ni_{2.44}Ti_{0.77}O_4$ (purple) corresponding to the peak at 37^o 2θ, which can not be associated with any other phase, and rutile, TiO_2, (blue) signified by reflection at 27^o 2θ as shown in figure.

Table 6.1 lists the unit cell parameters of the identified phases and figure 6.4 shows the search match results. The resulting mixed phase product is consistent with what was shown in the literature.

Table 6.1: shows the phases found during the search match analysis of powder diffraction pattern of the material made using sol-gel method

	Phase	Space group	a (Å)	b (Å)	c (Å)
01-083-0198	$NiTiO_3$	R-3R	5.03110	5.03110	13.79600
00-021-1276	TiO_2 (rutile)	P42/mm	4.59330	4.59330	2.95920
01-081-0353	$Ni_{2.44}Ti_{0.77}O_4$	Fd-3mz	8.33900	8.33900	8.33900

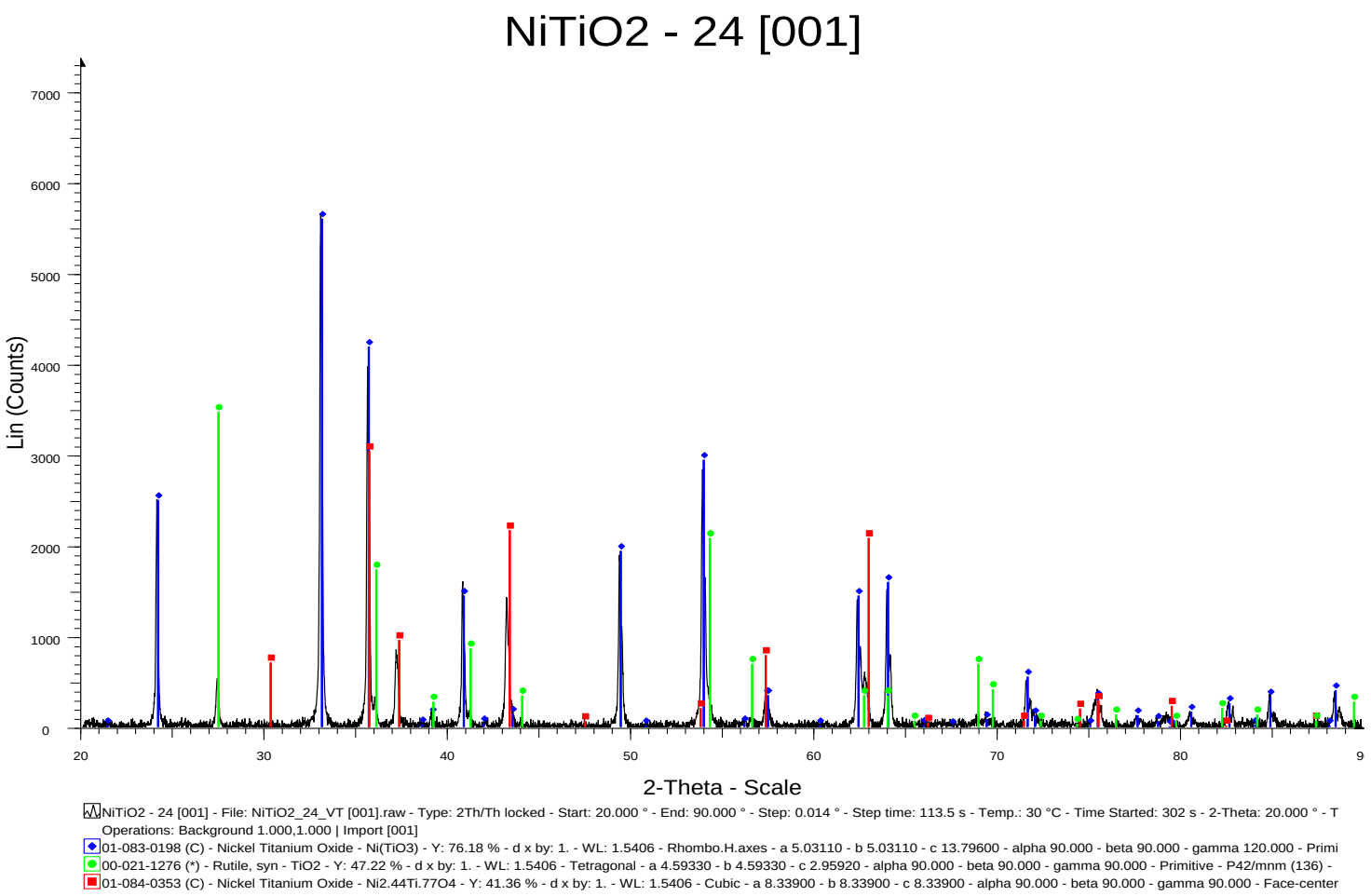


Figure 6.3: Powder diffraction pattern of the material made with the sol-gel method, showing results of the phase the three phases identified by Bruker Eva version 3

For the nickel tungstate synthesis, a single phase of nickel tungstate was identified and matched with the measured powder pattern. The results of the search match are shown in Figure 6.4 and the unit cell parameters in

Table 6.2 .

Table 6.2: shows the phases found during the search match analysis of powder diffraction pattern of the material made using citrate method

	Phase	Space group	a (Å)	b (Å)	c (Å)
01-072-0480	$NiWO_4$	P 2/c (13)	4.59920	5.66060	4.90680

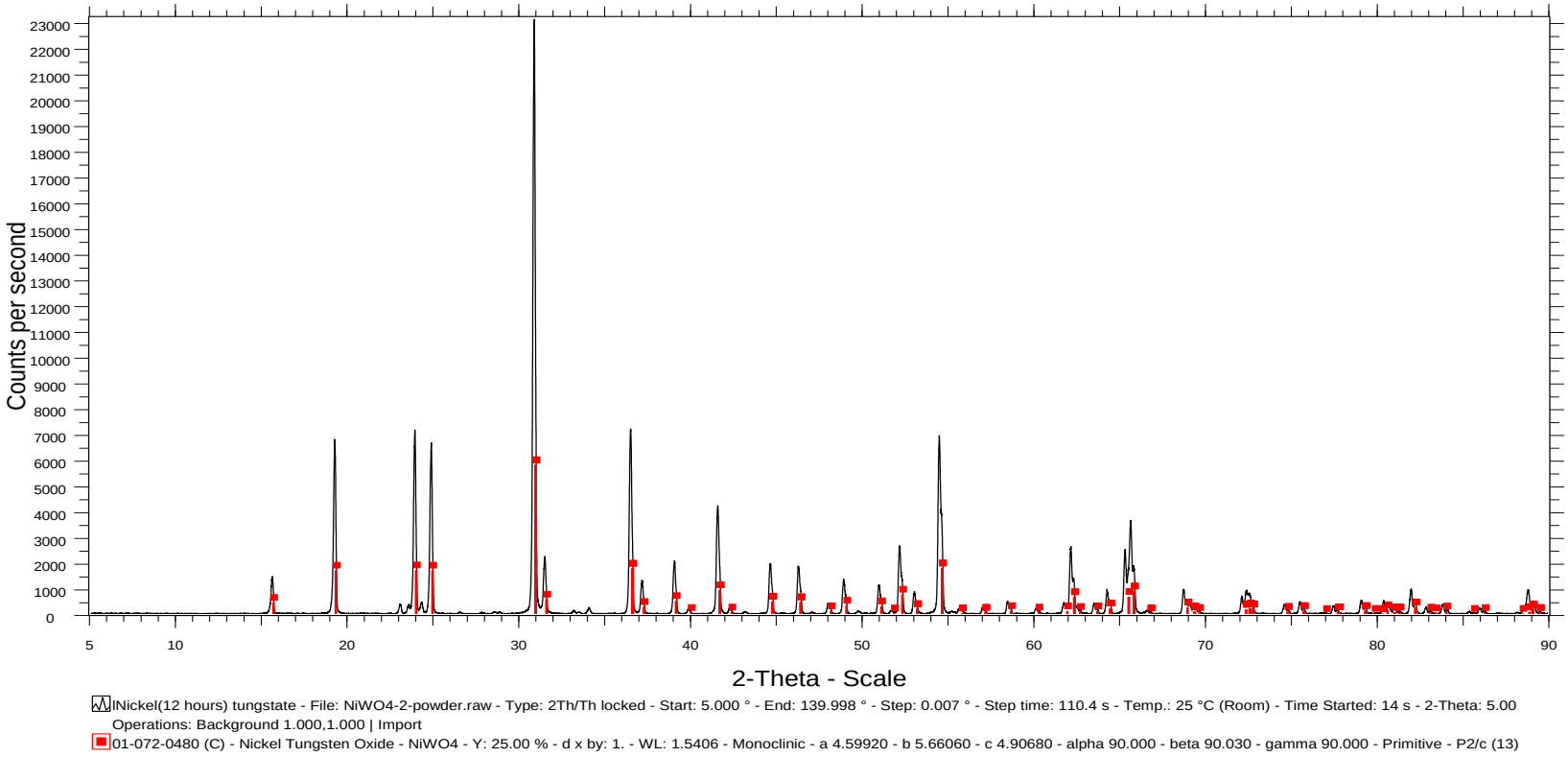


Figure 6.4: Powder diffraction pattern of the material made with the **citate** method, showing results of the phase the three phases identified by Bruker Eva version

6.4 Solid state reaction of nickel titanate using variable temperature in-situ XRD and Rietveld refinement

Variable temperature powder diffraction of the sol-gel produced material was measured at different temperature from 30^{o}C to 900^{o}C at 30^{o}C intervals. Figure **6.5** is a scatter plot showing the different diffraction patterns as a function of temperature. The patterns, as measured increase in temperature and the last one were measured after cooling the material to room temperature.

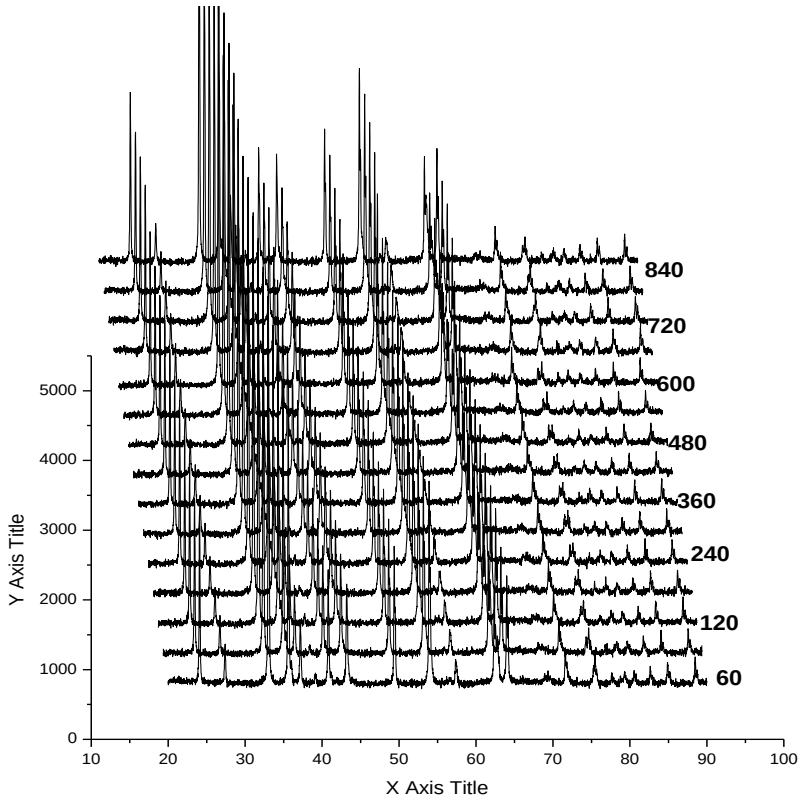


Figure 6.5: XRD patterns of **Nickel titanate** as a function of temperature

The resulting diffraction patterns went through crystal structure refined using TOPAS version 3 Rietveld refinement software according to their phase composition. Instrumental parameters were used according to the calibrations described in chapter 3 for LaB_6 and for the variable temperature attachment using Si.

The global goodness of fit, χ^2 for the refinement was found to be averaging 1.87. Table **6.3** lists the global refinement results.

Table 6.3: List of the global goodness of fit for the refinement

GOF / χ^2	1.87
R_{exp}	3.34
R_{wp}	6.24
R_p	4.16

The background was fitted as a polynomial of the fifth order for all patterns. Only the $Ni_{2.44}Ti_{0.77}O_4$ phase displayed noticeable preferred orientation. Eighth order spherical harmonics were used in the refinement to correct for preferred orientation. The individual goodness of fit for all the refinements is listed in Table **6**.**4**.

Figure **6**.**6Error! Reference source not found.** shows the resultant difference plot following the Rietveld refinement using the diffraction pattern measured at 900^{o}C. The plot illustrates graphically the results of the refinement and represents how all the refinement for other temperatures look like. A multiphase Rietveld refinement includes quantitative phase information as some of the parameters that are optimized This means that by tracking the patterns with temperature, information about what phases are present at what temperature and in what quantities, can be obtained.

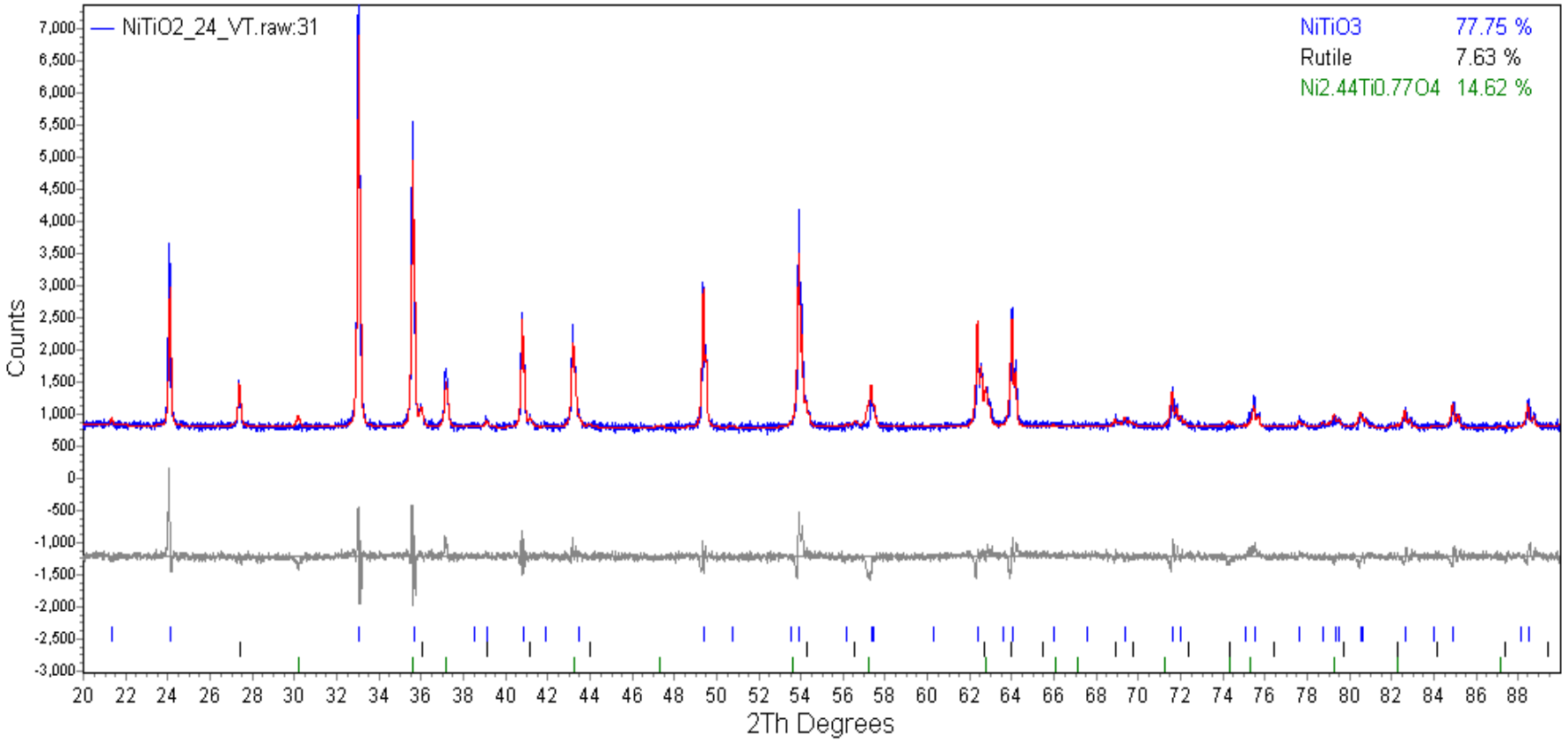


Figure 6.6: TOPAS diffractogram showing results of the Rietveld refinement quantitative phase analysis for Nickel titanate mixture: The measured pattern (black), fitted pattern (red) and difference curve below (blue) and the relative amounts of each phase.

Table 6.4: List Rietveld least squares refinement goodness of fit data for the individual patterns

Temperature	GOF / χ^2	Rexp	Rwp	Rp
29	1.73	3.32	5.75	4.06
60	1.71	3.32	5.68	3.99
90	1.68	3.32	5.56	3.96
120	1.65	3.32	5.49	3.90
150	1.58	3.32	5.25	3.83
180	1.53	3.32	5.07	3.72
210	1.50	3.32	4.98	3.63
240	1.48	3.32	4.90	3.60
270	1.45	3.32	4.83	3.57
300	1.42	3.32	4.7	3.51
330	1.42	3.32	4.72	3.51
360	1.41	3.32	4.67	3.47
390	1.41	3.32	4.69	3.49
420	1.41	3.33	4.68	3.47
450	1.41	3.33	4.70	3.50
480	1.44	3.33	4.80	3.58
510	1.45	3.33	4.82	3.58
540	1.53	3.33	5.10	3.74
570	1.58	3.34	5.27	3.83
600	1.71	3.34	5.70	4.05
630	1.83	3.35	6.12	4.26
660	1.99	3.35	6.66	4.51
690	2.08	3.36	6.99	4.66
720	2.18	3.36	7.32	4.79
750	2.30	3.37	7.74	4.96
780	2.43	3.37	8.19	5.15
810	2.48	3.38	8.37	5.23
840	2.61	3.38	8.82	5.44
870	2.78	3.39	9.44	5.74
900	2.98	3.40	10.14	5.98
28	2.10	3.30	6.93	4.57

Results of the quantitative Rietveld phase analysis study of the prepared nickel titanate mixture are summarized in fFigure 6.7. In present study the gel was calcined at 600^{o}C first before going through the *in situ* XRD measurement and the results showed $NiTiO_3$ as the dominant phase throughout all investigated temperatures, in agreement with the previous work that $NiTiO_3$ forms above 600^{0}C [5]. The amount of $NiTiO_3$ phase present increases with temperature from 77 % to 85 %.

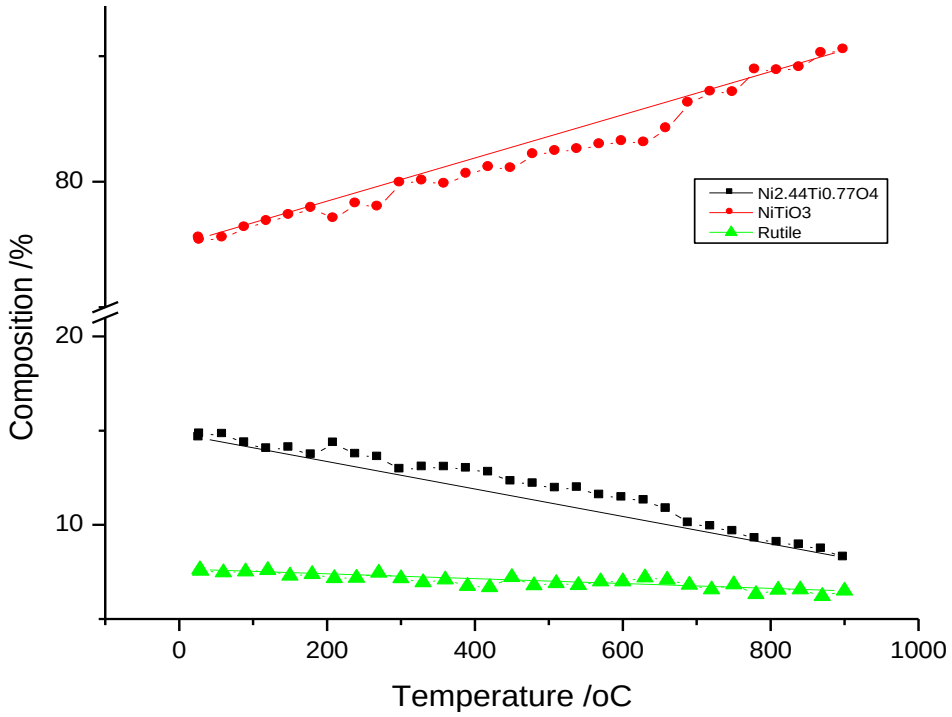


Figure 6.7: Graph showing the results of the composition of each phase from the refinement

The other two phases, rutile and $Ni_{2.44}Ti_{0.77}O_4$, were also detected over all temperature ranges. These results are different to the results obtained from the study done by Taylor *et. al.* [4], for their sol-gel synthesized material; they monitored the species formed as a function of temperature during the calcination step. Table 6.5 summarizes the different phases formed with respect to increasing temperature. Their results showed that only above 600^{o}C does the Nickel titanate phase start forming and became the dominant phase after 800^{o}C and they detected the presence of bunsenite (NiO) at all temperatures. In the present materials, there was no bunsenite was detected at any temperature.

Table 6.5: Composition found of different phases with temperature increase

Temperature(^{o}C)	Phases
400	TiO_2 (anatase)
	NiO
600	$NiTiO_3$
	NiO
	TiO_2 (anatase)
800	$NiTiO_3$
	TiO_2 (rutile)
	NiO
1200	$NiTiO_3$
	TiO_2 (rutile)
	NiO
1400	$NiTiO_3$
	NiO

In our study, the amount of rutile (TiO_2) and $Ni_{2.44}Ti_{0.77}O_4$ decreased linearly with increasing temperature and the amount of $NiTiO_3$ phase. A powder diffraction pattern of the material after cooling to room temperature was also measured. According to the refinement results the compositional ratios of the different phases goes back to the same as before the heat treatment.

6.5 Variable temperature study of nickel tungstate from powder XRD and Rietveld refinement

Powder diffraction patterns at high temperature were measured using the Anton Paar high temperature reaction chamber. The measurements were performed first at room temperature to confirm the starting phases and the rest between 50^{o}C and 900^{o}C at 50^{o}C increment. Figure **6.8** shows a summery of the measured patterns as a function of their temperature.

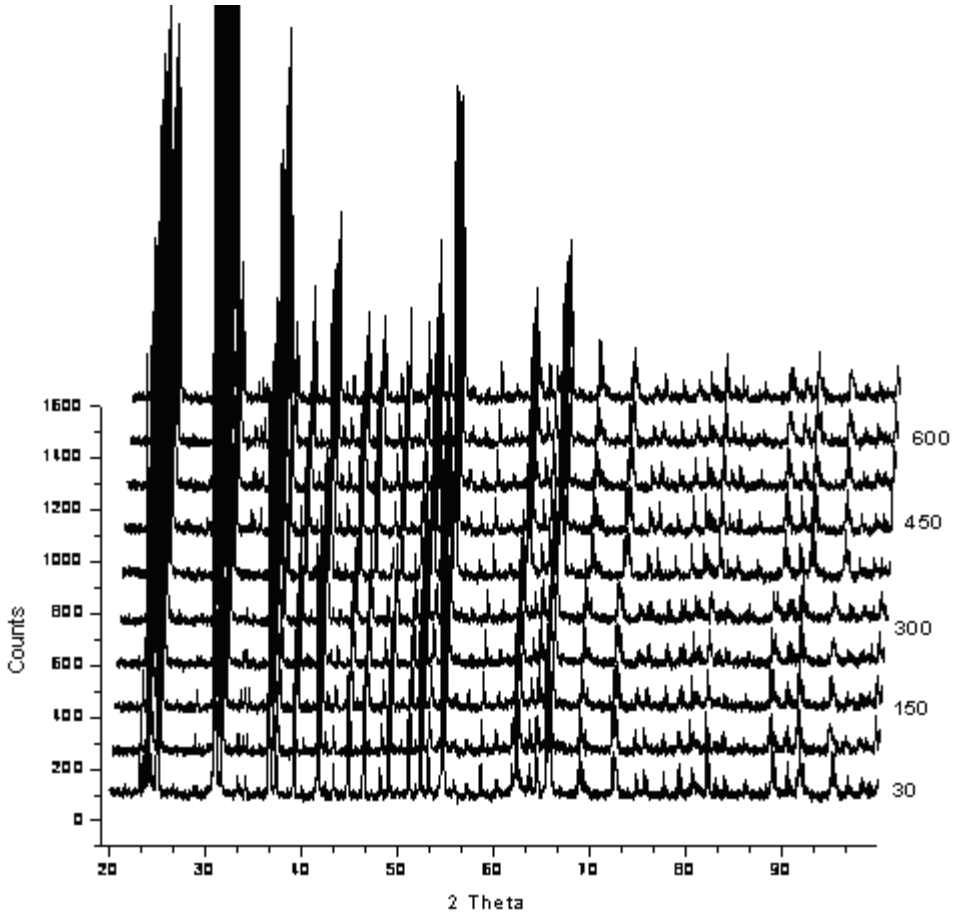


Figure 6.8: XRD patterns of $NiWO_4$ as a function of temperature

Rietveld refinement of the resulting temperature profiled patterns was carried out using TOPAS. The refinement strategy used was as described in chapter 2. A good fit between the measured patterns and the calculated patterns was achieved. The goodness of fit parameters for the individual patterns listed in Table 6.6. Figure 6.9 shows as an example the graphical refinement results of the pattern measured at 450^{o}C. The TOPAS input files are given in appendix.

Table 6.6: shows Rietveld refinement goodness of fit data for the patterns measured at different temperatures

Temperature	X^2	Rexp	Rwp	Rp
30	1.34	8.43	11.33	8.47
49.9	1.33	8.43	11.2	8.34
100	1.34	8.44	11.3	8.46
150	1.34	8.44	11.31	8.46
200	1.36	8.43	11.46	8.49
250	1.34	8.44	11.32	8.51
299.9	1.33	8.46	11.25	8.36
349.9	1.33	8.46	11.29	8.43
399.9	1.33	8.48	11.3	8.34
450	1.38	8.49	11.74	8.69
500	1.42	8.5	12.06	9.01
550	1.32	8.51	11.24	8.38
600	1.42	8.55	12.17	9.02
649.9	1.32	8.56	11.33	8.58
699.9	1.41	8.6	12.12	8.98
749.9	1.26	8.64	10.88	8.42
799.9	1.24	8.69	10.76	8.45
849.9	1.34	8.72	11.65	8.8
899	1.34	8.77	11.77	8.86
26.9	1.16	8.49	9.85	7.7

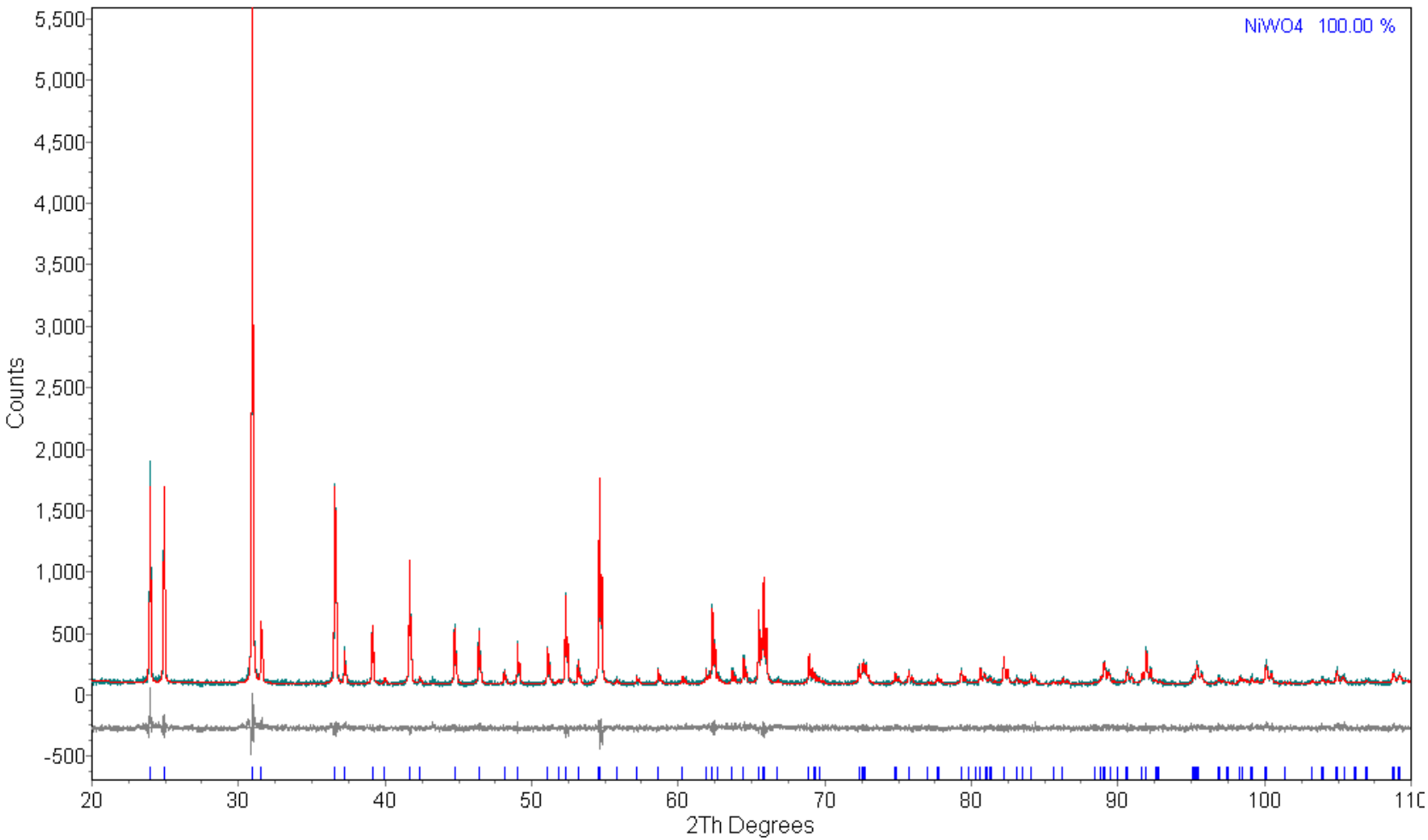


Figure 6.9:TOPAS diffractogram showing results of the Rietveld refinement for Nickel tungstate: The measured pattern (black), fitted pattern (red) and difference curve below (blue) .

X-ray diffraction can be used to derive information about crystallite sizes. The commonly used method for obtaining crystallite sizes from X-ray data is by the Scherrer method [14] which relates to the full width at half maximum calculations of the intensity of the highest peak, based on the formula outline by equation $L = \frac{0.9\lambda}{BCos\theta}$ 6-1.

$$L = \frac{0.9\lambda}{BCos\theta} \qquad \text{6-1 [14]}$$

Where L = crystallite size, B = full width at half maximum and K = 0.9 constant. Rietveld refinement calculates the crystallite size taking into account the whole pattern and not just the highest peak. The disadvantage of using the FWHM of the highest peak is that if there are any preferred orientation effects on the pattern, the highest peak might be due to the orientation effect and false results could be obtained. Figure **6.10** (blue) shows the crystallite sizes plotted against temperatures, which were determined using the Scherrer equation of the peak between 30.4 and 31.8^{o}.

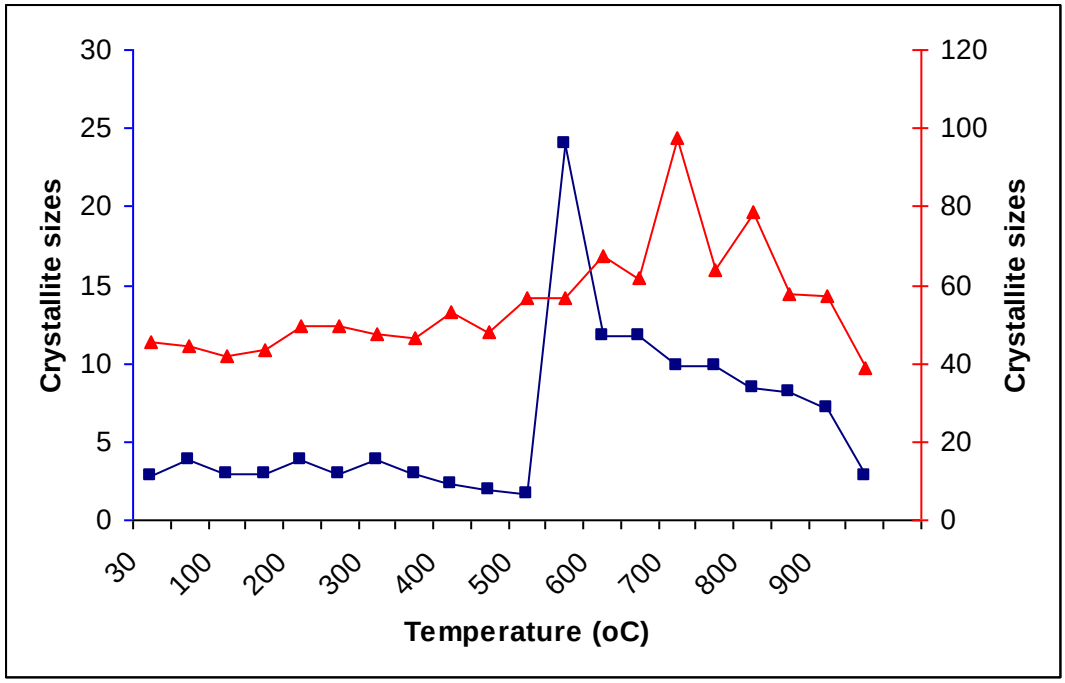


Figure 6.10: Average crystal sizes of NiWO4 as a function of synthesis temperature calculated using the Scherrer equation (Blue) and peak at position 31 2θ and using Rietveld refinement (Red)

From the Rietveld refinements carried out crystallite sizes were extracted. Figure **6.10** (red) summarizes change in crystallite sizes of nickel tungstate with temperature. TOPAS calculates the crystallite sizes by look at the peak line broadening and fitting either Lorentzian or Gaussian peak shape to it. The Crystallite sizes from the Scherrer equation are smaller than that extracted from the refinement.

Unit cell parameters were extracted from the refinement. Table 6.7 summarizes the effect of temperature on the unit cell parameters. There is a general increase in unit cell volume with the temperature increases. The lattice parameters a, b, and c also

increased with higher temperatures. There was no obvious structural phase transition observable in the temperature range under investigation

Table 6.7: Showing unit cell parameters of NiWO4 as a function of temperature

Temperature	a (Å)	b (Å)	c (Å)	beta(°)	Cell Vol (Å^3)
30	4.6016220	5.6677804	4.9131194	89.96378	128.13896
49.9	4.6026497	5.6689352	4.9140155	89.96697	128.21707
100	4.6047970	5.6708020	4.9157337	89.98301	128.36402
150	4.6073530	5.6733706	4.9181039	89.99427	128.55540
200	4.6099962	5.6759850	4.9202890	90.01038	128.74560
250	4.6122404	5.6779554	4.9222927	90.02950	128.90545
299.9	4.6140408	5.6796937	4.9237330	90.04771	129.03297
349.9	4.6171579	5.6827966	4.9265167	90.06587	129.26368
399.9	4.6199087	5.6853977	4.9290341	90.07855	129.46598
450	4.6212152	5.6866610	4.9299767	89.90348	129.55608
500	4.6240873	5.6894951	4.9325181	89.88483	129.76798
550	4.6273203	5.6926236	4.9355070	90.13036	130.00878
600	4.6295723	5.6946266	4.9371501	89.85196	130.16104
649.9	4.6324941	5.6973463	4.9398245	90.16339	130.37588
699.9	4.6358039	5.7007550	4.9426755	89.81655	130.62229
749.9	4.6388224	5.7034055	4.9452283	90.20237	130.83551
799.9	4.6414345	5.7060113	4.9476358	90.22067	131.03260
849.9	4.6457456	5.7105711	4.9517165	89.76307	131.36723
899	4.6492002	5.7138242	4.9547084	89.74141	131.61907
26.9	4.6017158	5.6675695	4.9130280	89.97136	128.13443

Using the unit cell parameters a, b and c, the coefficient of thermal expansion can be calculated in all lattice directions. In the all the lattice directions the coefficient of thermal expansion for NWO_4 is between $0 > \sigma_m < 2 \times 10^{-6} K^{-1}$, which make this material to fall in the lower thermal expansion materials group. Table 6.8 summarizes the thermal expansion co-efficient for NWO_4.

Table 6.8: Showing the coefficient of thermal expansion of NiWO4 as a function of temperature

	Coefficient of thermal expansion		
Temperature	**a (Å)**	**b (Å)**	**c (Å)**
30	1.1E-05	1.0E-05	9.2E-06
49.9	9.3E-06	6.6E-06	7.0E-06
100	1.1E-05	9.1E-06	9.6E-06
150	1.1E-05	9.2E-06	8.9E-06
200	9.7E-06	6.9E-06	8.1E-06
250	7.8E-06	6.1E-06	5.9E-06
299.9	1.4E-05	1.1E-05	1.1E-05
349.9	1.2E-05	9.2E-06	1.0E-05
399.9	5.6E-06	4.4E-06	3.8E-06
450	1.2E-05	1.0E-05	1.0E-05
500	1.4E-05	1.1E-05	1.2E-05
550	9.7E-06	7.0E-06	6.7E-06
600	1.3E-05	9.6E-06	1.1E-05
649.9	1.4E-05	1.2E-05	1.2E-05
699.9	1.3E-05	9.3E-06	1.0E-05

749.9	1.1E-05	9.1E-06	9.7E-06
799.9	1.9E-05	1.6E-05	1.6E-05
849.9	1.5E-05	1.2E-05	1.2E-05
899	1.2E-05	9.3E-06	9.6E-06
Average	**1.2E-05**	**9.3E-06**	**9.7E-06**

6.6 Conclusion

In this chapter the use of Rietveld refinement and variable temperature powder XRD studies to track the extent of a reaction and to determine the co-efficient of thermal expansion of a material was demonstrated. This was done by synthesizing a nickel titanate mixture and subjecting it through a temperature range (30 – 900^{o}C) and using quantitative Rietveld refinement to determine the amounts of each component in the mixture through the range. The co-efficient of thermal expansion of nickel tungstate synthesized by sol-gel was determined over the same temperature range

6.7 References:

1. D.J Taylor, P.F. Fleigh, R.A Page, Characterization of nickel titanate synthesized by sol-gel processing, Thin solid Films, 2002, **408**, 104

2. C.R. Blanchard-Ardid, J. Lankford, R.A. Page, L.E. Pope, L. Fehrenbacher, W.O. Winer (Eds.), *New Materials Approaches to Tribology: Theory and Applications*, Boston, USA, 1988, Materials Research Society Symposium Proceeding, 1989, **140**, 345

3. R.A.Page, C.R. Blanchard-Ardid, W. Wei, Effect of particulate additions on the contact damage resistance of hot-pressed Si_3N_4, J. Mater. Sci., 1988, **23**, 946

4. H.E. Sliney, *Friction, Lubrication, and Wear Technology, ASM Handbook,* ASM International, Metals Park, OH, 1992, **18,** 115

5. Y. Yoshimura, T. Sato, H. Shimada, N. Matsubayashi, M Imamura, A Nishijima, M. Higo b, S. Yoshitomi, Preparation of nickel-tungstate catalysts by a novel impregnation method, Catalysis Today, 1996, **29,** 221

6. F.J. Gil-Llamb´ıas, H. Rodriguez, I. Bouyssiers, M. Escudey, I. Carkovic, J. Catal., 1986, **102,** 37

7. B. Scheffer, P. Molhoek, J.A. Moulijn, Temperature-programmed reduction of NiO–WO3/Al2O3 hydrodesulphurization catalysts, Appl. Catal., 1989, **46**, 11.

8. D.L. Stern, R.K. Grasselli, J. Catal., 1997, **167**, 570

9. Bruker Diffract Plus EVA Search/Match Software, Bruker AXS Ltd., Congleton, UK

10. Joint Committee on Powder Diffraction Standards_JCPDS.–International Centre for Diffraction Data, ICDD, 15-0755,1996

11. B. Scheffer, J.J. Heijeinga, J.A. Moulijn, Framework topology of tectosilicates and its characterization in terms of coordination degree sequence, J. Phys. Chem., 1987, **91**, 4752

12. J.M. Quintana-Melgoza a, J. Cruz-Reyes b, M. Avalos-Borja, Synthesis and characterization of NiWO crystals Materials Letters, 2001, **47,** 314

13. A Guinier, X-ray diffraction: in crystals, imperfect crystals, and amorphous bodies, **ch 5**, 124

14. V.A. Drits, J. Srodon, D.D. Eberl, XRD measurement of mean crystallite thickness of illite and illite/smectite; reappraisal of the Klubler index and the Scherrer equation, Clays and clay Minerals, 1997, **45**(3), 461

Chapter 7 General conclusion

The synthesis of different mixed metal oxides using traditional and modern fabrication methods such as sol-gel, citrate and classical solid state synthetic techniques were shown by the present study. Sol-gel was used in the synthesis of Lead tungstate and nickel titanate, the citrate method used for the synthesis of the nickel tungstate and a mixed niobium tungstate material was synthesized using the classical solid state synthetic techniques.

The powder diffraction technique was used as a method for characterizing and understanding the structure of all the compounds synthesized. Combining Rietveld refinements' and *in-situ* powder X-ray diffraction with variable temperature range, several properties of the materials including thermal properties and behavior were studied and determined.

The coefficient of thermal expansion of Lead tungstate was determined at a temperature ranging from 30 - 90^{o}C. This material showed a positive thermal expansion with coefficient of 0 - 2 x 10-5 K^{-1}. The quantitative phase analysis of niobium tungstate mixture was shown at different temperatures using the Rietveld refinement for standardless quantitative phase analysis based on the whole pattern in the calculation instead of relative intensity calculation used traditionally.

Rietveld refinement and variable temperature powder XRD studies was also used to track the extend of a reaction of nickel titanate mixture and to determine the co-efficient of thermal expansion of nickel tungstate over a temperature range of 30 – 900^{o}C.

Chapter 8 List of Figures

Figure 2-1: Schematic diagram of the general sol-gel processes 18
Figure 2-2: Process flow diagram for synthesis of $Ba_3CoCuFe_{24}O_{47}$ using the citrate gel method. 20
Figure 2-3 Potential energy diagram of a harmonic oscillator **Error! Bookmark not defined.**
Figure 2-4 Potential energy diagram for an anharmonic oscillator 26
Figure 2-5 Change in length, L, of a sample of material as a function of temperature, T [33] 29
Figure 2-6 : Diagram of water molecules and the density plot as it freezes. Water contracts as it gets colder until it reaches 3.97 °C, then forms an open crystal structure that causes it [39] 32
Figure 2-7: Diagram showing the framework of ZrW_2O_8 perovskite during negative thermal expansion [59] 33
Figure 2-8: Diagram showing the straight and vibrational mode of the M-O-M bond, the arrows showing the vibrational movement of the oxygen 35
Figure 2-9: Schematic of a push rod mechanical dilatometer for thermal expansion measurement of specimen, (S) 36
Figure 2-10: Diffraction from a polycrystalline material, where the one dimensional powder patterns can be obtained by scanning a detector across the cones of diffracted intensity [86] ..... **Error! Bookmark not defined.**
Figure 2-11 : Powder diffraction data recorded on heating the non-activated mixture of $CaCO_3$ and TiO_2. Data at increasing temperatures have been offset vertically. 43
Figure 2-12: Showing change in scattering angle, θ, which was used in calculating the thermal expansion behavior of sulfur [93] 45
Figure 2-13: Comparison between Gaussian (dashed) and Lorentzian (solid) distributions. The functions of the two distributions are given in Eqns. 2.7 and 2.8, respectively [98]. 49
Figure 2-14: plot showing the curve fitting and deviation used in Pearson VII function 51
Figure 3-1 A Bruker D8 advance automated X-ray diffractometer which was used for all X-ray measurements 69
Figure 3-2: TOPAS Rietveld refinement results for LaB_6: fitted pattern (red), experimental pattern (blue) and the difference curve (grey) 72
Figure 3-3: Picture and schematic diagram of the Anton Paar XRK900 high temperature reaction chamber [6] 73
Figure 3-4: XRD powder pattern of the measured from the search match, phase identification Bruker Eva program showing all peaks of the measured powder corresponding to silicon 77
Figure 3-5: XRD patterns of silicon standard as a function of temperature 78
Figure 3-6: TOPAS output showing the results of the refinement of silicon standard, the measured pattern (blue), the calculated pattern (red) and the difference curve (grey) 80
Figure 4-1: Schematic diagram of a lead tungstate scintillators [15] 89

Figure 4-2: Plot showing coefficient of thermal expansion and light yield of lead tungstate with temperature [19].....90
Figure 4-3: Shows a flow diagram of the Sol-Gel process described above.....**Error! Bookmark not defined.**
Figure 4-4 XRD powder pattern of the measured from the search match, phase identification Bruker; Eva program showing all peaks of the measured powder corresponding to lead Tungstate, stolzite. 95
Figure 4-5*:* Rietveld refinement results for PbWO4: The measured pattern (black), fitted pattern (red) and difference curve below (blue) 99
Figure 4-6: Diamond diagram showing packing pattern extracted from the refinement of the synthesized lead tungstate.....107
Figure 4-7: Diagram showing the tetrahedral bonding of tungsten with oxygen.....108
Figure 4-8: Diagram showing the tetrahedral bonding of Lead with oxygen.....109
Figure 4-9: Selected XRD patterns of $PbWO_4$ as a function of temperature 110
Figure 4-10: Plot shows the increase in the unit cell parameter c with temperature for the refined variable temperature measurement of lead tungstate 113
Figure 4-11 Plot shows the increase in the unit cell parameter a with temperature for the refined variable temperature measurement of lead tungstate 114
Figure 4-12: Plot of co-efficient of linear thermal expansion over a temperature range of $PbWO_4$ calculated from refined unit cell parameters 115
Figure 5-1 Diffractogram showing the measured diffraction pattern with the identified phases of niobium tungstate.....122
Figure 5-2: TOPAS Difference plot output showing results of the quantitative phase analysis of niobium tungstate, the measured pattern (blue), the calculated pattern (red) and the difference curve (grey) and amounts of each phase.....124
Figure 5-3: Chart showing quantitative results of the different phases in niobium tungstate powder made.....126
Figure 5-4: XRD patterns of $NiWO_4$ as a function of temperature 128
Figure 5-5 Plot showing the compositional changes of the niobium tungstate mixture with temperature, $Nb_8W_9O_{47}$ in red and Nb_2WO_8 in blue 131
Figure 6-1: Shows a flow diagram of the above described Sol-Gel process.....136
Figure 6-2: Shows a flow diagram of the above described citrate processing method138
Figure 6-3: Powder diffraction pattern of the material made with the sol-gel method, showing results of the phase the three phases identified by Bruker Eva version 3...140
Figure 6-4: Powder diffraction pattern of the material made with the citate method, showing results of the phase the three phases identified by Bruker Eva version.....142
Figure 6-5: XRD patterns of $NiWO_4$ as a function of temperature 143
Figure 6-6: TOPAS diffractogram showing results of the Rietveld refinement quantitative phase analysis for Nickel titanate mixture: The measured pattern (black), fitted pattern (red) and difference curve below (blue) and the relative amounts of each phase. 146
Figure 6-7: Graph showing the results of the composition of each phase from the refinement 148
Figure 6-8: XRD patterns of $NiWO_4$ as a function of temperature 151
Figure 6-9:TOPAS diffractogram showing results of the Rietveld refinement for Nickel tungstate: The measured pattern (black), fitted pattern (red) and difference curve below (blue) 153

Figure 6-10: Average crystal sizes of NiWO4 as a function of synthesis temperature calculated using the Scherrer equation (Blue) and peak at position 31 2θ and using Rietveld refinement (Red) 155

Chapter 9 List of Tables

Table 2.1: list of parameters and corrections refined during Rietveld refimenet 47
Table 2.2: Listing some of the available Rietveld software 59
Table 3.1: Refined parameters for LaB_6 70
Table 3.2: XRK 900 Chamber Specifications 74
Table 3.3: List Rietveld list squares refinement global goodness of fit data..... 81
Table 3.4: List Rietveld list squares refinement goodness of fit data for the individual patterns..... 82
Table 3.5: Showing a comparison of the unit cell parameters of the current calibration and literature values..... 83
Table 4.1 shows search match results of experimental powder diffraction pattern..... 96
Table 4.2 *Cell parameters of our Stolzite type structure [ref]* 96
Table 4.3: *Refinement statistics* 98
Table 4.4 Refined linear background coefficients..... 100
Table 4.5: Refined structural parameters..... 101
Table 4.6: listing the refined coefficient of the shape factor from a Pearson VII function 103
Table 4.7: Refinement statistics..... 104
Table 4.8: Showing preferred orientation refinement results using 8^{th} order spherical harmonics..... 105
Table 4.9: List refined atomic coordinates 106
Table 4.10: List Rietveld list squares refinement goodness of fit data..... 111
Table 5.1: table showing refined background co-efficient 125
Table 5.2: List Rietveld least squares refinement goodness of fit data for the individual patterns..... 129
Table 6.1: shows the phases found during the search match analysis of powder diffraction pattern of the material made using sol-gel method..... 139
Table 6.2: shows the phases found during the search match analysis of powder diffraction pattern of the material made using citrate method..... 141
Table 6.3: List of the global goodness of fit for the refinement..... 144
Table 6.4: List Rietveld least squares refinement goodness of fit data for the individual patterns..... 147
Table 6.5: Composition found of different phases with temperature increase 149
Table 6.6: shows Rietveld refinement goodness of fit data for the patterns measured at different temperatures..... 152
Table 6.7: Showing unit cell parameters of $NiWO_4$ as a function of temperature 156